

Precision mass measurements of
neutron-deficient nuclei in $A \sim 60 - 80$ region via
multireflection time-of-flight mass spectrograph

Sota Kimura

November 2017

Precision mass measurements of
neutron-deficient nuclei in $A \sim 60 - 80$ region via
multireflection time-of-flight mass spectrograph

Sota Kimura

Doctoral Program in Physics

Submitted to the Graduate School of
Pure and Applied Sciences
in Partial Fulfillment of the Requirements
for the Degree of Doctor of Philosophy in
Science
at the University of Tsukuba

Abstract

Nuclear masses of proton-rich nuclei along the $N = Z$ line are crucial in determining the reaction flow of explosive nucleosynthesis in what is called the rapid proton-capture (rp -) process. The rp -process follows a pathway which transits through several key $N = Z$ nuclei, notably ^{64}Ge , ^{68}Se and, ^{72}Kr , the exact route being strongly dependent on the effective lifetimes of these waiting-point nuclei. Effective lifetimes of waiting-point nuclei depend exponentially on the Q -values of both the one- and two-proton capture reactions. The uncertainties in the masses of $N = Z - 1$ and $N = Z - 2$ nuclei, which are counterparts in the determination of Q -values, need to be less than roughly 10 keV to significantly reduce the uncertainties of rp -process calculations.

High-precision experimental mass data of nuclides near the $N = Z$ line are also necessary for verification of the Standard Model through the unitarity of the Cabibbo-Kobayashi-Masukawa (CKM) matrix. The necessary nuclear parameters for it are partial lifetimes of the $0^+ \rightarrow 0^+$ transition and the corresponding Q_{EC} -values. Sufficiently precise Q_{EC} -values require nuclear masses be known to a relative precision of $\delta m/m \lesssim 5 \times 10^{-8}$.

Precision mass measurement experiments of these intermediate-mass proton-rich nuclei with The SHE-mass facility, which consists of a multireflection time-of-flight mass spectrograph (MRTOF-MS) coupled with the gas-filled recoil ion separator GARIS-II via a cryogenic gas-cell and an ion transport system, were proposed. Half-lives of these nuclei span from $\sim 10 - 100$ msec, and the MRTOF-MS has an advantage for mass measurements of these short-lived nuclei due to the short measurement time of less than 10 msec.

These intermediate-mass proton-rich nuclei can be produced using symmetric fusion-evaporation reactions. In performing mass measurements at the SHE-mass facility with symmetric reactions, a difficulty arises from the lack of separation between the primary beams and the reaction products in GARIS-II due to the small difference of their $B\rho$ -values. Thus, the use of these symmetric reactions with intense primary beams could result in damage to the experimental equipment by irradiation with intense contaminants. To overcome this, improved beam stoppers have been developed to enhance the suppression of such particles. A performance evaluation was carried out by using the $^{208}\text{Pb}(^{18}\text{O}, 3n)^{223}\text{Th}$ reaction. Consequently, we have achieved a 200-fold enhancement of the signal-to-noise ratio at the GARIS-II focal plane.

The masses of ^{63}Cu , $^{64-66}\text{Zn}$, $^{65-67}\text{Ga}$, $^{65-67}\text{Ge}$, ^{67}As , $^{78,81}\text{Br}$, $^{79\text{m}}\text{Kr}$, $^{80,81\text{m}}\text{Rb}$, and $^{79,80}\text{Sr}$ were measured by using the SHE-mass facility with the beam stoppers. The masses of these nuclides have been determined by the single reference method using isobaric references of well-known mass. There are some inconsistencies with the 2016 Atomic Mass Evaluation values, and two corrected mass excess values are proposed: $\text{ME}(^{67}\text{Ge}) = -62675.2(46)$ keV and $\text{ME}(^{81}\text{Br}) = -77955.4(53)$ keV. This result reinforces the need for direct mass measurements of all nuclides, even for stable isotopes, if their masses were previously evaluated by indirect techniques. The relative mass precisions in the present study span the range of $\delta m/m \sim 10^{-7}$ to 10^{-8} . In the most precise measurement, that of ^{65}Ga , a mass uncertainty of 2.1 keV was obtained. This result shows that mass measurements satisfying the requirement of the CKM matrix can be achieved with the MRTOF-MS, given sufficient statistics.

We demonstrate that the SHE-mass facility is suitable for precision mass measurements of not only SHE but also intermediate-mass proton-rich nuclei, which are crucial to the rp -process.

Contents

1	INTRODUCTION	5
1.1	The rp-process pathway	5
1.2	Other physics subjects related to region of focus	8
1.2.1	Unitarity of CKM matrix	9
1.2.2	Coulomb displacement energy	11
1.3	Nuclear mass determination techniques	12
1.3.1	Q -value determinations	12
1.3.2	Direct measurements at intermediate- and high-energies	15
1.3.3	Direct measurements at low-energy	17
1.3.4	Multireflection time-of-flight mass spectrograph	19
1.4	Experimental apparatuses	27
1.4.1	SHE-mass facility	28
1.4.2	Gas-filled recoil separator GARIS-II	29
1.4.3	Cryogenic gas-cell and Ion transport system	30
2	EXPERIMENTS	36
2.1	Reaction systems	36
2.2	Primary beam separation	38
2.2.1	Difficulty in primary beam separation	38
2.2.2	Design of the primary beam stoppers	38
2.2.3	Performance evaluation of the primary beam stoppers	41
2.3	Modification of the SHE-mass facility	41
2.4	Target preparations	46
2.5	Online measurement	46
2.5.1	Mean charge state of intermediate-mass ions	46
2.5.2	Space charge effects on the gas-cell extractions	49
3	ANALYSIS	51
3.1	Analysis method	51
3.2	Fitting function	53
3.3	Error evaluation	55
4	RESULTS	58
4.1	$A/q = 65$	58
4.2	$A/q = 66$	59
4.3	$A/q = 67$	59
4.4	$A/q = 79$	59
4.5	$A/q = 80$	59

4.6	$A/q = 81$	60
5	DISCUSSION	79
5.1	Mass evaluation of ^{67}Ge and ^{81}Br	79
5.2	Measurement precision and its limitation	83
5.2.1	Position of the present study in the mass measurements	83
5.2.2	Systematic error originating from δt_{drift}	84
5.2.3	Systematic error originating from binning	85
5.3	Overall efficiency in the present measurement	86
5.4	Further applications of the SHE-mass facility	88
5.4.1	Vicinity of ^{100}Sn	88
5.4.2	Neutron-rich superheavy nuclei	89
6	SUMMARY AND CONCLUSIONS	91

List of Figures

1.1	The rp -process path in the type I X-ray bursts for the $A \sim 60 - 80$ region .	6
1.2	Effective lifetime of the waiting-point nucleus ^{64}Ge	7
1.3	Nuclear mass dependence of the light curve in X-ray bursts	8
1.4	Histogram of the fractional uncertainties of the final $\mathcal{F}t$ -values	10
1.5	The CDE values among the even-even $N = Z - 2$ nuclei.	11
1.6	Schematic view of Penning trap and ion circular motion in it.	18
1.7	Schematic of TOF-ICR detection technique.	18
1.8	Schematic and conceptual views of MRTOF-MS	20
1.9	Scan over lap number to determine number of laps	21
1.10	Schematic view of ion capturing and ejection in MRTOF	22
1.11	Schematic view of the MRTOF-MS at ISOLDE/CERN.	23
1.12	Schematic view of the MRTOF-MS at FAIR/GSI.	24
1.13	Spatial separation of $^{211g,221m}\text{Po}$ by use of the BNG in the MRTOF-MS. . .	25
1.14	Schematic view of the MRTOF-MS at RIKEN.	26
1.15	Measured effect of thermal expansion on the TOF	27
1.16	Schematic view of the SHE-mass facility.	28
1.17	Gas pressure dependence of the $B\rho$ -resolution.	30
1.18	Strutt diagram.	31
1.19	Conceptual view of ion surfing method on the RF carpet.	33
1.20	Photograph of the flat trap with typical direct current voltages annotated.	34
1.21	Conceptual view of time-of-flight drift compensation.	34
1.22	Conceptual view of drift tube.	35
1.23	Schematic of the working principle of a Bradbury-Nielsen gate.	35
2.1	Comparison of theoretical and experimental production cross-sections. . . .	37
2.2	Predicted $B\rho$ -values of primary beam.	39
2.3	Ion trajectories in GARIS-II.	39
2.4	Simulated position distribution at GARIS-II D1 entrance.	40
2.5	Schematic view of the primary beam stoppers.	40
2.6	Result of the Stopper1 performance evaluations.	42
2.7	Result of the Stopper2 performance evaluations.	42
2.8	Summed energy spectra of the silicon detector array.	43
2.9	Schematic view of the GARIS-II focal plane setup.	44
2.10	Schematic view of the β -activity counter	45
2.11	Schematic view of the ion transport system	45
2.12	Schematic view of the target irradiation test setup.	47
2.13	Peak energy shift of the α -particles.	47
2.14	Intensity distribution of β -activities as a function of magnetic rigidity. . . .	48
2.15	Lifetime measurement at the β -activity counter.	49

2.16	Primary beam intensity dependence of gas-cell extraction efficiencies. . . .	50
3.1	Process of time-of-flight drift compensation.	52
3.2	Flow chart of the analysis program.	54
3.3	Typical time-of-flight spectrum of $^{85}\text{Rb}^+$ ions.	55
4.1	Time-of-flight spectra of $A/q = 65$ at 225 and 226 laps.	62
4.2	Time-of-flight spectra of $A/q = 65$ at 227 laps.	63
4.3	Time-of-flight spectra of $A/q = 66$ at 223 and 224 laps.	64
4.4	Time-of-flight spectra of $A/q = 66$ at 225 and 226 laps.	65
4.5	Time-of-flight spectra of $A/q = 66$ at 227 and 229 laps.	66
4.6	Time-of-flight spectra of $A/q = 67$ at 223 and 224 laps.	67
4.7	Time-of-flight spectra of $A/q = 67$ at 225 and 227 laps.	68
4.8	Time-of-flight spectra of $A/q = 79$ at 224 and 225 laps.	69
4.9	Time-of-flight spectra of $A/q = 79$ at 227 and 228 laps.	70
4.10	Time-of-flight spectra of $A/q = 79$ at 229 laps.	71
4.11	Time-of-flight spectra of $A/q = 80$ at 224 and 225 laps.	72
4.12	Time-of-flight spectra of $A/q = 81$ at 221 and 222 laps.	73
4.13	Time-of-flight spectra of $A/q = 81$ at 224 and 225 laps.	74
4.14	Fit results of $A/q = 65$ series.	75
4.15	Fit results of $A/q = 66$ series.	75
4.16	Fit results of $A/q = 67$ series.	76
4.17	Fit results of $A/q = 79$ series.	76
4.18	Fit results of $A/q = 80$ series.	77
4.19	Fit results of $A/q = 81$ series.	77
4.20	Differences between the present measurement results and the AME16 values.	78
5.1	Diagram of the connection related to ^{67}Ge	79
5.2	Yields of γ -rays from $^{64}\text{Zn}(\alpha, n)^{67}\text{Ge}$ reactions.	80
5.3	Calculated yield curve of $^{64}\text{Zn}(\alpha, n)^{67}\text{Ge}$ reaction.	81
5.4	Diagram of the connections related to ^{81}Br	82
5.5	Decay measurement of ^{82}Br	83
5.6	Reported relative mass precisions and half-lives.	84
5.7	The systematic error as a function of relative mass difference	85
5.8	Fit parameter dependencies for ^{65}Ga mass excess value.	86
5.9	Predicted production cross-sections in the $^{\text{nat}}\text{S}(^{36}\text{Ar}, \text{X})$ reaction.	87
5.10	The rp -process path in the type I X-ray bursts for the end-point region	88
5.11	Experimental production cross section of proton-rich Ag to Sn isotopes	89
5.12	Upper part of the nuclear chart	90

Chapter 1

INTRODUCTION

The main aim of the present study was the reduction of the uncertainties of rapid proton capture process calculations that originate from the nuclear masses and thereby enable meaningful comparisons between theoretical models of type I X-ray bursts by precision mass measurements with $\delta m/m \lesssim 10^{-6}$ precision for key *rp*-process nuclei, which are located near the $N = Z$ line in the $A = 60 - 80$ region. Precision mass data of nuclei in the region of focus are valuable not only for *rp*-process nucleosynthesis, but also contribute to nuclear structure and possibly the standard model.

1.1 The *rp*-process pathway

Type I X-ray bursts are known as the most frequent explosive astronomical phenomenon in the universe, occurring on the surfaces of neutron stars in low-mass X-ray binary systems [1]. Comparisons of observed X-ray bursts with theoretical predictions can be used to extract information about the neutron star mass and radius, which in turn constrain the nuclear matter equation of state [2].

X-ray bursts can be explained by unstable thermonuclear burning of matter accreted from a stellar companion. The dominant reaction sequence is a rapid proton-capture process (*rp*-process). When the reaction path reaches weakly proton-bound or proton-unbound nuclei near the proton-drip line, then local equilibrium between proton capture (p, γ) and photo-dissociation (γ, p) is established, and the reaction flow waits at this point until β -decay allows further progress. The *rp*-process path strongly depends on the effective lifetimes of these waiting-point nuclei. The most crucial *rp*-process waiting-point nuclei are ^{64}Ge , ^{68}Se , and ^{72}Kr , since their long β -decay lifetimes are comparable to the typical burst duration of $\sim 10 - 100$ s. The effective lifetime of a waiting point nucleus (Z, N) is determined by the balance between the β^+ decay and local $(p, \gamma) - (\gamma, p)$ equilibrium with the $(Z + 1, N)$ nucleus. The abundance of the $(Z + 1, N)$ nucleus is dependent not only on local $(p, \gamma) - (\gamma, p)$ equilibrium, but also on the (p, γ) reaction rate to the $(Z + 2, N)$ nucleus. At lower temperatures (< 1.4 GK), the effective lifetimes of the (Z, N) waiting point is represented by the total destruction rate λ [7];

$$\begin{aligned} \lambda = & \lambda_{\beta^+, (Z, N)} + n_p \left(\frac{2\pi\hbar^2}{\mu_{(Z, N)} k_{\text{B}} T_9} \right)^{3/2} \frac{G_{(Z+1, N)}(T_9)}{G_{(1, 0)} G_{(Z, N)}(T_9)} \\ & \times \exp \left(\frac{11.605 Q_{p, (Z, N)}}{T_9} \right) \langle \sigma v \rangle_{(p, \gamma), (Z+1, N)}, \end{aligned} \quad (1.1)$$

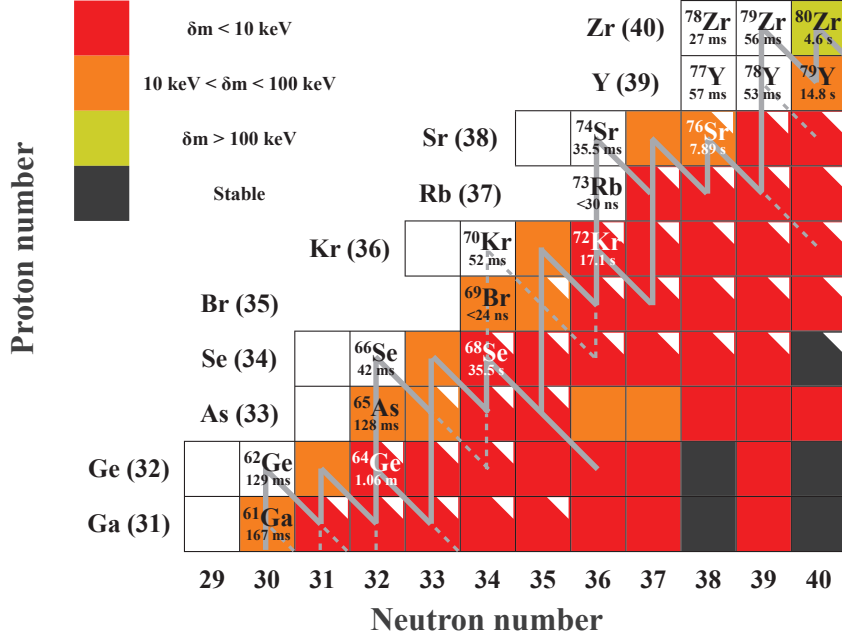


Figure 1.1: The rp -process path in the type I X-ray bursts for the $A \sim 60 - 80$ region. Each box is color-coded according to the experimental precision of corresponding nuclear mass. Red colored boxes satisfy the required mass precision for X-ray burst calculations. If there is no experimental mass value, the box has white background. White triangles indicate isotopes whose masses have been determined by Penning trap mass spectrometry. Nuclides denoted by black characters are key nuclei in the rp -process, as pointed out by Q -value sensitivity studies [3, 4]. Waiting-point nuclei are indicated with white lettering. The gray bold lines indicate reaction flows of more than 10% mass fraction and the dashed lines indicate reaction flows of 1% - 10%. This rp -process path is taken from [5].

where n_p is proton number density, T_9 is temperature in units of GK, k_{B9} is the Boltzmann constant in units of GK, μ is reduced mass of the proton-nucleus pair, and G is the partition function of the nucleus as a function of environmental temperature. Also λ_{β^+} , $\langle \sigma v \rangle_{(p,\gamma)}$, and Q_p are β^+ decay rate, proton capture cross section, and Q -value of the (p, γ) reaction in MeV, respectively. As the temperature exceeds ~ 1.4 GK, local $(p, \gamma) - (\gamma, p)$ equilibrium between the $(Z + 1, N)$ and $(Z + 2, N)$ nuclei is established and the total destruction rate λ depends on the Q -value of sequential two-proton capture reactions:

$$\begin{aligned} \lambda = & \lambda_{\beta^+, (Z, N)} + n_p^2 \left(\frac{2\pi\hbar^2}{k_{B9}T_9} \right)^3 \mu_{(Z, N)}^{-3/2} \mu_{(Z+1, N)}^{-3/2} \frac{G_{(Z+2, N)}(T_9)}{G_{(1, 0)}^2 G_{(Z, N)}(T_9)} \\ & \times \exp \left(\frac{11.605 Q_{2p, (Z, N)}}{T_9} \right) \lambda_{\beta^+, (Z+2, N)}. \end{aligned} \quad (1.2)$$

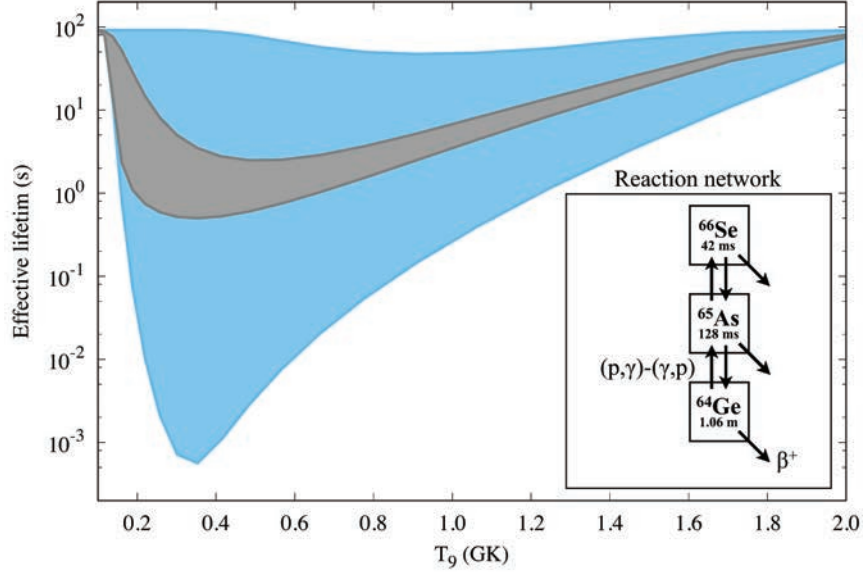


Figure 1.2: Effective lifetime of the waiting point nucleus ^{64}Ge . The light-blue area denotes the uncertainty of the effective lifetime, dominantly originating from mass uncertainties of ^{65}As ($\delta m = 85$ keV) [6] and ^{66}Se ($\delta m = 100$ keV) [7]. Reaction network used for determining the effective lifetime is indicated in a panel located at bottom-right. By reducing the both uncertainties to 10 keV, the uncertainty of the effective lifetime will be reduced to the size of the gray area. In this figure, masses were varied by $\pm 3\sigma$ and a proton density of $n_H = 10^6$ g/cm 3 was assumed.

In both temperature regions, the total destruction rate depends exponentially on one- or two-proton capture reaction Q -values. As these Q -values are determined via mass differences, the masses of waiting point nuclei (Z, N) and the $(Z + 1, N)$ and $(Z + 2, N)$ nuclei play important roles in determining the effective lifetimes. The uncertainties of the nuclear masses needed to determine these Q -values need to be smaller than about 10 keV to reduce the uncertainties of rp -process calculations [8, 9].

A status of mass measurements around the rp -process path is shown in Fig 1.1. The masses of the waiting-point nuclei, ^{64}Ge [10], ^{68}Se [11], and ^{72}Kr [12] have been measured in Penning traps at various facilities with precisions beyond that required for X-ray burst studies. However, among the six nuclides (^{65}As , ^{69}Br , ^{73}Rb , ^{66}Se , ^{70}Kr , and ^{74}Sr) which are the counterparts for calculating Q_p - and Q_{2p} -values, only the masses of ^{65}As and ^{69}Br have been determined experimentally, with uncertainties of 85 keV [6] and 40 keV [13], respectively. For the others, only theoretical predictions are available.

A effective lifetime of the most important waiting-point nucleus ^{64}Ge , which is evaluated by solving the smallest reaction network for determining that with the present mass data, is indicated by the light-blue area of Fig. 1.2. An uncertainty of the ^{64}Ge effective lifetime would decrease to the gray area of Fig. 1.2 as reducing the mass uncertainties of both ^{65}As and ^{66}Se to the required value for rp -process calculation, $\delta m = 10$ keV. In most of the temperature region of X-ray bursts, the uncertainty of the ^{64}Ge effective lifetime spans within an order of magnitude based on precision mass data satisfying the requirement, contrasting with the light-blue area which has the uncertainty of five order of magnitude

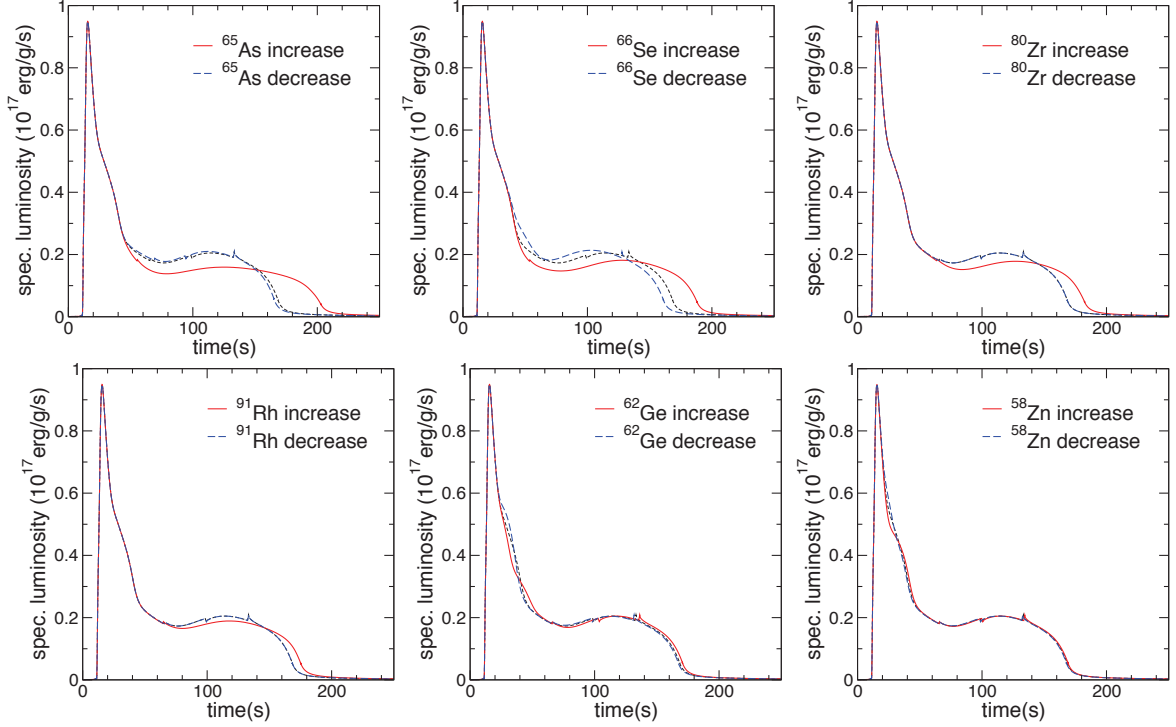


Figure 1.3: Nuclear mass dependence of the light curve in X-ray bursts. Black dashed lines indicate the baseline of theoretical model. Red solid (blue dashed) lines show the case of mass increase (decrease) by 3σ . This figure is taken from [4].

at maximum. This results indicate their masses have significant influences on the effective lifetime of waiting-point nucleus ^{64}Ge and high precision data of these masses are required to perform accurate rp -process calculation.

The influences of mass uncertainties to predicted light curves are indicated in Fig. 1.3. Effects of mass value differences can be found only in the tailing phase of light curves as the early, rise phase is dominated by (hot) CNO-cycle and the early part of rp -process. Three nuclides indicated in top row - ^{65}As and ^{66}Se - have especially large influences on light curve shapes of X-ray burst with present mass uncertainties. Thus, again, accurate and precise mass data for these nuclei are highly desirable in order to enable meaningful comparisons between theoretical models of type I X-ray bursts.

1.2 Other physics subjects related to region of focus

In the present study, we mainly focus on the key nuclei in the rp -process. The nuclei around the $N = Z$ line in this mass region also have direct impacts on several topics of nuclear physics, such as the unitarity of Cabibbo-Kobayashi-Masukawa matrix, the study of isospin symmetry breaking, and Coulomb energy studies in general through this unique proton-rich nuclear laboratory.

1.2.1 Unitarity of CKM matrix

High-precision experimental mass data of nuclides near the $N = Z$ line are also necessary for verification of the Standard Model through the unitarity of Cabibbo-Kobayashi-Masukawa (CKM) matrix. The ft -values of super allowed $0^+ \rightarrow 0^+$ β decay between $T = 1$ (T : isospin) analog states are related to the unitarity of CKM matrix via “corrected” $\mathcal{F}t$ -values [14, 15],

$$\mathcal{F}t \equiv ft(1 + \delta'_R)(1 + \delta_{\text{NS}} - \delta_{\text{C}}) = \frac{K}{2G_V^2(1 + \Delta_R^V)} \quad (1.3)$$

where $K = 8120.2776(9) \times 10^{-10} (\hbar c)^6 \text{ GeV}^{-4}\text{s}$, G_V is the vector coupling constant, δ_{C} is the isospin symmetry breaking correction, Δ_R^V is the transition-independent part of the radiative correction, δ'_R and δ_{NS} are radiative corrections of the transition-dependent part. G_V is directly connected to the up-down quark-mixing element V_{ud} of the CKM matrix via Fermi coupling constant G_{F} : $G_V = G_{\text{F}}V_{\text{ud}}$. The V_{ud} is the dominant term in the top-row sum of the CKM matrix, $|V_{\text{ud}}|^2 + |V_{\text{us}}|^2 + |V_{\text{ub}}|^2$, then V_{ud} is important for checking the unitarity of the CKM matrix.

To calculate the $\mathcal{F}t$ -values, the necessary nuclear parameters are partial lifetimes of the $0^+ \rightarrow 0^+$ transition and the corresponding Q_{EC} -values. For nuclear masses, a relative precision of $\delta m/m \lesssim 5 \times 10^{-8}$ is required. The unitarity of the CKM matrix is confirmed to the level of 1.2×10^{-4} with the uncertainties of present nuclear data [15].

To verify the unitarity of the CKM matrix more strictly, a reduction in the uncertainty of the corrected $\mathcal{F}t$ -value for masses of $N = Z$ nuclei with $A \gtrsim 60$ is required. Recently the mass of ^{74}Rb has been measured with a relative precision of $\delta m/m = 5.7 \times 10^{-8}$ by Penning trap mass spectrometry (PT-MS) [20, 21, 22]. However, there remain several nuclei – ^{66}As and ^{70}Br – that have non-negligible mass uncertainties, which can be seen in Fig. 1.4, and which we could reduce to a level capable of impacting on the verification of the unitarity of the CKM matrix.

The mass of ^{66}As has been measured by PT-MS at NSCL [10]. But unfortunately uncertainty of ^{66}As mass remains 30 keV and does not satisfy the requirement for impact on CKM, due to low statistics in that measurement. (In the 2016 Atomic Mass Evaluation [23, 19], the uncertainty of ^{66}As mass is evaluated to be 6 keV. However the reference to

Table 1.1: Experimental Q_{EC} -values of ^{70}Br . ΔQ_{EC} represents displacements of the experimental Q_{EC} -values from the Q_{EC} -value trend: $\Delta Q_{\text{EC}} \equiv Q_{\text{EC}}^{(\text{exp})} - Q_{\text{EC}}^{(\mathcal{F}t)}$, where $Q_{\text{EC}}^{(\mathcal{F}t)}$ is the Q_{EC} -value derived from presumption of the constancy of $\mathcal{F}t$ -value, $Q_{\text{EC}}^{(\mathcal{F}t)} = 9.96(5) \text{ MeV}$, and is taken from [16].

	Method	State of ^{70}Br	$Q_{\text{EC}}^{(\text{exp})} \text{ (MeV)}$	$\Delta Q_{\text{EC}} \text{ (MeV)}$	Ref
Dauids <i>et.al.</i> (1980)	β -endpoint	ground	9.97(17)	0.01(18)	[17]
Karny <i>et.al.</i> (2004)	β -endpoint	isomer ^a	9.90(8)	-0.06(9)	[16]
Savory <i>et.al.</i> (2009)	Penning trap	isomer ^a	10.505(15) ^b	0.54(5)	[11]

^a $E_{\text{X}} = 2292.3 \text{ keV}$, $t_{1/2} = 2.2 \text{ sec}$ [18]

^b ^{70}Se mass is adopted from [19]

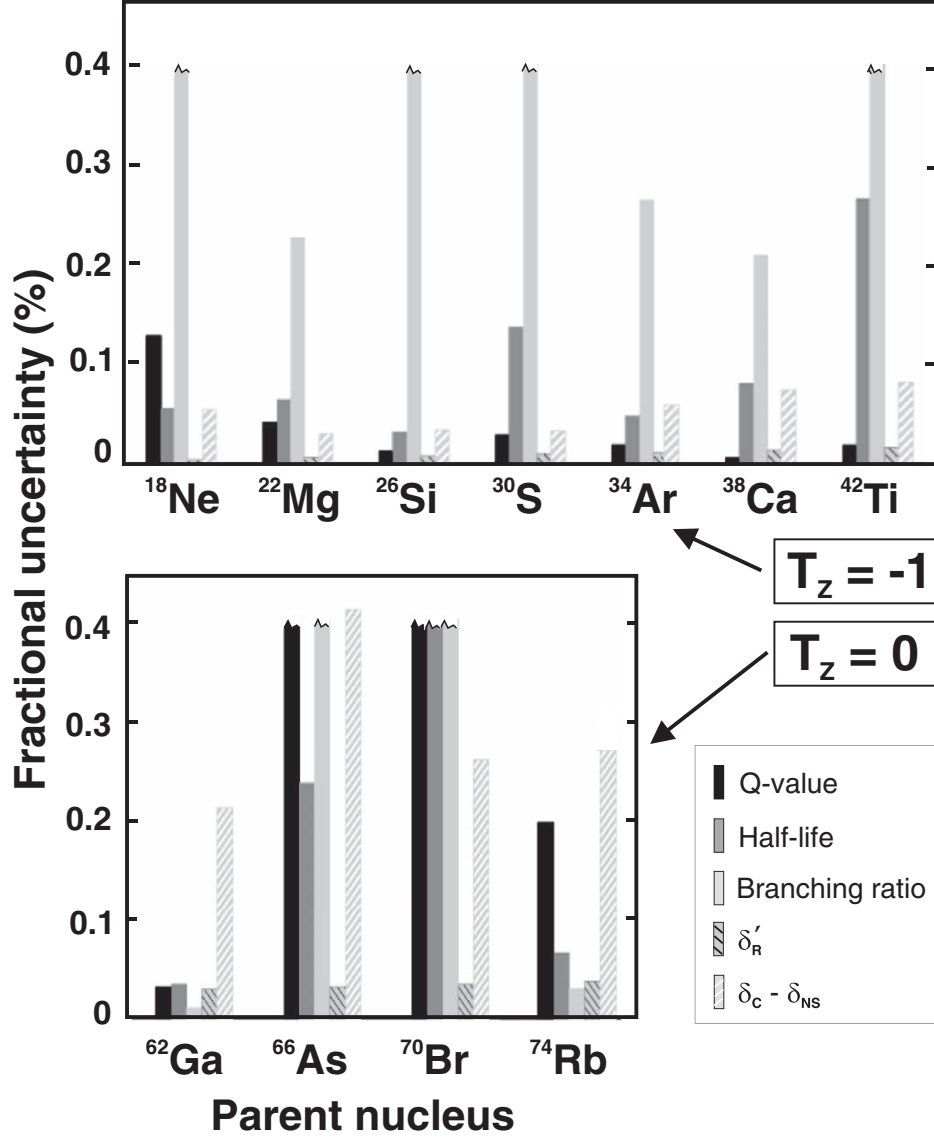


Figure 1.4: Histogram of the fractional uncertainties attributable to each experimental and theoretical input factor that contributes to the final $\mathcal{F}t$ -values. Errors with jagged lines have fractional uncertainties more than the 0.4%. This figure taken from [15]

this value is "private communication", thus 30 keV has been adopted in this thesis as the uncertainty of ^{66}As mass.)

The mass of ^{70}Br has been measured with two different techniques: PT-MS [11] and β -endpoint measurement [17, 16]; the results are summarized in Table 1.1. The β -endpoint measurements were performed on both ground and isomeric states of ^{70}Br and were consistent with each other. PT-MS has been applied to only isomeric state at in-flight fragmentation was highly favorable to production of the high-spin isomer. The mass value derived from PT-MS is outside of the Q_{EC} -value trend assuming the constancy of $\mathcal{F}t$ -value, which can be seen in the " ΔQ_{EC} " column of Table 1.1. Because PT-MS is a very accurate direct mass measurement technique, this discrepancy leads to some ambiguity about ^{70}Br mass value itself.

1.2.2 Coulomb displacement energy

Isospin symmetry is a concept introduced by Wigner [24], stating that in the hypothesis of charge independence, the nuclear forces between proton-proton, neutron-neutron, and proton-neutron are the same. Due to the Coulomb force the isospin symmetry is broken, and in the upper pf -shell, isospin non-conserving forces (INC) compete with multipole Coulomb effects, leading to a breakdown of the simple symmetry.

Coulomb displacement energy (CDE) is a term used to represent the isospin symmetry breaking. The CDE value D is defined by the difference between nuclear binding energies

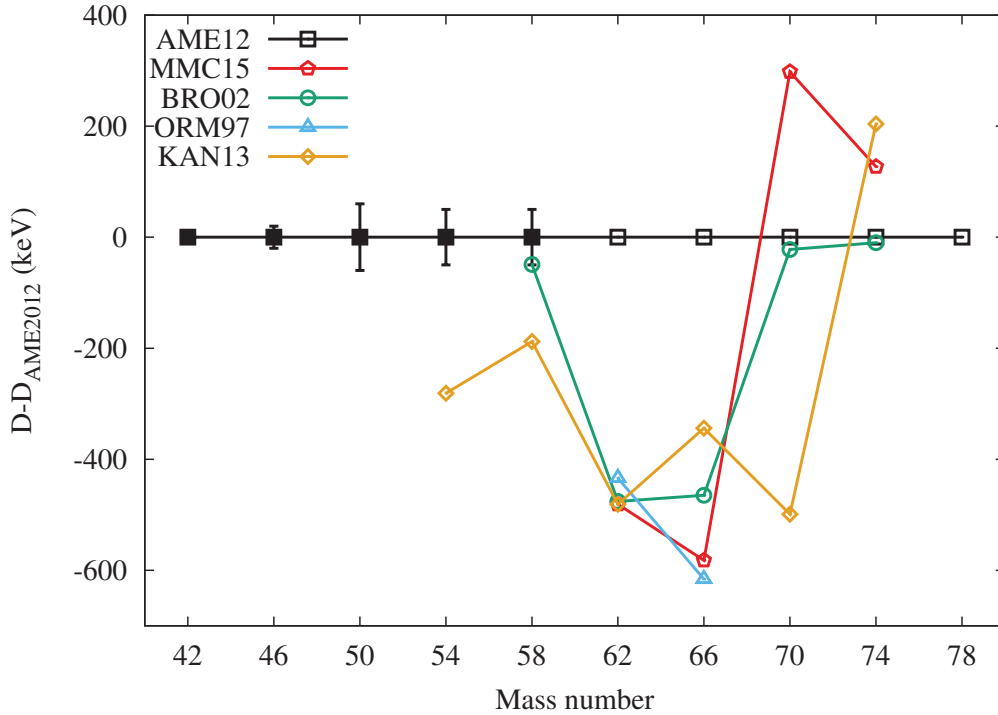


Figure 1.5: The CDE values among the even-even $N = Z - 2$ nuclei. Black filled squares represent experimental data while open symbols represent predictions. The models are discussed in the text.

BE of mirror nuclei,

$$D = BE(A, T_z^<) - BE(A, T_z^>), \quad (1.4)$$

where $T = |T_z^<| = |T_z^>|$ and $T_z = (1/2)(N - Z)$. For $T = 1/2$ nuclei, experimental data needed to calculate CDE exist for $A \leq 75$ excluding $A = 73$. In contrast to $T = 1/2$ nuclei, experimental data of $T = 1$ nuclei only exist for $A \leq 58$. Figure 1.5 shows several predictions of CDE for even-even $N = Z - 2$ nuclei. Labels in Fig. 1.5 are as follows: “AME12” uses the regional model of the Atomic Mass Evaluation [25], “MMC15” uses updated experimental information in a saturated non-spherical Coulomb estimate [26], “BRO02” [7] is a theoretical calculation based on the Skyrme Hartree-Fock method, “ORM97” [27] and “KAN13” [28] are shell model calculations including INC forces. By determining the masses of even-even $N = Z - 2$ nuclei in the region $Z \in (32, 40)$, we can constrain these models to further explore INC effects and multipole Coulomb effects.

Recent experiments on ^{66}Se [29], ^{70}Kr [30], and ^{74}Sr [31] identified three excited states up to 6^+ in ^{66}Se and two excited states, 2^+ and 4^+ , in both ^{70}Kr and ^{74}Sr . However, shell model calculations with state-of-the-art nuclear force plus INC effects have not been able to explain the excited states thus far.

No data exists at present to verify the INC effects using the CDE of $T = 1$ of nuclei heavier than $A = 62$, and only sparse and low-precision data exist in this region for $T = 1/2$ nuclei. The experimental mass data of the $N = Z - 2$ and $N = Z - 1$ nuclei in upper pf -shell are necessary for enabling the most stringent test of CDE calculations and could provide useful informations to constrain the INC description.

1.3 Nuclear mass determination techniques

There are two experimental ways to determine the nuclear masses: direct and indirect measurements. Here we will discuss both mass determination methods and their limitations. In the present study multireflection time-of-flight mass spectrograph was adopted as the preferred mass measurement method due to it alone satisfying the requirements of mass measurements for rp -process calculations.

1.3.1 Q -value determinations

Q -values are defined by the mass difference between initial and final states of a system:

$$Q \equiv \left[\sum_i M_i \right]_{\text{ini}} - \left[\sum_j M_j \right]_{\text{fin}}. \quad (1.5)$$

If all masses of related nuclei and/or particles, excluding an unknown mass M_X of nuclide X , are known, one can determine the M_X by using the Q -value with following relation,

$$M_X = \left[\sum_i M_i \right]_{\text{ini}} - \left[\sum_{j \neq X} M_j \right]_{\text{fin}} - Q. \quad (1.6)$$

Mass determinations with Q -values have been performed for wide regions of the nuclear chart by employing various reactions, such as, nuclear decays, particle induced reactions, transfer reactions with light nuclides, and breakup reactions.

Nuclear decays

Unstable nuclei change to more stable nuclei by undergoing nuclear decays with specific lifetimes. Q -value determinations have been made from α -decays, β^\pm -decays, and electron-capture (EC) decays. Their Q -values are calculated by

$$Q = \begin{cases} M_p - M_d - M_{4\text{He}} & (\text{for } \alpha) \\ M_p - M_d & (\text{for } \beta^-/EC) \\ M_p - M_d - 2m_e & (\text{for } \beta^+), \end{cases} \quad (1.7)$$

where the subscripts p and d represent parent and daughter nuclei, respectively, and m_e is the electron rest mass.

Being a two-body system, α -decay's have a discrete energy and Q_α -values can, in principle, be determined from single events, as compared with the three-body β^\pm/EC -decay for which Q -value determination requires interpretation of a decay spectrum produced by large numbers of events, as will be discussed later. The α -decaying nuclei are dominantly distributed in the $Z > 82$ region of the nuclear chart. In particular, most of the masses of (super)heavy nuclei have been determined by observing their α -decay chains down to known mass nuclei. Precisions of this method correspond to energy precision of the α -particle detectors employed. If silicon semiconductor detectors are employed for α -decays and high statics data are available, uncertainties of $\delta E_\alpha \lesssim 10$ keV are expected. However there are no guarantees that the observed α -particles represent ground state to ground state transitions. In order to avoid this problem, α - γ spectroscopy has begun to be utilized for more accurate Q_α -value measurements [32].

β^+ - (β^- -) decays are three-body systems of decaying nuclei, positron (electron), and electron-(anti)neutrino. Therefore the emitted positrons (electrons) have a continuous energy distribution. To determine Q_{β^\pm} -values, maximum energies of positron or electron are necessary, which can be measured in several ways, such as classical Kurie plot analysis, shape-fitting techniques, and other spectrometric methods. For all cases the response functions of the detector must be well understood for accurate and precise measurements. These measurement methods can be applied for β^- -decay. In the case of β^+ -decay, emitted positrons produce pair-annihilations with electrons of the detector materials and emit two 511 keV γ -rays that affects the detected positrons' energies. A summation-free β^+ -endpoint spectrometer had to be employed for Q_{β^+} -value determination to avoid this difficulty [33]. This spectrometric method uses a coincidence gate with two 511 keV annihilation γ -rays and to prevent overestimating the observed positron energies.

Accurate and precise mass measurements via nuclear decay Q -value determinations need the well understood response functions of detectors, accurate detector calibrations, and high statistics data. In addition, identification of each transition originating from the observed events is important for removing the ambiguities of excited states. These Q -value determination techniques could provide precision mass values, which satisfy the requirement of rp -process calculations. But decay properties of the nuclei in this study have not been clarified yet and the yields of many are insufficient for such techniques. We cannot rely on the accuracy of mass data that might be obtained and thus exclude the Q -value measurements as a mass determination method in the present study.

Nuclear reactions

Mass determinations via nuclear reactions have been widely used and can be applied for the entirety of the nuclear chart. Various nuclear reactions, e.g., knockout reactions, transfer reactions, charged-particle induced reactions, and neutron-capture reactions have been employed for this purpose.

If one can obtain the all information of nuclei related to a certain reaction, such as momentums and their excited states, the reaction Q -value can be extracted from them through conservation of momentum and energy. In this way accessible nuclei are limited under the combinations of stable isotopes. Then in order to access the nuclei far from stability, a few nucleon transfer or knockout reaction of unstable, exotic isotopes are used. Reaction Q -value determination via these reactions is an effective technique for unstable, very short lived (less than micro-seconds) nuclei. Mass measurement of the proton-unbound nucleus ^{69}Br has been performed with a proton-induced neutron-knockout reaction of ^{69}Se beam and via coincidence measurement of the $^{69}\text{Br} \rightarrow p + ^{68}\text{Se}$ decay products [13]. As a result, a resonance state of ^{69}Br was observed and its mass excess value was deduced to be $ME(^{69}\text{Br}) = -46115_{-34}^{+40}$ keV. However, the possibility of suppression of the ground state by population of the proton-decaying isomeric state has been pointed out [34] and there is uncertainty that this mass excess value corresponds to the ground state. This kind of ambiguity is always appearing due to an uncertainty of the population of the produced nuclear states.

If reaction Q -value is negative, the reaction has a threshold energy. Considering a nuclear reaction $A(a, b)B$, which has negative Q -value Q_{reac} , threshold energy of this reaction E_{th} can be written as

$$E_{\text{th}} = -\frac{M_A + M_a}{M_A} Q_{\text{reac}}, \quad (1.8)$$

where M_A and M_a are masses of nuclei A and a , respectively. By measuring the yield of produced nucleus “ B ” via γ -ray detection as a function of the initial energy of the reaction system, E_{th} can be determined as the point where the yield becomes nil. Equation 1.8 is valid only for ideal situations. Actual measurements have been performed with reactions between charged-particles and then the correction of Coulomb barrier between them C_{Coulomb} is necessary;

$$E_{\text{th,measure}} = E_{\text{th}} + C_{\text{Coulomb}}. \quad (1.9)$$

The correction C_{Coulomb} is evaluated theoretically and results depend on the adopted theoretical model. Thusly obtained mass values, thereby, have an ambiguity originating from the theoretical models.

Mass determination via neutron-capture, (n, γ) reactions, are known to be an accurate and precise method. Neutron irradiations are performed with thermal neutron source such as reactors. Because the thermal neutron energy is extremely small, $\sim 10^{-2}$ eV, initial excited state of compound nuclei has a mass, $M(^{A+1}Z^*)$, equal to summation of the masses of the target nucleus $M(^AZ)$ and a neutron M_n ,

$$M(^{A+1}Z^*) = M(^AZ) + M_n. \quad (1.10)$$

The difference between mass of the initial excited state $M(^{A+1}Z^*)$ and that of its ground state $M(^{A+1}Z)$ is the Q_n -value. If all of the γ -ray transitions are observed, one can reconstruct the excited states up to the initial compound state by utilizing Rydberg-Ritz combination principle and can extract the Q_n -value. Rydberg-Ritz combination principle

is a theory in atomic physics to explain the relationships of the spectral lines; if two lines with different frequencies ν_1 and ν_2 are observed, another line ν_3 satisfying the following equation must be exist,

$$\nu_1 + \nu_2 = \nu_3 \quad \text{or} \quad |\nu_1 - \nu_2| = \nu_3. \quad (1.11)$$

By assuming the analogy extends from atomic transitions to nuclear transitions, γ - γ coincidence informations allow determination of each excited state and thereby the Q_n -value. The precision of this method depends only on the energy resolution of the γ -ray detector, with typically $\delta Q_n \lesssim 1$ keV is expected if germanium detectors are employed. The Q -value determination via (n, γ) reaction is a very accurate and precise technique but it can be applied only for nuclides near stability due to its need both of macroscopic amounts of target material and lifetime long enough for irradiation and handling.

1.3.2 Direct measurements at intermediate- and high-energies

The mass of intermediate- or high-energy ions can be measured through determination of time-of-flight (TOF) and/or magnetic rigidity. Techniques have been developed for performing such measurements in both single-pass and ion storage regimes. A feature of these technique is use of highly or even fully stripped ions which can be provided in high energy reaction production mechanisms such as in-flight fragmentation of relativistic heavy ions.

Single-pass methods

The magnetic rigidity of a ion which has velocity β is represented by

$$B\rho = \frac{\gamma m_0}{cq} \beta, \quad (1.12)$$

where m_0 and q are the ion's rest mass and an its charge state, respectively, and γ is the Lorentz factor: $\gamma = 1/\sqrt{1 - \beta^2}$. By measuring both momentum and TOF of the ion, one can determine the ion mass m_0 . The flight paths of ions slightly depend on both the charge states and momentum of the ions. Thus the ion mass can be deduced by a certain function of the charge state and the TOF t ,

$$m_0 = f(q, t). \quad (1.13)$$

The form of the function $f(q, t)$ depends on the details of the experimental setup and is characterized and calibrated by utilizing known mass nuclei. This TOF- $B\rho$ technique has been performed in several facilities.

One such device to have employed the TOF- $B\rho$ technique for mass measurements is the high resolution fragment spectrometer SPEG at GANIL. An intense, $\sim 10^2$ pA, primary heavy-ion beam at intermediate energy (50 - 100 MeV/nucleon) can be used in this facility and can provide exotic nuclides by in-flight fragmentation reactions. Mass measurements have been performed for mainly light, $A < 80$, neutron- and proton-rich nuclei [35, 36, 37]. Mass resolving powers have been reported in the range of $R_m = 2500 - 5000$ and the mass uncertainties of these measurements are typically $\delta m \geq 100$ keV.

Mass measurements have also been carried out with the A1900 fragment separator combined with the S800 spectrograph at NSCL. There, intermediate-mass, neutron-rich nuclei far from β -stability produced by the fragmentation reactions of 100 MeV/nucleon

^{84}Kr and 140 MeV/nucleon ^{82}Se primary beams were utilized. Mass resolving powers reaching $R_m = 5600$ were reported [38]. The precision of these measurements are smaller than 1 MeV but do not reach 100 keV.

At RIKEN, the SHARAQ spectrometer has been developed in collaboration with University of Tokyo's Center for Nuclear Science. The SHARAQ spectrometer has been used to perform mass measurements of neutron-rich calcium isotopes beyond the new magic number $N = 34$ [39]. In the case of ^{55}Ca , the mass value was determined with relative mass precision of $\delta m/m \sim 3 \times 10^{-6}$, which corresponds to a mass uncertainty of $\delta m \sim 150$ keV.

The required measurement time of the TOF- $B\rho$ technique, determined by the time needed to pass through the beam lines, is typically $t \lesssim 1$ μsec . This measurement time allows access to the very shortest-lived, most exotic nuclei. But the measured mass precision is limited to ~ 100 keV, which is too large for the requirements of the present study, that being $\delta m < 10$ keV.

Storage rings

In general, extending the flight path of the ions can improve the achievable mass precision. It was noted by H. Wollnik in the 1980s [40] that if one could increase the curvature of the analyzing magnets to create a closed storage loop, the flight path could be arbitrarily long. This is the basis of the magnetic storage ring spectrometer. Consider two ions, differing in mass by $\Delta(m/q)$, circulating in a magnetic storage ring. The ability to distinguish between the two ions – the mass resolving power – is given, to first order approximation, by [41]

$$\frac{\Delta(m_0/q)}{m_0/q} = \frac{1}{\gamma_{\text{tr}}^2} \frac{\Delta t}{t} + \left(\frac{1}{\gamma_{\text{tr}}^2} - \frac{1}{\gamma^2} \right) \frac{\Delta v}{v} + \frac{1}{\gamma_{\text{tr}}^2} \frac{\Delta B}{B}, \quad (1.14)$$

where $\Delta t/t$ and $\Delta v/v$ are the TOF resolution and velocity spread, respectively. The Lorentz factor γ_{tr} corresponds to the so-called transition energy, which is a constant characteristic for the ion-optical setting of a given storage ring. The third term $\Delta B/B$ is the non-uniformity of the magnetic field integrated over the all paths of the ring. If the contribution of the magnetic non-uniformity term can be made negligible, the mass resolution is limited only by the velocity and time spread terms.

There are two ways to removing the contribution of the velocity spread term: reduction of the velocity spread Δv and tuning of the ring optics such that $\gamma \rightarrow \gamma_{\text{tr}}$. The former way is called Schottky mass spectrometry (SMS) [42], while the latter is referred to as isochronous mass spectrometry (ISM) [43]. The heavy ion storage ring ESR [44] at GSI can employ both mass measurements via SMS and ISM. To perform SMS, the velocity spread $\Delta v/v$ of the stored ions can be reduced by the electron cooling method. In this method, the reduction of the velocity spread is achieved by ion cooling via stochastic Coulomb interaction between cold electrons and can reach $\Delta v/v = 5 \times 10^{-7}$ [42]. The electron cooling requires at least 30 sec to suppress the velocity spread for heavy ions, which initially have $\Delta v/v \sim 10^{-3}$. Mass measurement with ESR-SMS has been applied to a wide region of the nuclear chart. The ESR operated in SMS mode has achieved high-precisions even in cases of only one ion for a certain nuclide, because the ion will be detected each time it passes through the Schottky pickup. The precisions of the measurements, dominated by systematic errors, have been evaluated to be 10 keV in one experiment for neutron-rich platinum to uranium isotopes [45].

Mass measurements via ISM have been performed in ESR and CSRe [46] at IMP. In addition, Rare-RI Ring (R^3) [47], has been constructed and developed for mass measure-

ment of short-lived, rare isotopes via ISM at RIKEN. ISM does not need long measurement time, in contrast with SMS, a typical measurement duration being only $\sim 10^1 \mu\text{sec}$. Mass measurements via ESR-ISM have been carried out for intermediate- and light-mass nuclides on both the neutron- and proton-rich side of β -stability. The mass uncertainties of these measurements are typically in the order of $\delta m \gtrsim 100 \text{ keV}$. CSRe has performed mass measurements mainly for proton-rich nuclei and reported [48] mass precisions reaching down to a level of 10 keV. However, in the case of ^{52}Co , a discrepancy between the mass-value measured by PTMS [49] has been noted. Measured mass excess values of ^{52}Co are $ME_{\text{CSRe}}(^{52}\text{Co}) = -34361(8) \text{ keV}$ and $ME_{\text{PTMS}}(^{52}\text{Co}) = -34331.6(66) \text{ keV}$, showing a difference between them of $\Delta ME(^{52}\text{Co}) = 29(10) \text{ keV}$. Deferring to the historical accuracy of PTMS, this indicates that there is still some room to discuss the limits of accuracy in error evaluations of high-precision measurements with CSRe. R³ does not have any mass measurement results yet. However, the non-uniformity of the magnetic field in the beam line of R³ has been evaluated to be 1.3×10^{-4} [50], leading to the relative mass precision being limited to $\delta m/m \gtrsim 10^{-6}$. This limitation corresponds to a mass uncertainty of $\delta m \sim 56 \text{ keV}$ for $A = 60$ nuclei.

The required measurement time of SMS is several orders of magnitude longer than the half-lives of the nuclei of interest ($t_{1/2} \lesssim 10^2 \text{ msec}$) in the present study. ISM can be applied to for very short-lived nuclei, but the precision of the measurements do not satisfy our requirement of $\delta m < 10 \text{ keV}$.

1.3.3 Direct measurements at low-energy

Penning trap mass spectrometry (PT-MS) is known as the most accurate and precise direct mass measurement technique using low-energy ions.

Penning traps store ions via a static electromagnetic field, which consists of the superposition of a homogenous magnetic field $\vec{B} = (0, 0, B)$ and weak axisymmetric electrostatic field $\Phi(z, r) = U_{\text{DC}}(z^2 - r^2/2)/2d^2$, where U_{DC} is the direct current potential applied on the ring electrode and $2d^2 = (z_0^2 - r_0^2/2)$. An ion having mass m and charge state q moves in the Penning trap with a complex motion that has three eigenfrequencies,

$$\omega_z = \sqrt{\frac{qU_{\text{DC}}}{md^2}}, \quad (1.15)$$

$$\omega_{\pm} = \frac{\omega_c}{2} \pm \sqrt{\frac{\omega_c^2}{4} - \frac{\omega_z^2}{2}}, \quad (1.16)$$

where ω_c is cyclotron frequency of the ion, $\omega_c = qB/m$. The eigenfrequency ω_z characterizes the axial motion, while the radial motion is characterized by a slow $\vec{E} \times \vec{B}$ drift known as magnetron motion (characterized by ω_-) and the faster reduced cyclotron motion (characterized by ω_+). The sum of the two radial eigenfrequencies ω_{\pm} is equals to the cyclotron frequency,

$$\omega_c = \omega_+ + \omega_-, \quad (1.17)$$

which depends only on the magnetic field. Direct measurement of this summed frequency enables mass measurements via comparison with a reference ion,

$$m = \frac{\omega_{c,\text{ref}}}{\omega_c} m_{\text{ref}}. \quad (1.18)$$

Measurement of ω_c is done by resonant excitation of the ion motion. The ion's radial motions can be resonantly excited via an azimuthal quadrupole radio-frequency (RF) signal

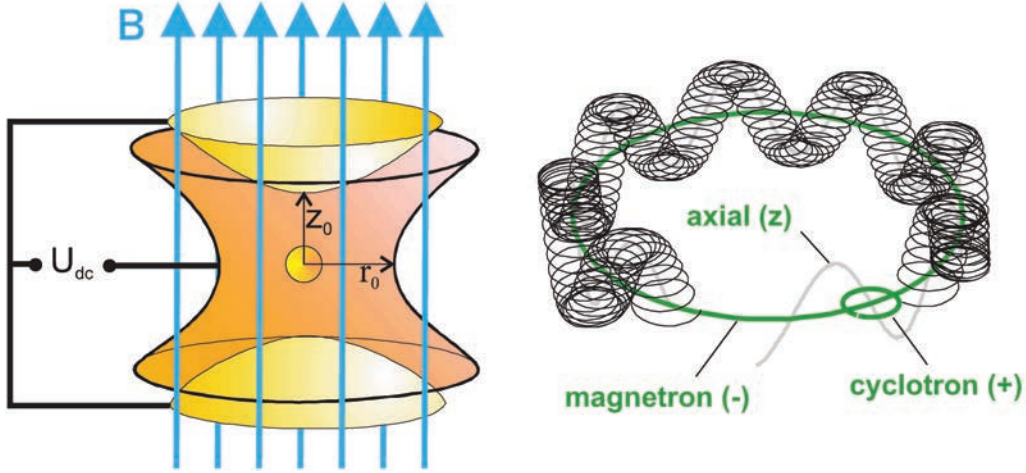


Figure 1.6: Schematic view of Penning trap and ion circular motion in it.

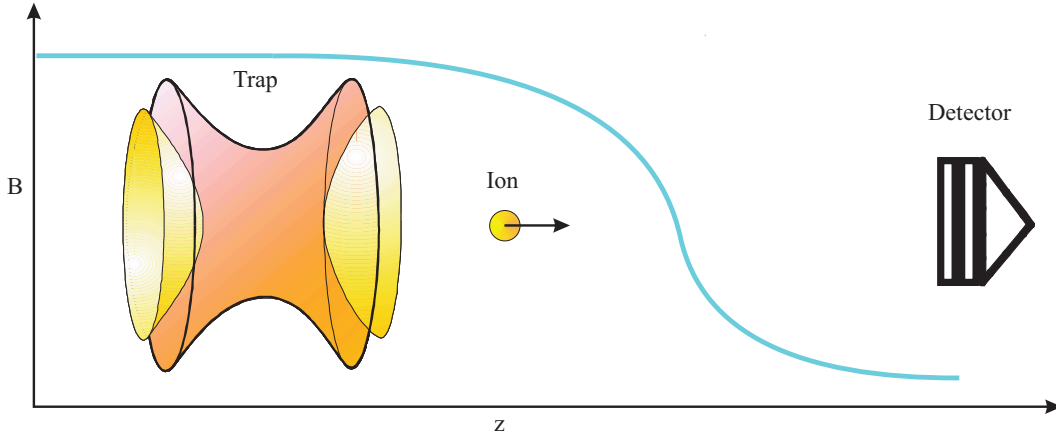


Figure 1.7: Schematic of time-of-flight ion-cyclotron resonance detection technique. Acceleration of ejected ion via magnetic field gradient force.

$U_{\text{exc}}(t)$. The time-of-flight ion-cyclotron resonance (TOF-ICR) detection technique is commonly used for cyclotron frequency measurements [51]. When ejected from the Penning trap, an ion will pass through the non-uniform magnetic field and experience the gradient force \vec{F} from the decaying B-field,

$$F_z = -\frac{E_r}{B} \frac{\partial B}{\partial z}, \quad (1.19)$$

converting its radial kinetic energy E_r into axial kinetic energy. Therefore an ion's TOF is related to the radial motion of the trapped ion and one can determine the resonant frequency ω_c through systematic measurement of the ion's TOF as a function of the frequency of the applied external field U_{exc} . In TOF-ICR measurements, the Penning trap should accept only one ion at a time to remove space charge effects, which can induce significant systematic errors. Thus measurements are performed one ion at a time.

Mass resolving power of PT-MS is evaluated by the following relation [51],

$$R_m = \frac{\omega_c}{\Delta\omega_c} \approx \nu_c T_{\text{exc}}, \quad (1.20)$$

where $\nu_c = \omega_c/2\pi$ and T_{exc} is time for RF excitation in Penning trap. For singly-charged, medium mass ions in a trap with $B \gg 1$ T, the cyclotron frequency is on the order of megahertz. While the maximum excitation time is limited by the collisions between the ion and neutral background gas particles, $T_{\text{exc}} \geq 1$ sec is common. Thus mass resolving power of PT-MS typically exceeds the level of $R_m = 10^6$ for long-lived ions. The accuracy limit of PT-MS mainly comes from fluctuations in the magnetic field during measurements, since simultaneous measurement of both analyte and reference ions is not performed. Superconductivity magnet can provide a homogeneity of typically $\Delta B/B < 10^{-8}$ over a volume of 1 cm^3 and a stability of the field of $(\Delta B/B)/\Delta T < 10^{-8}/\text{hr}$ [52] and give high accuracy and precision to mass measurement via PT-MS.

PT-MS requires measurement time, and consequently achievable mass resolving power, is limited by the life-time of the analyte ion. Additionally, PT-MS requires a pre-cooling process before the measurement. The PT-MS have been applied for several short-lived isotopes, such as, in the range of $t_{1/2} < 100$ msec, ^{11}Li [53], $^{32-34}\text{Mg}$ [54], ^{32}Ar [55], $^{64-66}\text{Mn}$ [56], ^{74}Rb [20, 21, 22], and $^{99,100}\text{Rb}$ [57], and the shortest one is ^{11}Li of $t_{1/2} = 8.8$ msec. In the case of ^{74}Rb which has half-life of 65 msec, the measurements were performed by using ISOLTRAP at ISOLDE/CERN. A cooling and bunching time of $\lesssim 200$ msec was required and the excitation times from 60 msec to 120 msec were used. Considering the cyclotron frequency of $^{74}\text{Rb}^+$ was $\omega_{c,74\text{Rb}} = 1.2$ MHz, the mass resolving power can be determined to be $R_m \approx 7.2 \times 10^4 - 1.4 \times 10^5$. The precision of $\delta m = 3.9$ keV required accumulation of 10^4 events. This mass resolving power is comparable to that of the multireflection time-of-flight mass spectrograph (MRTOF-MS) discussed below. By considering decay loss in the cooling, bunching, and excitation processes, MRTOF-MS has advantage in achieving precision mass measurements for such short-lived nuclei.

1.3.4 Multireflection time-of-flight mass spectrograph

Overview of multireflection time-of-flight mass spectrograph

The mass resolving power of a TOF mass spectrograph is related to a TOF value t and a width of TOF distribution Δt by

$$R_m \propto \frac{t}{\Delta t}. \quad (1.21)$$

Then in order to achieve high mass resolving power in TOF mass spectrometry, the TOF width Δt must be as short as possible compared to TOF t . This requires a long flight path. One solution satisfying this requirement is the storage ring, discussed in Section 1.3.2. The MRTOF-MS is another solution that enables high mass resolving power. MRTOF-MS devices consist of at least two electrostatic ion mirrors, which can reflect the ions back and forth, and a field-free drift region, to provide a long flight path. Initial type of MRTOF-MS device had U-shaped configuration, which consists of three mirrors, but its transmission efficiency decreased with increasing numbers of laps due to optical aberrations [58]. In order to avoid this optical aberration issue, current MRTOF-MS devices have rotationally symmetric coaxially arranged mirror electrodes [59], which is shown in the upper panel of Fig 1.8.

The TOF difference between two ions with differing mass, which travel the same flight path with the same non-relativistic kinetic energy, depends only on the square root of their mass ratio. In real-world measurements, to account for imperfect synchronization between the start of the ion motion and the start of the measurement clock, the measured TOF, t_{obs} , must include additional systematic offset t_0 ,

$$t_{\text{obs}} = (a + b \cdot \ell) \sqrt{m} + t_0, \quad (1.22)$$

where ℓ represents the number of laps an ion makes between the mirrors, and a and b are constants related to the single, non-reflection flight path and length of flight path between consecutive reflections from one of the mirrors, respectively. A part of the first term enclosed by brackets depends only on the ion energy and can be treated as a constant within same lap number. Then in order to determine the mass of a certain nuclei, two reference nuclei are necessary due to there being two unknown parameters: $(a + b \cdot \ell)$ and t_0 . If the value of t_0 is determined independently, *e.g. by direct measurement*, it allows the

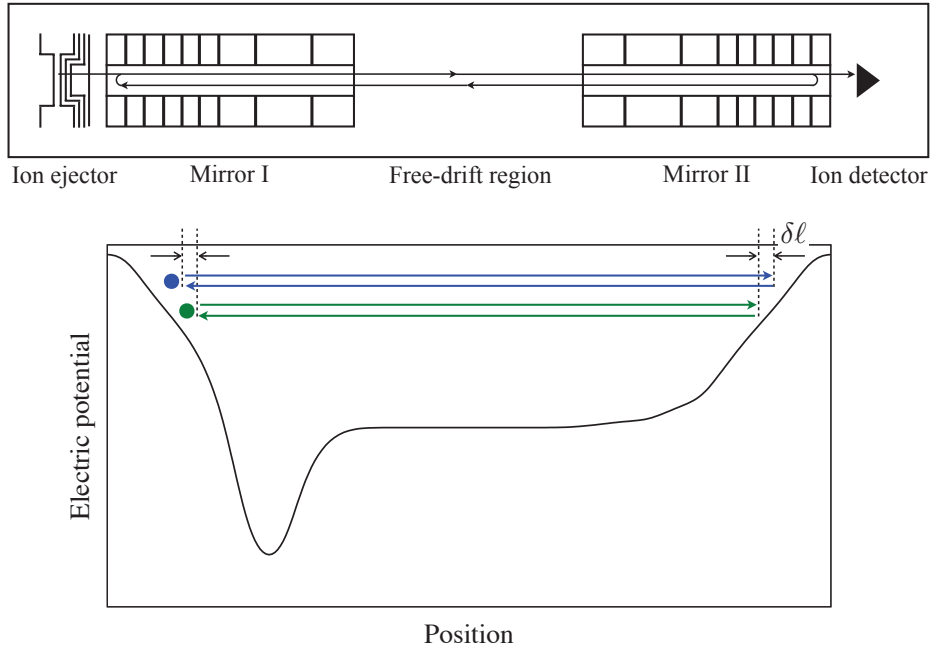


Figure 1.8: (Upper panel) Schematic view of coaxial multireflection time-of-flight mass spectrometer. (Lower panel) Conceptual view of energy isochronicity in multireflection time-of-flight mass spectrograph (MRTOF-MS). The blue and green dots represent ions, wherein the blue ion has slightly higher energy than the green ion. The less energetic ion has a velocity v , while the more energetic ion has a velocity $v + 2\delta\ell/t$. Each lap in the MRTOF-MS, the more energetic ion flies along a path which is $2\delta\ell$ longer than that of the low energy ion. In this way, the circulation time is not energy dependent. The dip in the mirror potential on the left side represents an Einzel lens, providing spatial refocusing each lap.

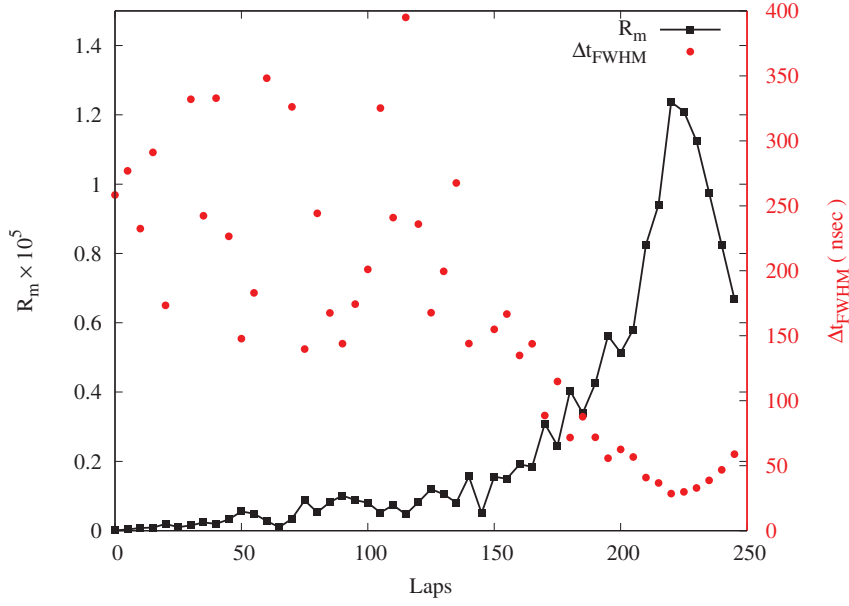


Figure 1.9: Scan over lap number to determine number of laps at which the ions achieve a time focus.

use of single reference methods,

$$m = \left(\frac{t - t_0}{t_{\text{ref}} - t_0} \right)^2 m_{\text{ref}}. \quad (1.23)$$

In this study the single reference method has been adopted. The details and error evaluation of this method will be discussed in Section 3. Because the mass has a second-order dependence on TOF, the mass resolving power in terms of time spread of the detected ion pulse is given by

$$R_m = \frac{t}{2\Delta t}. \quad (1.24)$$

The MRTOF-MS produces a minimal time spread by usage of electrostatic ion mirrors, between which ions reflect, allowing the flight path to be extended to great lengths. By designing the shape of the mirror potentials to cancel out the ion's energy dispersion, a so-called energy-isochronous condition analogous to $\gamma = \gamma_{tr}$ in the magnetic storage ring, the time spread can be minimized and thereby the mass resolving power can be maximized. A conceptual view of the energy-isochronous condition is shown in the lower panel of Fig 1.8. Ions injected into the MRTOF device have typical energy dispersion of $<2.5\%$. Each mirror's potential gradient causes energetic ions to travel a slightly longer path than the that of lower-energy ions, removing energy dependence from the ion's TOF. Additionally, the potentials during ion injection create a condition that places a so-called time-focus at a great distance (typically ~ 100 m). The time spread is minimized at the time-focus.

Thus there is an optimum lap number ℓ_{pot} that maximizes the mass resolving power for each MRTOF device and setting. Once the lap number (flight length) exceeds ℓ_{pot} -value, the time spread increases and the mass resolving power decreases; this is analogous to the divergence seen following a spatial focus in an optical system. This behavior, lap number dependence of mass resolving power, is clearly shown in Fig 1.9.

The MRTOF-MS is a powerful mass measurement technique due to its short processing time, in the range of a few to several ten milliseconds, and large mass resolving power $R_m \gtrsim 10^5$. Therefore MRTOF-MS is a well-suited mass measurement technique for the requirements of the present study.

Ion capturing and ejection techniques and mass bandwidth of measurements

There are two options for capturing ions in and ejection ions from the MRTOF: mirror switching and in-trap potential lift [60]. Their schemes are indicated in Fig 1.10. The main advantage of in-trap potential lift is that ion transfer energy does not affect the trapping conditions as long as $E_{\text{transfer}} - q\Delta U_{\text{lift}} = \text{Const.}$, where E_{transfer} is the ion transfer energy and ΔU_{lift} is the lift potential. This means changes of mirror potential are not necessary during the measurements. It is an effective and efficient way to achieve both high resolving power and good stability.

However, the in-trap potential lift technique has a disadvantage in mass bandwidth – the mass range that can be measured simultaneously. The acceptance time window t_{lift} of the in-trap potential lift technique can be evaluated as

$$t_{\text{lift}} = \frac{l_{\text{lift}}}{v_{\text{ion}}} = l_{\text{lift}} \sqrt{\frac{m_{\text{ion}}}{2E_{\text{transfer}}}}, \quad (1.25)$$

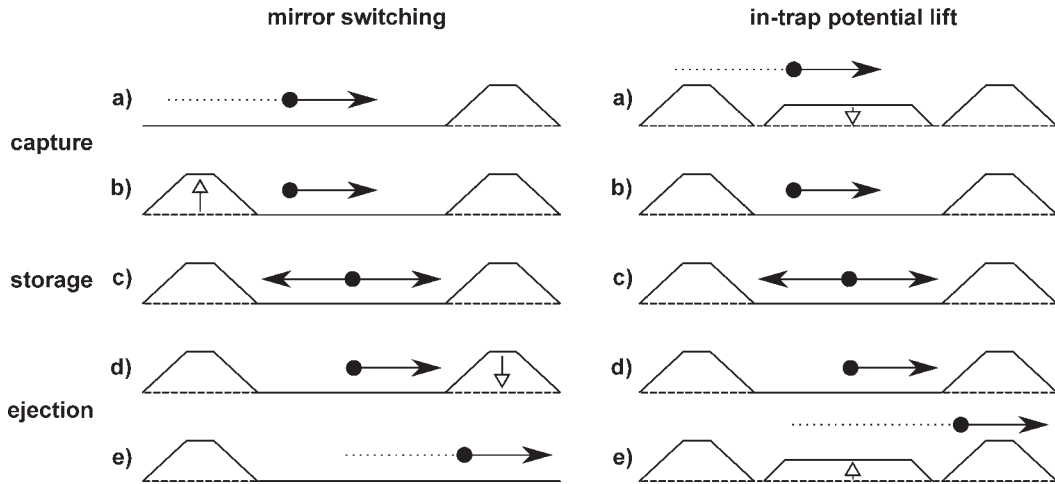


Figure 1.10: Schematic view of ion capturing and ejection in MRTOF. (Mirror switching) An entrance mirror is lowered when bunched ions come (a). After the ions passed the entrance mirror, the mirror is raised to the trapping value (b). Then ions are trapped between the mirrors (c). Similarly, the potential of the exit mirror is lowered to eject the ions (d). Ions can exit from MRTOF (e). (In-trap potential lift) Ions having $E_{\text{transfer}} > qU_{\text{trap}}$ pass through the first mirror and enter the drift region (a). When ions flight drift region, the in-trap lift is activated, *i.e.*, a potential ΔU_{lift} is applied (b). Then ions are trapped as their energy is no longer high enough to pass the mirrors (c). Ions are trapped with a certain number of reflection (d). The in-trap lift voltage is applied when ions flight the drift region, then they are regaining enough energy to leave the potential well of MRTOF (e). This figure is taken from [60].

where v_{ion} and m_{ion} are the velocity and mass of the transferring ion, respectively, and l_{lift} is the length of the drift region. By assuming $m_{\text{ion}} = 60u$, $E_{\text{transfer}} = 5 \text{ keV}$, and $l_{\text{lift}} = 30 \text{ cm}$, one can readily calculate that $t_{\text{lift}} = 2.4 \text{ } \mu\text{sec}$. This time window can cover a mass range of $\Delta m/m \approx 0.1\%$ if the total TOF is 5 msec.

In contrast with the in-trap potential lift, the mirror switching technique can enable wide mass bandwidth measurements. Consider a situation where two different ions, which have unequal masses $m_1 \neq m_2$, have the same TOF, namely

$$(\zeta + \ell_1)b\sqrt{m_1} = [\zeta + (\ell_1 + \Delta\ell)]b\sqrt{m_2}, \quad (1.26)$$

where $\zeta = a/b \approx 0.7$ and $\Delta\ell$ is a difference of the number of laps. The mass bandwidth is defined as the maximum fractional mass range which is capable of simultaneously making the same number of reflections, which corresponds to a limitation of $|\Delta\ell| \rightarrow 1$. Thus one can find mass bandwidth by solving Eq. 1.26 by rewriting m_2 as $m_1 + \Delta m$ [61],

$$\frac{\Delta m}{m} = \frac{2(\zeta + \ell_m) + 1}{(\zeta + \ell_m)^2}, \quad \ell_m = \frac{\sqrt{m_2}}{\sqrt{m_2} - \sqrt{m_1}} - \zeta. \quad (1.27)$$

In the case of Fig. 1.9, the optimum, time focusing lap number is about 125, then mass bandwidth can be estimated to be $\Delta m/m \approx 1.6\%$. This value represents an upper limit of mass bandwidth. The effective mass bandwidth is reduced by the switching of the ejection mirror: when the ions are ejected from MRTOF, the mirror potential is lowered to allow ions to pass through the mirror (processes (d) and (e) in mirror switching of Fig. 1.10). Ions near the rear mirror will feel the changing electric field and consequently their energy (and TOF) will be artificially modified. The effective mass bandwidth has been confirmed via offline experiments to be about 60% of the upper limit in the case of $A/q \sim 40$ ions [61].

MRTOF

MRTOF devices have been developed at several facilities throughout the world, *e.g.* CERN, GSI, and RIKEN, as isobar separators and mass spectrographs. Here they and their recent activities will be introduced and explained briefly in the following parts.

I) MRTOF@ISOLDE/CERN

A Penning trap system named ISOLTRAP has been developed for accurate and precision mass measurements for short-lived nuclei at ISOLDE/CERN. ISOLDE facility can provide

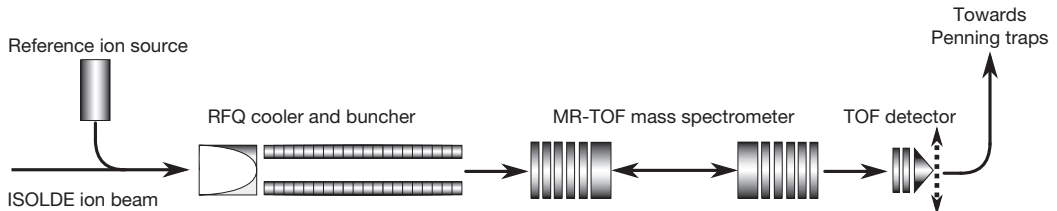


Figure 1.11: Schematic view of the MRTOF-MS at ISOLDE/CERN. This figure is taken from [62].

a large variety of stable and unstable isotopes. The major difficulty to perform efficient experiment at ISOLTRAP is selection of the one ion of interests from the unseparated isobaric contaminants. The mass resolving power of $R_m \sim 10^6$ is required to suppress the isobaric contaminants. At ISOLDE, an MRTOF has been developed as an isobar separator to solve this difficulty. Overview of ISOLTRAP system and the MRTOF are shown in Fig 1.11. MRTOF is located after the RFQ cooler and buncher system with Bradbury-Nielsen gate (BNG, for its details see Section 1.4.3).

In the case of the MRTOF at ISOLDE, the in-trap potential lift technique has been adopted. This is not suitable for wide mass bandwidth measurement, but is convenient for in-flight separation, which was discussed previously.

The MRTOF at ISOLDE has also been used for online mass measurements of neutron-rich calcium isotopes, $^{53,54}\text{Ca}$ [62], and potassium isotopes, $^{52,53}\text{K}$ [63], which are produced by proton-induced fission reactions of a uranium carbide target by 1.4 GeV protons. The mass resolving power of the MRTOF at ISOLDE has been shown to achieve $R_m \approx 2 \times 10^5$ at maximum [64]. Their mass values were determined by employing two reference nuclei. The relative precision of their mass values are distributed in the range of $\delta m/m = 6.8 \times 10^{-7}$ to 2.2×10^{-6} .

II) MRTOF@FAIR/GSI

At GSI, the MRTOF [65] has been developed as both a mass spectrometer and isobar separator for the Low-Energy Branch of the Super-FRS [67], which uses a superconducting magnetic for separation of exotic nuclear beams made via projectile fragmentation and fission of ^{238}U beams at about 1 GeV/nucleon. Figure 1.12 shows the schematic view of the MRTOF system at FAIR/GSI.

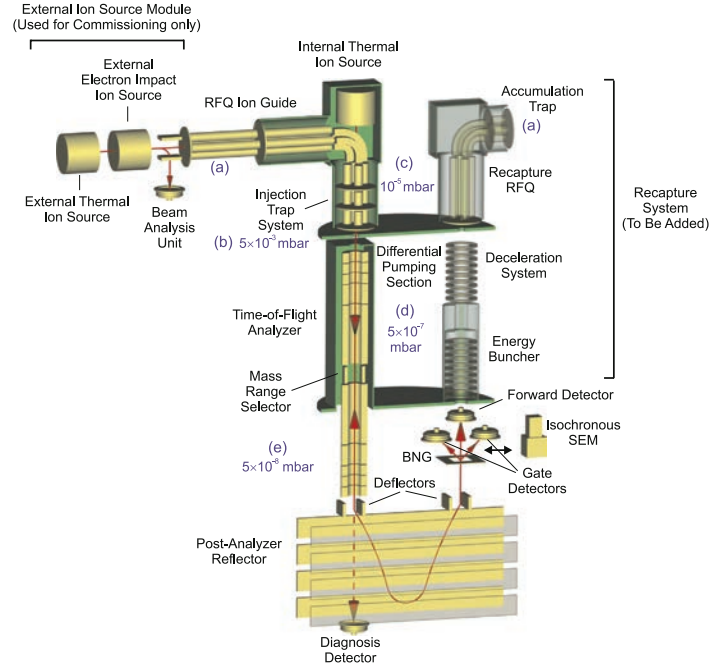


Figure 1.12: Schematic view of the MRTOF-MS at FAIR/GSI. This figure is taken from [65].

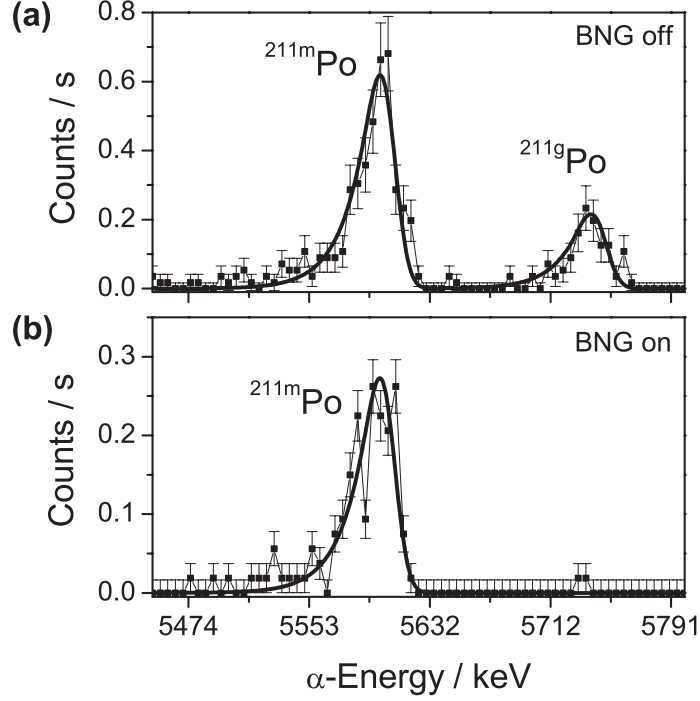


Figure 1.13: Spatial separation of $^{211g,211m}\text{Po}$ by use of the BNG in the MRTOF-MS. Energy spectra of the main alpha decay branches are shown, which were measured with the Si detector behind the gate with the voltages on the BNG off (a) and with the voltages on the BNG pulsed for transmission of the isomeric state only (b). This figure is taken from [66].

The MRTOF at GSI has a triple injection trap system, which enables the ion cooling and ejection process to require less than few milliseconds with about 100% duty cycle. A post-analyzer reflector is installed at the exit of the MRTOF at GSI, which is to image a final time focus at isochronous SEM and BNG (see Fig 1.12). The mass resolving power of $R_m = 6 \times 10^5$ has been achieved in offline measurement of $^{133}\text{Cs}^+$ ions.

The mass measurements via MRTOF-MS have been performed for heavy, α -emitting nuclei around neutron magic number $N = 126$, ^{211}Po , ^{211}Rn , and ^{213}Rn [68]. In the case of ^{211}Po , both the ground state and isomeric state were observed and were resolved in the mass spectrum of the MRTOF-MS [66]. The excitation energy of the isomeric state has been determined for the first time via the MRTOF-MS and the result of $E_X = 1472(120)$ keV is in good agreement with the literature value of $E_X = 1462(5)$ keV. The mass separation by the MRTOF-MS combining with the BNG has been performed successfully to $^{211g,211m}\text{Po}$, as shown in Fig. 1.13.

III) MRTOF@RIKEN

In RIKEN Nishina Center for Accelerator-Based Science, the MRTOF [70] will be coupled with several apparatuses, *e.g.*, an in-flight RI beam separator BigRIPS [71], a gas filled recoil separator GARIS-II [72], and KEK isotope separation system KISS [73]. This will allow the measurement of the masses of key nuclei of rapid neutron-capture process and superheavy elements. Connection between each apparatus to the MRTOF will be done by

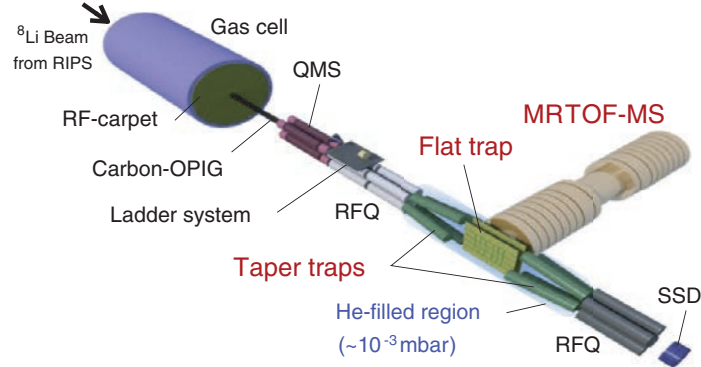


Figure 1.14: Schematic view of the MRTOF-MS at RIKEN in the initial commissioning. A section of RFQ between the QMS and the taper trap was mounted on a ladder system along with a channeltron electron multiplier, which can be used as a beam intensity monitor, and an alkali ion source for offline test. An SSD detector was used as the α -decay detector of ^8Li for beam line tuning. This figure is taken from [69].

using various gas-cell systems, such as the SLOWRI and the PALIS gas-cells for BigRIPS [74, 75].

Initial commissioning of the MRTOF at RIKEN was performed with ions of the short-lived isotope ^8Li [69]. Figure 1.14 shows the experimental setup of this commissioning. ^8Li ions were produced by fragmentation reaction of 100 MeV/nucleon ^{13}C beam and were selected by the RIPS projectile fragment separator [76]. ^8Li ions were stopped in the gas-cell and were extracted as extremely low-energy ions. The mass of ^8Li was determined using the single reference method (see Section 3.1) employing ^{12}C as a mass reference, and was determined with relative precision of $\delta m/m = 6.6 \times 10^{-7}$.

At RIKEN, the MRTOF has recently been applied for mass measurements of short-lived heavy nuclei, $^{204-206}\text{Fr}$, $^{204,205}\text{Rn}$, and $^{204,205}\text{At}$, which are produced by fusion evaporation reactions [77]. For this experiment, the SHE-mass facility was utilized (see Section 1.4.1). In this study three A/q series, $A/q = 204 - 206$, were observed. Among them, identifications of ^{205}Bi , $^{204,205}\text{Po}$, ^{206}Rn , and ^{206}At were done with less than 10 events in TOF spectra, verifying that the MRTOF-MS is an efficient way to identify exceedingly low-yield species like superheavy elements.

Stabilities in the MRTOF system were studied for stable long-time operation [70]. TOF values may vary due to instability of high-voltage power supplies for mirror electrodes and thermal expansion of MRTOF device itself. Variation in the high-voltages is limited to the level of $\Delta V/V = 5$ ppm by an active PID compensation loop, and it allows the mass resolving power of $R_m = 1.4 \times 10^5$. Influence of the thermal expansion was also measured and results are shown in Fig 1.15. In order to guarantee the accuracies of the measurements with MRTOF-MS, the system is designed to enable rapid drift compensation (see Section 1.4.3 and 3.1).

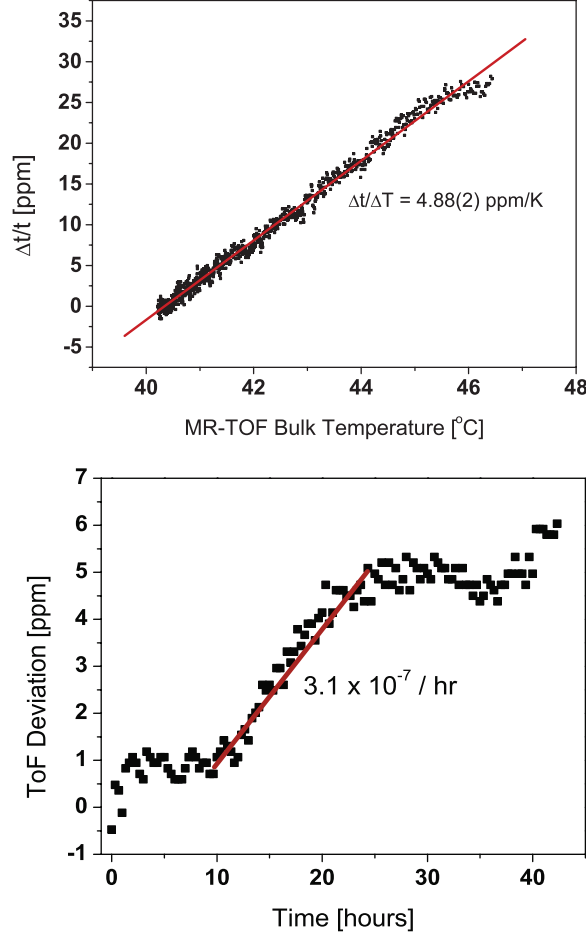


Figure 1.15: (Top) Measured effect of thermal expansion on the TOF. (Bottom) Long-term stability of the MRTOF-MS. The fast component is consistent with thermal expansion from a 0.8 K increase in the temperature of the MRTOF. This figure is taken from [70].

1.4 Experimental apparatuses

The half-lives of the interested nuclei indicated in Fig. 1.1 are distributed in the range of about 10 sec to 10^{-2} sec. Due to their half-lives and required mass precision for X-ray burst calculation, multireflection time-of-flight mass spectroscopy (MRTOF-MS) is the only method, among the mass measurement techniques widely used as discussed in previous part, which satisfies these requirements.

It is envisioned that several MRTOF devices will be installed at various facilities within RIKEN Nishina Center. At present, however, there is only one available MRTOF device which is combined with a gas-filled recoil ion separator GARIS-II via a gas-cell and an ion transport system, called SHE-mass facility. The details of SHE-mass facility and apparatuses configuring it, both GARIS-II and MRTOF, are given in this section.

1.4.1 SHE-mass facility

The SHE-mass facility at the RIKEN Nishina Center for Accelerator Based Science has been developed to measure the masses of superheavy elements (SHE). The facility consists of a multi-reflection time-of-flight mass spectrograph (MRTOF-MS) coupled with the gas-filled recoil ion separator GARIS-II via a cryogenic gas-cell (CGC) and an ion transport system. A schematic view of the SHE-mass facility is shown in Fig. 1.16. Nuclei of interest produced by fusion-evaporation reactions are transmitted to the GARIS-II focal plane and then stopped in the CGC. Ions of the nuclei of interest are extracted from the CGC and then trapped in the first flat trap before being ejected orthogonally and transported to the second flat trap. Ions trapped in the second flat trap can be ejected and transferred into the MRTOF device to be mass analyzed. For our region of interest, mass measurements in the MRTOF-MS require flight times of ≈ 5 ms. Then total required measurement time, including transportation time to the MRTOF device, being $t_{\text{total}} \lesssim 30$ ms is compatible with the ($t_{1/2} \lesssim 100$ ms) lifetimes of the nuclei of interest in the present study. Overall efficiency of the SHE-mass facility, excluding the transport efficiency of GARIS-II, is estimated to be on the order of 1%.

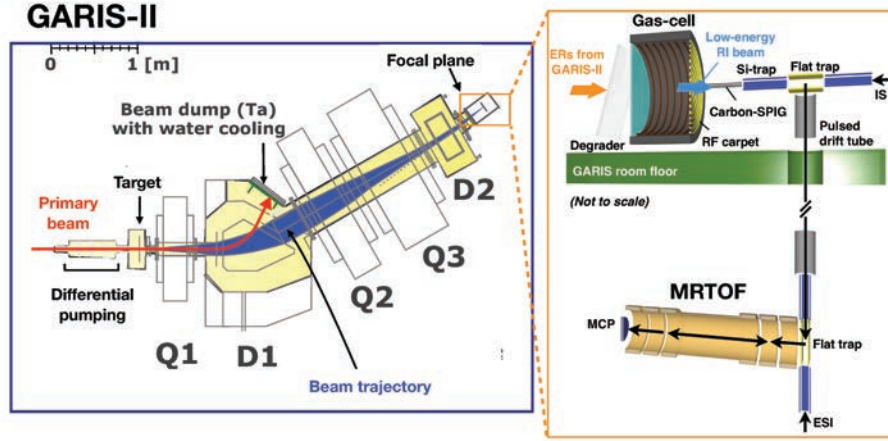


Figure 1.16: Schematic view of the SHE-mass facility. Facility consists of the gas-filled recoil separator GARIS-II, a helium-filled rf-carpet gas cell, a multi-reflection time-of-flight mass spectrograph (MRTOF) and a transport system from the gas cell to the MRTOF device. GARIS-II consists of five electromagnets – two dipoles (D1 and D2) and three quadrupoles (Q1, Q2, and Q3). The gas-cell system was installed in the GARIS-II focal plane and connected to the ion transport system. Extremely low-energy ions extracted from the gas-cell were transported to and accumulated in the first flat trap. Trapped ions were ejected orthogonally, then accelerated and decelerated via pulsed drift tubes for transport to the second flat trap. The transported ions were cooled and trapped in the second flat trap before being ejected and transferred into the MRTOF. Ions flew in the MRTOF for a pre-determined number of laps. Finally Ions were detected with a multi channel plate (MCP) detector and their times-of-flight recorded by means of a high-precision time-to-digital converter.

1.4.2 Gas-filled recoil separator GARIS-II

Ions moving in dilute gas may undergo charge exchange reactions with gas molecules. If the mean free path of such charge exchanging reactions is sufficiently short, the charge state will come into equilibrium and ion charge states can be represented by the mean charge state. The mean charge state \bar{q} is given as an empirical function of ion velocity v and atomic number of ion Z thusly:

$$\bar{q} \approx C (v/v_0) Z^{1/3}, \quad (1.28)$$

where C and v_0 are a constant and the Bohr velocity, respectively. The magnetic rigidity of ions in dilute gas depends solely on the ion's atomic number Z and mass number A and is related to the ion's mean charge state \bar{q} :

$$B\rho = \frac{M_{\text{ion}}v}{\bar{q}} \approx \frac{0.0227}{C} \frac{A}{Z^{1/3}} \text{ (Tm)}. \quad (1.29)$$

This equation indicates charge exchange reactions with dilute gas could cancel out ion velocity dispersion. Thus we can selectively transport ions having a large velocity distribution, such as is typical of fusion-evaporation products, without changing of magnetic field settings when the irradiating beam energy is changed. Devices employing this principle of charge state equilibration via beam interactions with dilute gas are referred to as gas-filled separators.

The mass resolving power, $A/\Delta A$, for a gas-filled separator is proportional to the $B\rho$ resolution, $\Delta B\rho/B\rho$. The width of the ion distribution, $\Delta B\rho$, is determined mainly by a balance of two processes: the charge exchanging reactions and multiple Coulomb scattering with gas molecules, and can be written as

$$\left(\frac{\Delta B\rho}{B\rho} \right)^2 = \Delta_q^2 + \Delta_s^2, \quad (1.30)$$

where Δ_q and Δ_s are the relative variance of charge exchange and scattering, respectively. Both processes depend mainly on the pressure of the dilute filling gas, but their effect on $B\rho$ resolution are in opposition to each other. The relative variance from originating multiple Coulomb scattering, Δ_s , is proportional to gas pressure, since increased numbers of gas molecules lead to ever more collisions with gas molecules, which in turn leads to a larger momentum distribution for the ions. At the same time, the increasing number of collisions leads to more charge exchange reactions and a small charge state dispersion will be achieved due to the charge states of all most of the ions reaching the mean charge state. Therefore, an optimum gas pressure, P_{opt} , which achieves a minimum value of $\Delta B\rho/B\rho$, must be exist (see Fig 1.17). To enable efficient experiments with gas-filled separators, P_{opt} is an important operation parameter.

The gas-filled recoil separator GARIS-II is an apparatus specialized to collect and transport fusion-evaporation residues, and has been used for (super-)heavy element nucleosyntheses and nuclear chemistry experiments at RIKEN.

Schematic view of GARIS-II is shown in Fig 1.16 within the blue-colored frame. GARIS-II consists of five electromagnets in a $Q_v D Q_h Q_v D$ configuration. The bending angle of the first dipole magnet (D1) is 30° . Most of the all light, unwanted particles such as primary beam nuclei (indicated with a red arrow in Fig 1.16) can be separated in the first dipole due to their magnetic rigidities being sufficiently small as compared to the (super-) heavy

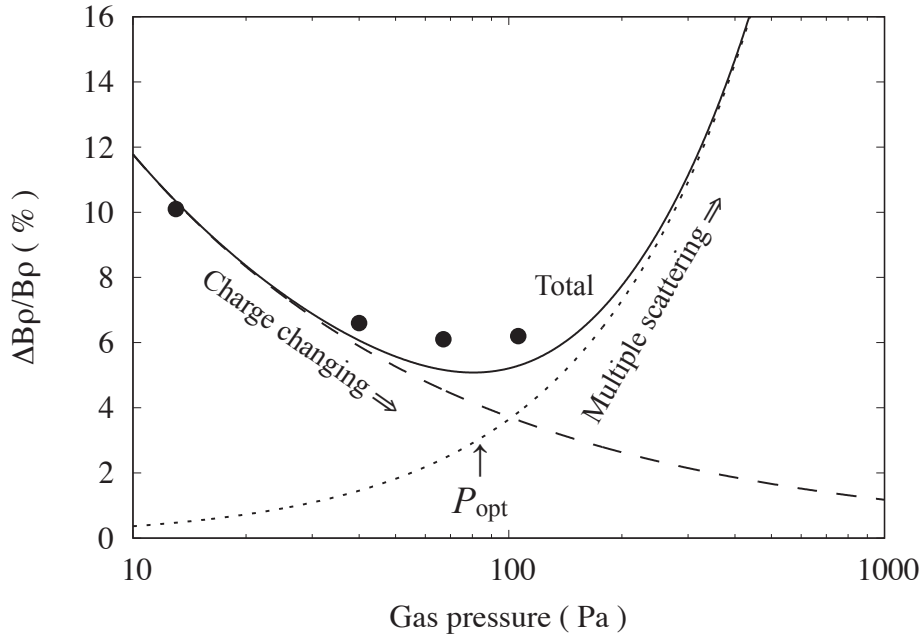


Figure 1.17: Gas pressure dependence of the $B\rho$ -resolution. The dotted and dashed lines indicate the contributions originating from charge state dispersion [78] and multiple Coulomb scattering [79], respectively. Resultant $B\rho$ -resolution ($\Delta B\rho/B\rho$) is shown by the solid line. Filled circles indicate experimental data for ^{208}Pb , taken from [80].

nuclei (indicated by the blue band in Fig 1.16) produced in the fusion-evaporation reactions. The first quadrupole magnet (Q1) provides a large angular acceptance to GARIS-II while the second dipole magnet (D2) suppresses the unwanted light particles originating from background events at the focal plane.

1.4.3 Cryogenic gas-cell and Ion transport system

The fusion-evaporation products delivered by GARIS-II are far too high-energy to be directly transferred into the MRTOF-MS. To accomplish this feat, the MRTOF-MS is connected to GARIS-II via a cryogenic gas-cell and ion transport system as shown in Fig. 1.16 within the orange-colored frame. The gas cell stops and thermalizes the energetic ions delivered by GARIS-II. Ions can then be efficiently extracted from the gas cell and transferred to an RF ion trap to accumulate and cool before being sent to the MRTOF-MS.

Theory of ion trapping with radio-frequency electric field

The equation of motion of a singly charged ion in the electric potential $\Phi(t, \vec{r})$ can be represented by

$$m \frac{d^2 \vec{r}}{dt^2} + \frac{e}{\mu} \frac{d\vec{r}}{dt} = -e \nabla \Phi(t, \vec{r}), \quad (1.31)$$

where $\mu = \mu_0 P_0 / P$ is the mobility of the ion, P_0 is the atmospheric pressure, μ_0 is the ion mobility at a pressure of P_0 . By assuming that $\Phi(t, \vec{r})$ can be decomposed to be time and

position dependent terms, $\Phi(t, \vec{r}) = \phi(t)\varphi(\vec{r})$, time-dependent quadrupole potential can be asymptotically expressed as

$$\Phi(t, \vec{r}) = \phi(t)\varphi(\vec{r}) = (U - V \cos \Omega t) \times \frac{x^2 - y^2}{2r_0^2}. \quad (1.32)$$

Then by substituting Eq. 1.32 for Eq. 1.31, the ion motion in the time-dependent quadrupole potential is written as follow,

$$\left(\frac{d^2}{dt^2} + \frac{1}{\tau_v} \frac{d}{dt} \right) \begin{pmatrix} x \\ y \\ z \end{pmatrix} + \frac{e}{mr_0^2} (U - V \cos \Omega t) \begin{pmatrix} x \\ -y \\ 0 \end{pmatrix} = 0, \quad (1.33)$$

where $\tau_v \equiv \mu m/e$. If we introduce the expressions as follow

$$\tau = \Omega t, \quad p = \frac{1}{2\tau_v \Omega}, \quad a_x = -a_y = \frac{eU}{mr_0^2 \Omega^2} \quad q_x = -q_y = \frac{eV}{mr_0^2 \Omega^2}, \quad (1.34)$$

Eq. 1.33 becomes to be

$$\left(\frac{d^2}{d\tau^2} + 2p \frac{d}{d\tau} + a_i - q_i \cos \tau \right) r_i = 0 \quad (1.35)$$

where r_i corresponds to x and y . If one assume the solution can be given as a product of damping term, $r_i = u_i(\tau) \exp(-p\tau)$, a form of that equation can be changed to the Mathieu Equation type,

$$\left(\frac{d^2}{d\tau^2} + a'_i - q_i \cos \tau \right) u_i = 0. \quad (1.36)$$

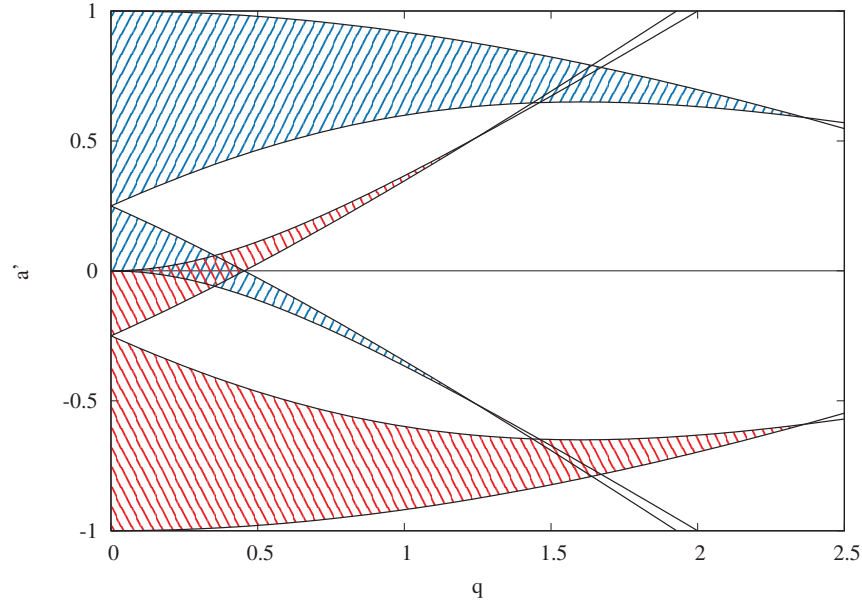


Figure 1.18: Strutt diagram. Each hatched zone indicates the stable region for one dimension. Overlapped areas of red- and blue-colored stripes indicate regions satisfying the stable conditions along both axes simultaneously.

where $a'_i = a_i - p^2$. It is well-known that solutions of the Mathieu equations are stable only for certain regions of the $a' - q$ plane known as the Strutt diagram, which is shown in Fig. 1.18.

Here we consider a situation where there is only an inhomogeneous radio-frequency (RF) electric field. The motion of the ion in such an RF field can be expressed as a sum of the secular motion $\langle \vec{r} \rangle$ and the micro-motion \vec{R} as follows:

$$\vec{r} = \langle \vec{r} \rangle + \vec{R}(t) = \langle \vec{r} \rangle + C \vec{E}_{\text{eff}} \cos(\Omega t + \theta), \quad (1.37)$$

where $\langle \vec{r} \rangle$ is assumed to be nearly constant over a period of the RF oscillation of frequency Ω . By assuming Eq. 1.31 has a solution represented by Eq. 1.37, one can calculate

$$C = -\frac{e}{m\Omega^2} \frac{1}{\sqrt{1 + 1/\Omega^2 \tau_v^2}}, \quad \tan \theta = \frac{1}{\Omega \tau_v}. \quad (1.38)$$

Then the time-averaged force $\langle \vec{F} \rangle$ produced by the RF electric field is represented by

$$\begin{aligned} \langle \vec{F} \rangle &= e \langle \vec{E}_{\text{eff}} \cos \Omega t + (\nabla \cdot \vec{E}_{\text{eff}} \cos \Omega t)|_{\vec{r}=\langle \vec{r} \rangle} \vec{R}(t) \rangle_{\text{time average}} \\ &= -\nabla(\vec{E}_{\text{eff}} \vec{E}_{\text{eff}}) \frac{e^2}{4m\Omega^2(1 + 1/\Omega^2 \tau_v^2)}. \end{aligned} \quad (1.39)$$

In the limits of vacuum and high-pressure, the time-averaged force becomes

$$\langle \vec{F} \rangle = -\nabla(\vec{E}_{\text{eff}} \vec{E}_{\text{eff}}) \frac{e^2}{4m\Omega^2} \frac{1}{\Omega^2} \quad \text{for } \Omega \tau_v \gg 1 \text{ (vacuum)} \quad (1.40)$$

$$\langle \vec{F} \rangle = -\nabla(\vec{E}_{\text{eff}} \vec{E}_{\text{eff}}) \frac{e^2}{4m\Omega^2} \tau_v^2 \quad \text{for } \Omega \tau_v \ll 1 \text{ (high - pressure)}. \quad (1.41)$$

Such treatment describing the “averaged” motion of the ion in an RF electric field is known as the pseudo-potential approach. The pseudo-potential is very useful for prediction of the motion of ions in RF electric fields.

Cryogenic gas-cell

Reaction products enter the CGC after being transmitted through GARIS-II. The CGC is typically pressurized with 100 mbar helium. Incoming ions will undergo ionizing collisions with the helium gas, eventually stopping in the CGC. Inside the CGC is a cylindrical printed circuit board with ≈ 50 electrodes to produce a uniform static electric field that can push ions to the end of the chamber where a RF carpet is located for extracting the ions from the CGC. Figure 1.19 indicates a conceptual view of the RF carpet. The RF carpet consists of ring-shaped electrodes to which oscillatory signals are applied. The signals are superpositions of RF and audio frequency (AF) signals. There are 4 signals which have different AF and RF phase combinations. Ions arriving at the RF carpet will be trapped between the RF pseudo-potential and a pushing electric field. This trapping process is assisted by energy damping collisions of the ions with the helium atoms. The four phases of the AF signals produce a traveling wave “surfing potential”, which can transport ions radially along the carpet – either toward or away from the center of the RF carpet, depending on the choice of relative AF phases. The RF carpet has a nearly 100% efficiency at buffer gas pressures up to 100 mbar or more. Overall efficiency of the CGC, including stopping, was measured with Fr isotopes to be 30% [81].

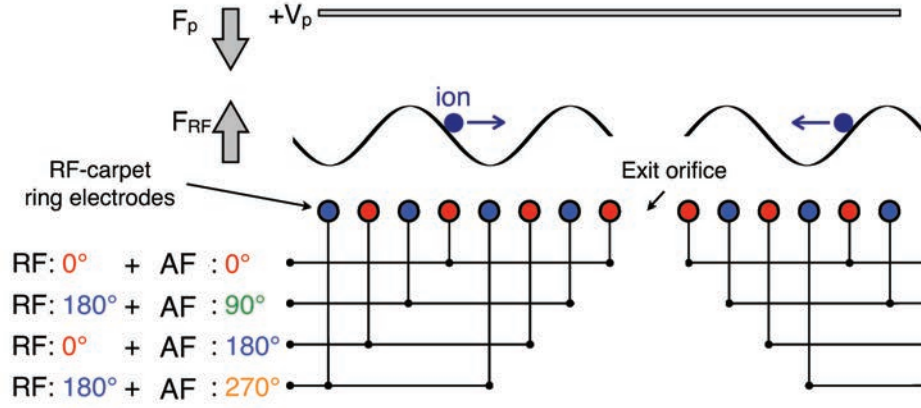


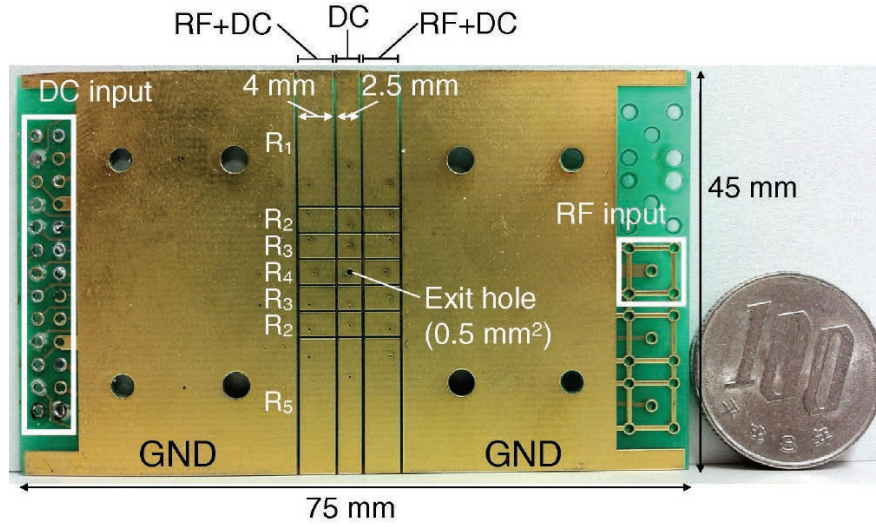
Figure 1.19: Conceptual view of ion surfing method used by the RF carpet. F_{RF} and F_p are a repelling force from the RF carpet and a pushing force, respectively.

Flat trap

Two suites of three RF ion traps are used in the facility. The first is used to accumulate ions from the gas cell, while the second is used to prepare ions prior to transfer to the MRTOF-MS. Each suite of traps consists of a “flat ion trap” sandwiched between a pair of linear Paul traps made from resistive silicon. Ions initially accumulate and are precooled in the linear Paul trap, then are transferred to the flat ion trap. The flat trap consists of a pair of mirrored printed circuit boards. A photograph of one such circuit board is shown in Fig 1.20. They are set parallel and facing each other. By applying an electric potential between the central strip of electrodes and the outer strips of electrodes, an approximate quadrupole field is formed. Modulating the potential difference to form an RF signal produces a pseudo-potential field in which ions can be radially confined. By use of properly applied DC biasing of each segment, an axial potential well can be formed to provide axial confinement.

Each suite of ion traps is pressurized to $\sim 10^{-3}$ mbar of helium gas. Scattering collisions with the gas provide cooling of the trapped ions. The capacity of the flat traps is $\sim 10^4$ ions[82].

The first flat trap is used for ion transport to the experimental room, downstairs from GARIS-II, where the MRTOF-MS is located, and a second ion trap suite, identical to the first, is employed as the injector for the MRTOF-MS. Ions extracted from the CGC will be transported to the first ion trap suite after passing through a sextupole ion guide (SPIG). To eject ions from the flat trap, a synchronized pair of switches is employed to apply a positive (negative) voltage to the central electrode (the one with the exit hole in Fig.1.20) of the “top” (“bottom”) circuit board. This produces a dipole electric field that accelerates the ions toward the bottom circuit board and the ions leave the trap orthogonally via the small exit hole in the central electrode. This novel geometry allows the flat ion trap to accept ions from both sides, greatly simplifying the use of reference ions. This property of the flat trap allows for compensation of TOF drift originating from some instabilities discussed in Section 1.3.4. Figure 1.21 shows a concept of this drift compensation. By measuring the interesting radioactive ions and the reference ions sequentially, we can measure the drift of TOF via TOF value of the reference ions and can correct the TOF values of the interesting ions (see Section 3.1).



Electrode	R_1	R_2	R_3	R_4	R_5
Length (mm)	14.9	2.6	2.6	2.6	14.9
DC voltage (V) : Accumulation*	-4.5	-5.7	-5.8	-6.0	5.0
DC voltage (V) : Cooling	27	10.5	7.5	5.0	27

* R_1 side is the entrance in this case.

Figure 1.20: Photograph of the flat trap with typical direct current (DC) voltages annotated. Spacing between adjacent electrodes is 0.3 mm. A ¥100 JPY coin is included for scale. This figure is taken from [82].

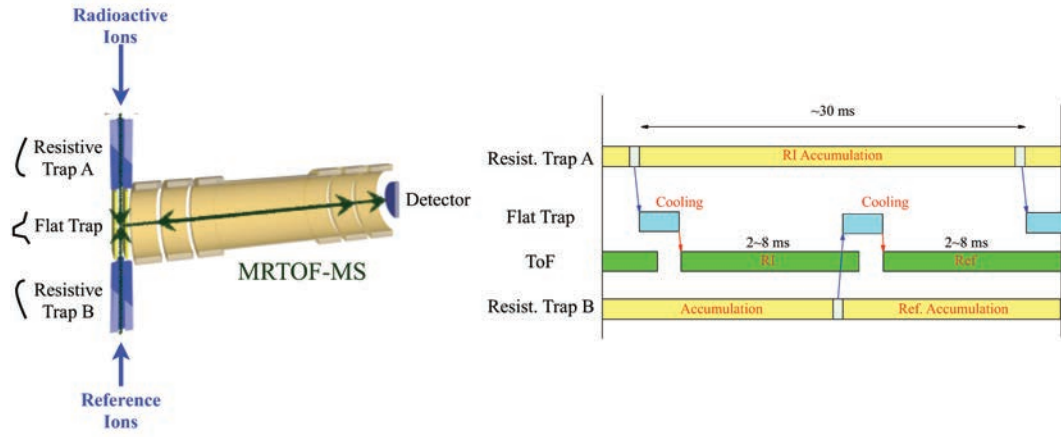


Figure 1.21: Conceptual view of time-of-flight drift compensation. (Right panel) Ejection system consisting of the flat trap and two resistive tarps can accepts the ions come from both sides of upper (interested radioactive ions) and bottom (offline reference ions). (Left panel) Time sequence of the measurement with reference ions. In this method, we can measure the TOF value of interested ions and can compensate for TOF drift without any loss of interested ions.

Drift tube and Bradbury-Nielsen gate

Two drift tubes and a Bradbury-Nielsen gate (BNG) are installed between the first and the second flat traps. The first drift tube, installed upstairs, was used for acceleration of the ejected ions from the first flat trap while the second, installed downstairs, decelerated the ions to allow trapping them in the second flat trap. The drift tubes accelerate/decelerate the ions by application of high voltage pulses when ions are passing through the drift tubes. An overview of this acceleration/deceleration mechanism is shown in Fig. 1.22.

The BNG is made by thin wires and is employed as a mass filter. When undesirable ions are passing through the BNG, it can deflect them by applying opposing voltages to adjacent thin wires (Fig. 1.23). In this way, only desirable ions could be allowed to enter the second flat trap. The maximum mass resolving power of the BNG was $m/\Delta m \sim 100$.

Transport efficiency between the first and the second trap was evaluated to be $\sim 3\%$.

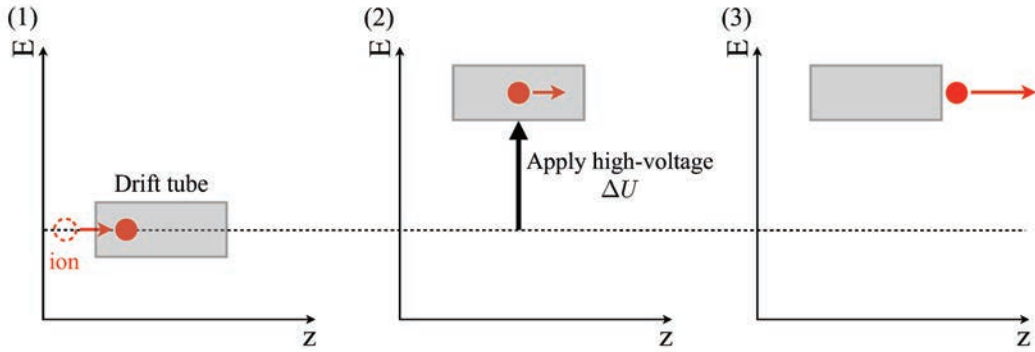


Figure 1.22: Conceptual view of drift tube. (1) An ion (red circles) ejected from the first trap goes into a drift tube at zero-potential, as indicated by the dotted line. (2) While the ion is passing through the drift tube, a fast high-voltage switch increases the potential applied to the drift tube by ΔU . The ion in the drift tube does not “feel” the change of potential energy. (3) The ion exits the drift tube and accelerates by ΔU . The deceleration process is performed in much the same way, but the change in potential is $-\Delta U$.

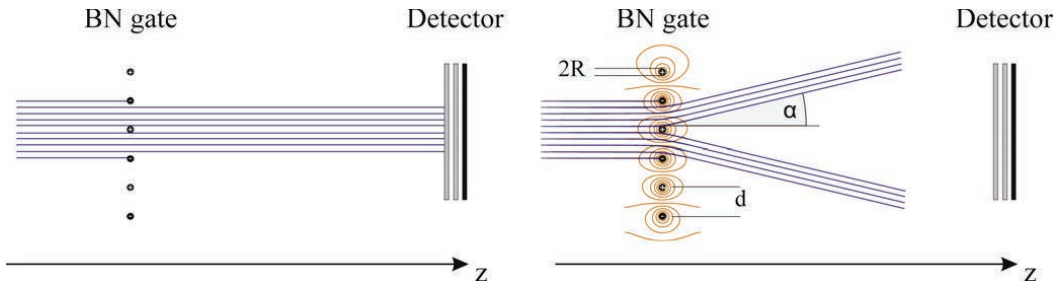


Figure 1.23: Schematic of the working principle of a Bradbury-Nielsen gate showing idealized ion trajectories. If both wire sets are at the same potential, most of the ions cross the gate and reach the detector (left). If opposing voltages are applied to the wires, the beam is deflected, effectively turning off the gate (right). Also shown are equipotential lines of the wires. This figure is taken from [83].

Chapter 2

EXPERIMENTS

2.1 Reaction systems

In order to access the proton-rich, $N < Z$ nuclei via fusion-evaporation reactions, combinations between $N = Z$ nuclei are preferred. There are existing results using these reactions to access $N = Z - 2$ nuclei, which are counter parts to calculate Q_{2p} -values of waiting point nuclei (see Fig 1.1): $^{40}\text{Ca}(^{28}\text{Si}, 2n)^{66}\text{Se}$ [29], $^{40}\text{Ca}(^{32}\text{S}, 2n)^{70}\text{Kr}$ [30], and $^{40}\text{Ca}(^{36}\text{Ar}, 2n)^{74}\text{Sr}$ [31]. There are no availabilities of ^{28}Si and ^{32}S beams in SHE-mass facility due to the ion source of accelerator being unable to provide these elements.

Thus, possibilities for substitute reactions having the same compound nuclei were considered. Candidates for the primary beam were ^{36}Ar and ^{40}Ca because both argon and calcium isotope beams are widely used for nucleosyntheses of (super)heavy elements and high intensity beams have previously been developed. Reaction systems used for producing the interesting nuclides of the present study with both ^{36}Ar and ^{40}Ca primary beams are tabulated in Table 2.1. In these reaction systems, non-enriched, natural materials can be

Table 2.1: List of reaction system used for producing interested nucleides in the present study. Interested nuclides are shown in first column and their half-lives and mass excess values are given in columns of the “ $t_{1/2}$ ” and the “ME”, respectively, where # indicates a value that has been extrapolated from systematic trends of AME16. The optimum exited energies are shown in the “ E_x ” column and corresponding production cross-sections are given in the column of “ σ ”.

	$t_{1/2}$ (msec)	ME (keV)	Reaction	E_x (MeV)	σ (μb)
^{61}Ga	167(3)	-47130(40)	$^{28}\text{Si}(^{36}\text{Ar}, 1\text{p}2\text{n})$	45.1	130
^{62}Ge	129(35)	-41740(140)#	$^{28}\text{Si}(^{36}\text{Ar}, 2\text{n})$	45.1	0.45
^{65}As	170(30)	-46940(80)	$^{32}\text{S}(^{36}\text{Ar}, 1\text{p}2\text{n})$	45.4	41
^{66}Se	33(12)	-41660(200)#	$^{32}\text{S}(^{36}\text{Ar}, 2\text{n})$	45.4	0.12
^{70}Kr	52(17)	-41100(200)#	$^{32}\text{S}(^{40}\text{Ca}, 2\text{n})$	45.6	0.16
^{74}Sr	27(8)	-40830(100)#	$^{40}\text{Ca}(^{36}\text{Ar}, 2\text{n})$	46.7	0.11

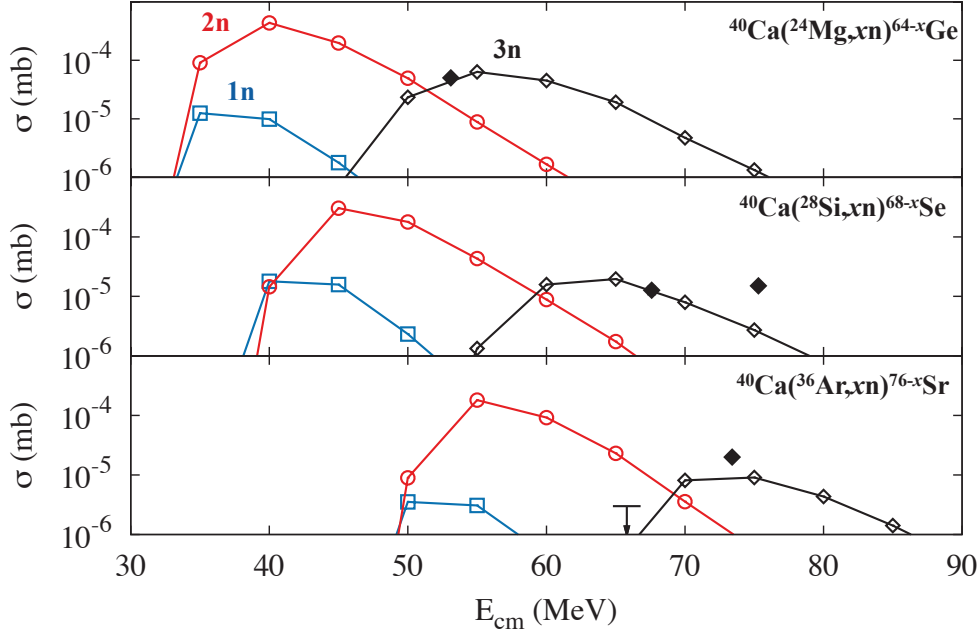


Figure 2.1: Comparison of theoretical and experimental production cross-sections. Open symbols and solid lines show the theoretical predictions and their color corresponds to neutron evaporation channels. Filled symbols and an arrow represent experimental values and an upper limit. Experimental data are taken from [85, 86, 87].

used for targets due to target nuclides having sufficient abundance; ^{28}Si 92.2%, ^{32}S 94.9%, and ^{40}Ca 96.9%. The predicted production cross-sections extend to very small values, ranging from $\sim 100 \mu\text{b}$ down to $\sim 10 \text{ nb}$. Therefore establishment of the experimental conditions which enable both efficient and stable experiments with an intense primary beams is necessary. In following sections, we will discuss the experimental conditions based on the uses of these reactions in the SHE-mass facility.

In order to estimate production cross-sections, LisFus [84] has been employed. The LisFus code relies on a model using an analytical approach and allows for calculating cross-sections of nuclei far from the stability, which may have very small values, without excessively time consuming computations. The LisFus code calculates the probabilities of 8 possible decay channels (n , $2n$, p , $2p$, d , t , ^3He , α) as well as the excitation energy distribution of daughter nuclei corresponding to each decay channels at a certain excitation energy, allowing for an excitation function for any given excitation energy to be calculated.

Validity of the LisFus model was confirmed by comparison with experimental values. The fusion evaporation reaction of $N = Z$ nuclei has been performed for β -delayed proton spectroscopy experiments of $N = Z - 3$ nuclei [85, 86, 87] and deduced production cross sections are indicated in Fig 2.1. The LisFus predictions reasonably reproduce the trends of the experimental results within one order of magnitude.

2.2 Primary beam separation

2.2.1 Difficulty in primary beam separation

Fusion-evaporation residues, due to their low velocities, behave like ions that have achieved an equilibrium mean charge state \bar{q} . For the present nuclides of interest, proton-rich Ge through Zr, the expected optimum $B\rho$ -values are distributed in the range of 0.7 to 0.8 Tm based on assuming $C = 0.641$ [88] in Eq 1.29. Primary beam particles, on the other hand, have long mean free paths in terms of charge exchange reactions, and do not reach an equilibrium state. Thus the $B\rho$ -values of primary beam particles are determined by a convolution of their charge state distribution after the target and their velocities. Figure 2.2 shows the predicted primary beam energy dependence of $B\rho$ -value. The charge state distribution was taken from Ref [89] based on a primary beam of ^{36}Ar . Expected primary beam energy after the target is less than 3 MeV/u, indicating that a relative fraction of primary beam ranging from 10^{-6} to 10^{-4} could reach the GARIS-II focal plane.

The transmission probability of primary beams in GARIS-II was also evaluated by a simulation based on Geant4 [90], which included consideration of charge exchange processes between the filled-gas and the ions, Coulomb scattering by the filled-gas, and the GARIS-II geometry and optics. An example of the simulation results for $^{28}\text{Si}(^{36}\text{Ar}, 2n)^{62}\text{Ge}$ reaction is shown in Fig. 2.3. The transmission probability for the ^{36}Ar beam was evaluated to be 2×10^{-5} under the $B\rho = 0.70$ Tm setting of GARIS-II, optimized for ^{62}Ge . If one were to use an intense primary beam of 5 pμA, the rate of the primary beam reaching the GARIS-II focal plane could be as much as 6×10^8 particles per second. Such an intense primary beam could lead to breakage of the thin Mylar window foils located at both the exit of GARIS-II and the gas-cell entrance. In addition, the gas-cell extraction efficiency depends on the incoming particle rate, decreasing due to space charge effects [91] as the incoming rate increases. The intensity of the all evaporation residues produced can be estimated to be $\approx 1 \times 10^7$ particle per second for 0.4 mg/cm² $^{\text{nat}}\text{Si}$ target with the presupposed 5 pμA beam of ^{36}Ar . Primary beam intensity at the GARIS-II focal plane is thereby roughly one hundred times higher than the evaporation residue ions. In order to ensure incoming primary beam does not deleteriously influence the gas-cell extraction efficiency, the relative intensity of primary beam compared to the evaporation residues must be reduced by more than a factor of one hundred.

2.2.2 Design of the primary beam stoppers

To enable performing experiments in the presence of intense contaminants, we installed a suite of new equipment for primary beam suppression in GARIS-II. The goal was for this equipment to improve the signal-to-noise ratio at the GARIS-II focal plane by at least a factor of one hundred.

The primary beam and the evaporation residues differ in terms of their behavior in GARIS-II based on their $B\rho$ -values and angular distributions immediately after the target. Their $B\rho$ -values are generally similar to each other, as discussed above, although there remains a capability to separate them by the small differences of their trajectories at the exit of the first GARIS-II dipole (D1) chamber, which can be seen in Fig 2.3. Evaporation residues have large angular distributions compared to the primary beam, due mainly to multiple scattering in the target materials and recoils of evaporated light-particles in de-excitation processes. Figure 2.4 shows the predicted position distributions at the entrance

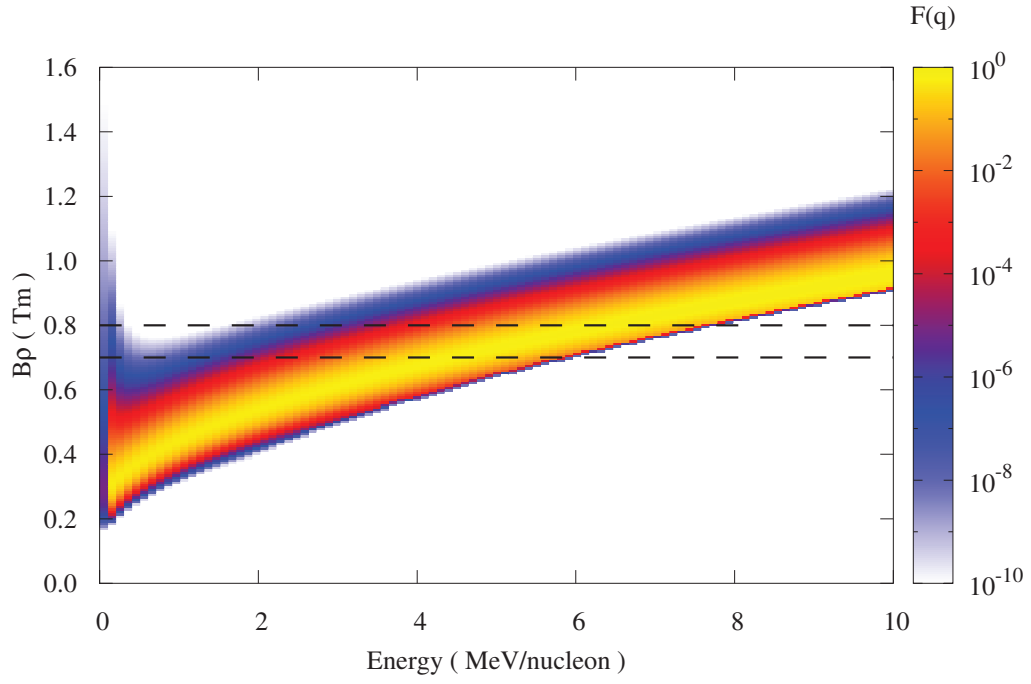


Figure 2.2: Predicted $B\rho$ -values of primary beam based on ^{36}Ar primary beam nuclide. Contour indicates the charge state fraction $F(q)$. Dashed lines represent the upper and lower $B\rho$ -value of nuclides of interest.

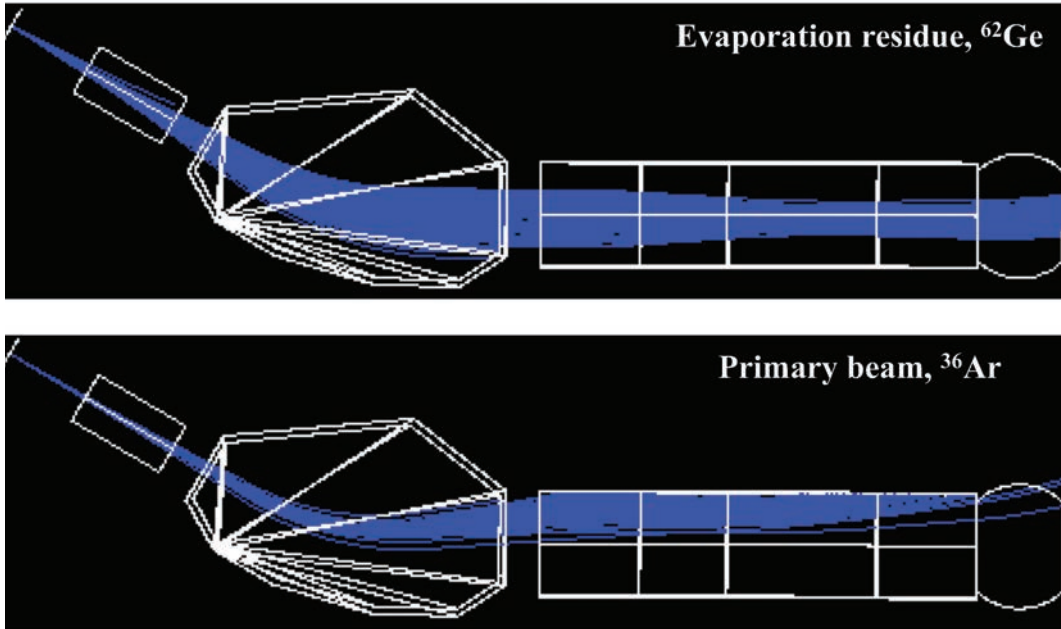


Figure 2.3: Ion trajectories in GARIS-II. Upper and lower panels show trajectories of ^{62}Ge and ^{36}Ar , respectively. Beam direction is from left to right. Magnetic rigidity of GARIS-II was $B\rho = 0.70 \text{ Tm}$.

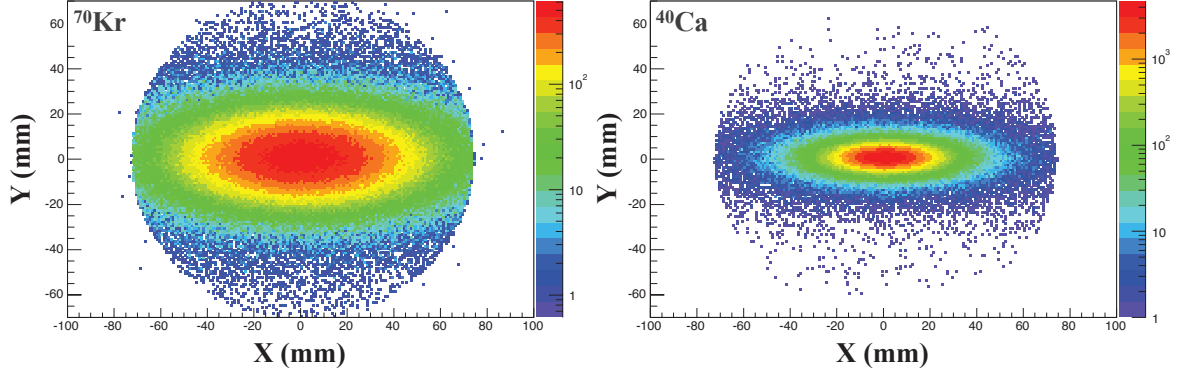


Figure 2.4: Simulated position distribution at GARIS-II D1 entrance based on $^{32}\text{S}(^{40}\text{Ca}, 2n)^{70}\text{Kr}$ reaction. Settings of GARIS-II were the same in both case. The circular edges in both panels reflect beam duct shape of GARIS-II.

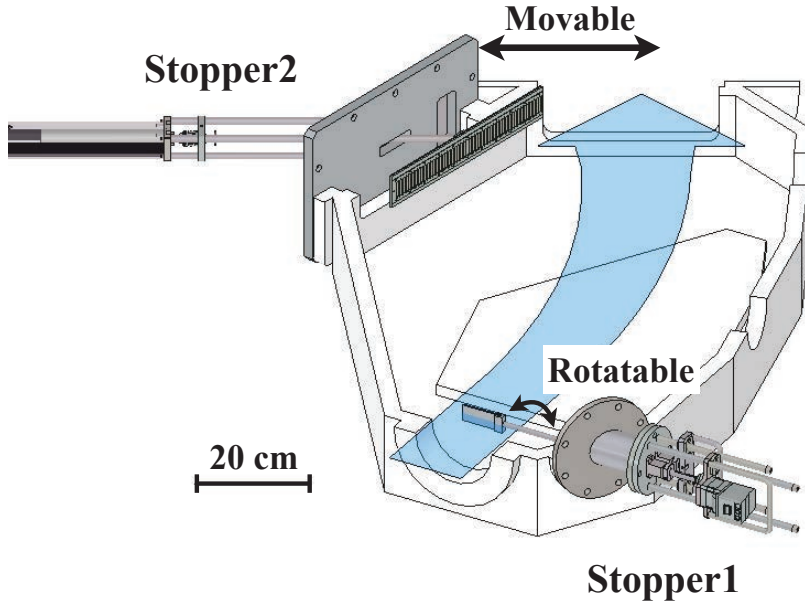


Figure 2.5: Schematic view of the primary beam stoppers. The D1 chamber is shown in cross-sectional view. The blue arrow indicates the beam direction.

of the GARIS-II D1 chamber, for both a ^{40}Ca primary beam and the evaporation residue ^{70}Kr . These distributions were evaluated by the same GARIS-II simulation as Fig 2.3. The angular distribution of ^{70}Kr is significantly wider than that of ^{40}Ca , showing that primary beam and evaporation residues could be separated by utilizing the differences in their angular distributions.

For separating the primary beams and the evaporation residues, two water-cooled primary beam stoppers, Stopper1 and Stopper2, were installed in the GARIS-II D1 chamber as indicated in Fig. 2.5. Stopper1, which could prevent most of the primary beam particles, was installed at the entrance of the D1 chamber and consisted of a copper plate of 80 mm width, 30 mm height, and 3 mm depth. Its effective area impinged by beam could be var-

ied by rotation. Stopper2, enhances the original GARIS-II beam dump to accept primary beams with more gently curved trajectories as compared with those typical for super-heavy element (high $B\rho$ -value) cases; it is located near the D1 chamber exit. Stopper2 was made by a 400 mm width, 60 mm height, and 5.5 mm depth copper board mounted on a linear manipulator to change the position. It additionally incorporated tantalum fins on its surface to prevent scattering of the colliding particles.

2.2.3 Performance evaluation of the primary beam stoppers

The performances of the both stoppers were evaluated by using the ^{208}Pb (^{18}O , $3n$) ^{223}Th reaction. A 6.5 MeV/u $^{18}\text{O}^{5+}$ beam with average intensity of 16 pnA was provided by the RIKEN linear accelerator RILAC. The segmented ^{208}Pb targets were prepared by evaporation on 60 $\mu\text{g}/\text{cm}^2$ carbon backings and their average thickness was 450 $\mu\text{g}/\text{cm}^2$.

An array of silicon detectors (HAMAMATSU S3204-09), which are arranged in 3×5 , was employed to count both the incoming ^{223}Th and the contaminants at the GARIS-II focal plane. Signals of the detector array were processed with both high- and low-gain circuits. The primary beam was chopped to measure the α -decay from ^{223}Th in low background conditions. Chopping sequence was set to be 0.2 sec beam on and 0.2 sec beam off. For counting the ^{223}Th events, high-gained data were used and the intensities were determined by fitting with gaussian. The intensities of the contaminants were calculated by integration of low-gained data down to about 15 MeV, which is a threshold of a data acquisition system for the low gain circuit.

In this reaction, the 4^+ ionization state of the ^{18}O beam after the targets has a close $B\rho$ -value to that which is optimal for ^{223}Th . Evaluated results are shown in Figs. 2.6 and 2.7. The intensity ratio of the contaminants to the ^{223}Th was determined to be ~ 20 without either stoppers. As the effective area of Stopper1 increased, the intensity of the contaminants rapidly decreased while the ^{223}Th counting rate reduced by a nominal fraction (Fig. 2.6). As a result, we could prevent $\sim 95\%$ of the contaminants from reaching the focal plane by using Stopper1, while $\sim 80\%$ of ^{223}Th were still transported. The same measurements were performed by changing the position of Stopper2 as shown in Fig. 2.7. When measuring the Stopper2 performance, the Stopper1 effective area was set to its maximum value of 2400 mm^2 . The Stopper2 measurement shows a similar result to that of Stopper1. Thus we can improve the signal-to-noise ratio by as much as ~ 200 times by using both stoppers.

This background reduction can be confirmed in the summed energy spectra of the silicon detector array which shown in Fig. 2.8. Background events are found in wide energy range and the primary beam components are clearly appeared in the situation of no beam stoppers and no primary beam chopping. After installing the both beam stoppers, the most of background events are disappeared without primary beam chopping.

2.3 Modification of the SHE-mass facility

A experimental setup of the present study was based on the SHE-mass facility. There were needs to modification of the detectors for tracing the β -decaying nuclides due to the SHE-mass facility is specialized for detecting superheavy (α -decaying) nuclides. One of the modifications was installing the beam stoppers above discussed, to be capable of employing the symmetric reaction system. Other one was replacements of Si detectors,

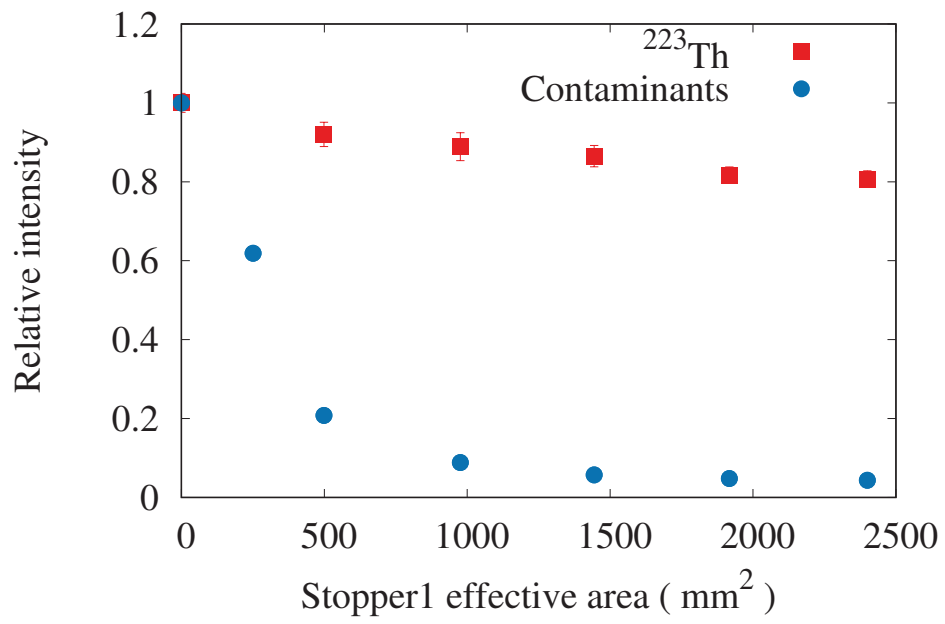


Figure 2.6: Result of the Stopper1 performance evaluations.

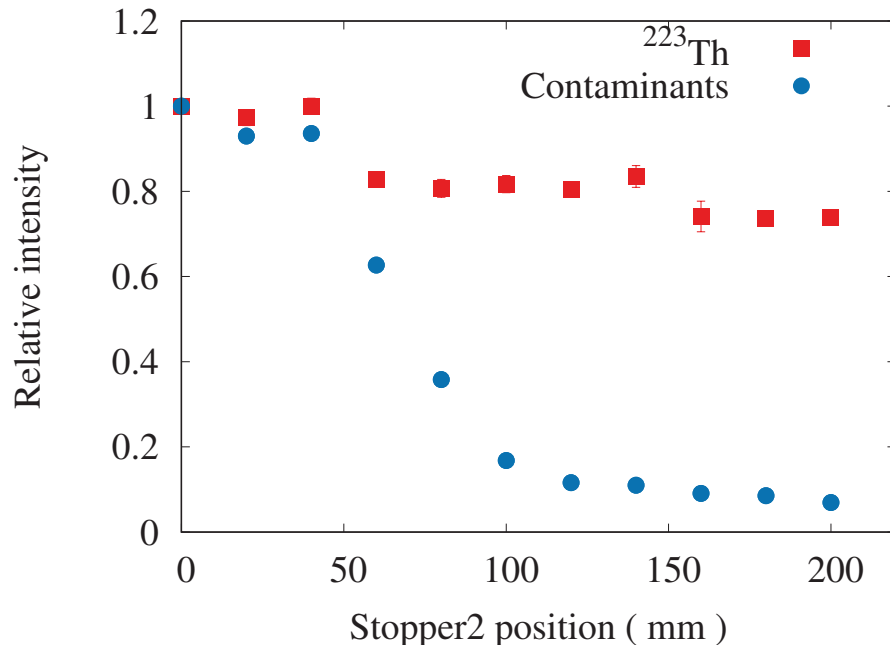


Figure 2.7: Result of the Stopper2 performance evaluations.

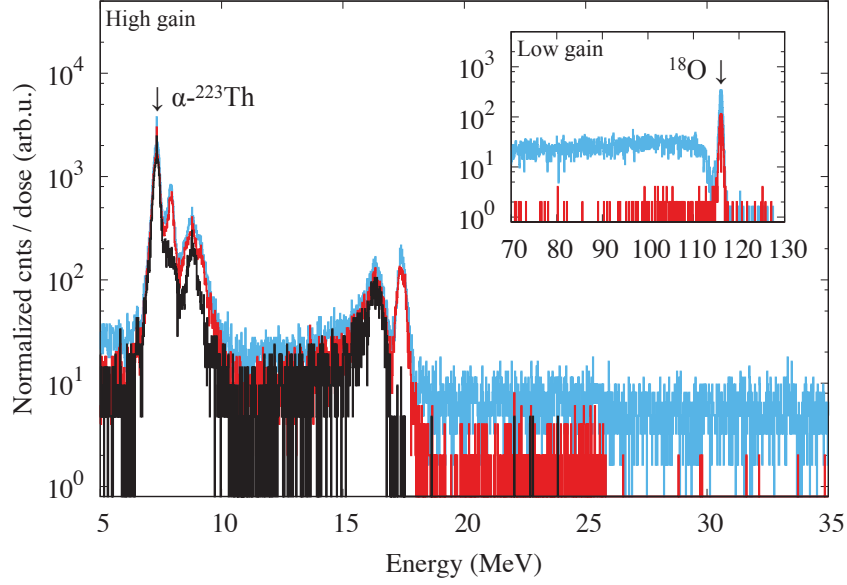


Figure 2.8: Summed energy spectra of the silicon detector array. (Blue line) Energy spectrum without both stoppers and primary beam chopping. (Black line) Energy spectrum with primary beam chopping. (Red line) Energy spectrum with both stoppers and without primary beam chopping.

which are originally installed, to plastic scintillators for detecting β -decaying nuclides.

Figure 2.9 shows the GARIS-II focal plane setup for the present study. The cryogenic gas-cell (CGC) was cooled to 90 K and pressurized with helium gas at 100 mbar room temperature equivalent. Two independent Mylar energy degraders were used to adjust the ion stopping ranges in the CGC. A fixed $2.5\ \mu\text{m}$ retractable fixed degrader and a $5\ \mu\text{m}$ rotatable degrader provided an effective thickness ranging from $5\ \mu\text{m}$ to $9\ \mu\text{m}$.

Since there has been a lack of data on the mean charge states of intermediate-mass ions in dilute helium gas, intensity distribution measurement as a function of magnetic rigidity in GARIS-II is necessary for the first step of the experiment. β -decay is a three-body system, then β -rays have continuous energy distribution in contrast with α -particles. This could lead to a difficulty about optimum $B\rho$ -value search due to no possibility for extraction of β -rays fed by a certain nuclide without any gates. Fortunately, a region of now interest has several nuclides which have strikingly high Q_β -value to the others.

Figure 2.10 shows an overview of the β -activity counter. It consisted of double-layered, 1 mm and 2 mm thick plastic scintillators connected to 2×2 multi-anode photomultiplier tube (HAMAMATSU R5900U) via light guides. Two 1.5 mm copper plates were set which aim of energy degraders to suppress the low-energy β -rays ($E_\beta \lesssim 4\ \text{MeV}$) and reducing background events originating from Compton scattering events with unfavorable γ -rays. A Pb plate was also installed just after the second plastic scintillator for reduction of environmental, long-lived γ -ray events.

Detector system employed for adjustment of the ion transport system from the gas-cell to the MRTOF is shown in Fig. 2.11. Three β -activity counters, d-scinti, LTOF1, and LTOF2 were installed instead of the previous Si detectors. d-scinti, which consists of

2 cm cubic plastic scintillator and thin copper plate to make an electrostatic guide field for extracted ions by applying high-voltage of about -100 V, was used to optimization of CGC operation parameters and primary beam intensity dependence of gas-cell extraction efficiency. LTOF1 and LTOF2 consisted of 1 cm×1 cm square and 2 mm thick plastic scintillators, which are used as a telescope configuration in LTOF1 and to be alone in LTOF2. Both LTOF1 and LTOF2 were mounted on stepping motors, they could be fully removed from the beam line. The same type photomultiplier tubes (HAMAMATSU R7400P+E5780) were used for d-scinti, LTOF1, and LTOF2.

All plastic scintillators and light guides were wrapped by reflection sheets which are called “Luiremirror” [92] for suppressing light attenuation effects of the plastic scintillators. The reflectance of the “Luiremirror” is 97.5%.

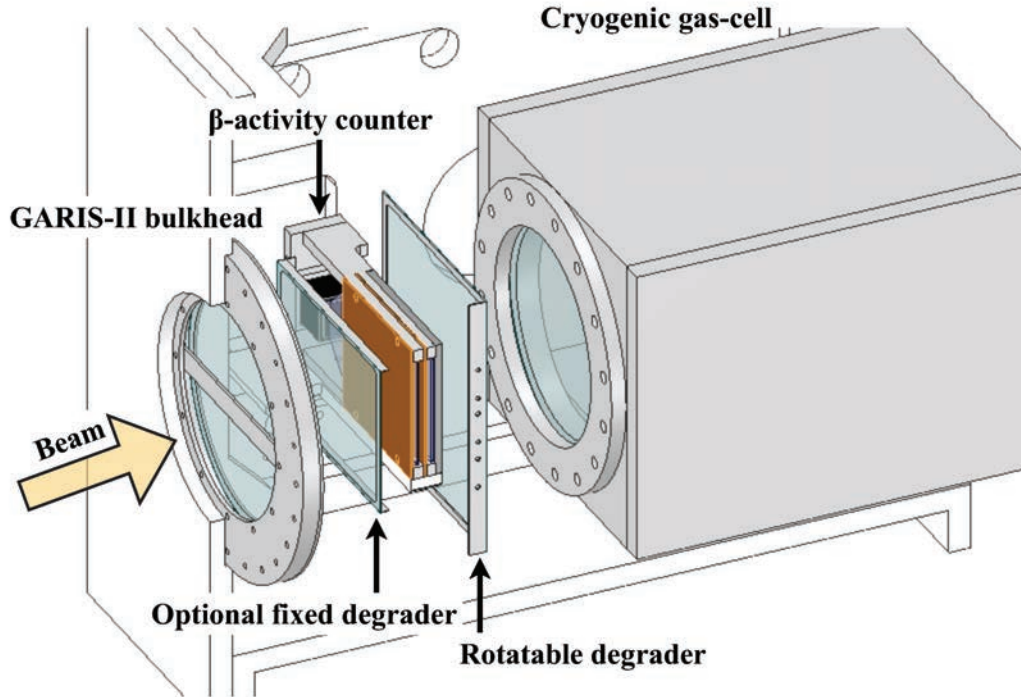


Figure 2.9: Schematic view of the GARIS-II focal plane setup. In the GARIS-II focal plane chamber, two energy degraders of different thickness Mylar films, a β -activity counter, and a cryogenic gas-cell were installed. The effective thickness of the rotatable degrader could be varied by changing its angle relative to the beam axis, while the optional fixed degrader and β -activity counter were mounted on independent air cylinders to allow them to be inserted and removed from the beam line as needed. A stainless steel bar was set in front of the GARIS-II bulkhead to protect its Mylar window from beam bombardments. The cryogenic gas-cell was pressurized with helium gas at 100 mbar room temperature equivalent, and cooled to 90 K.

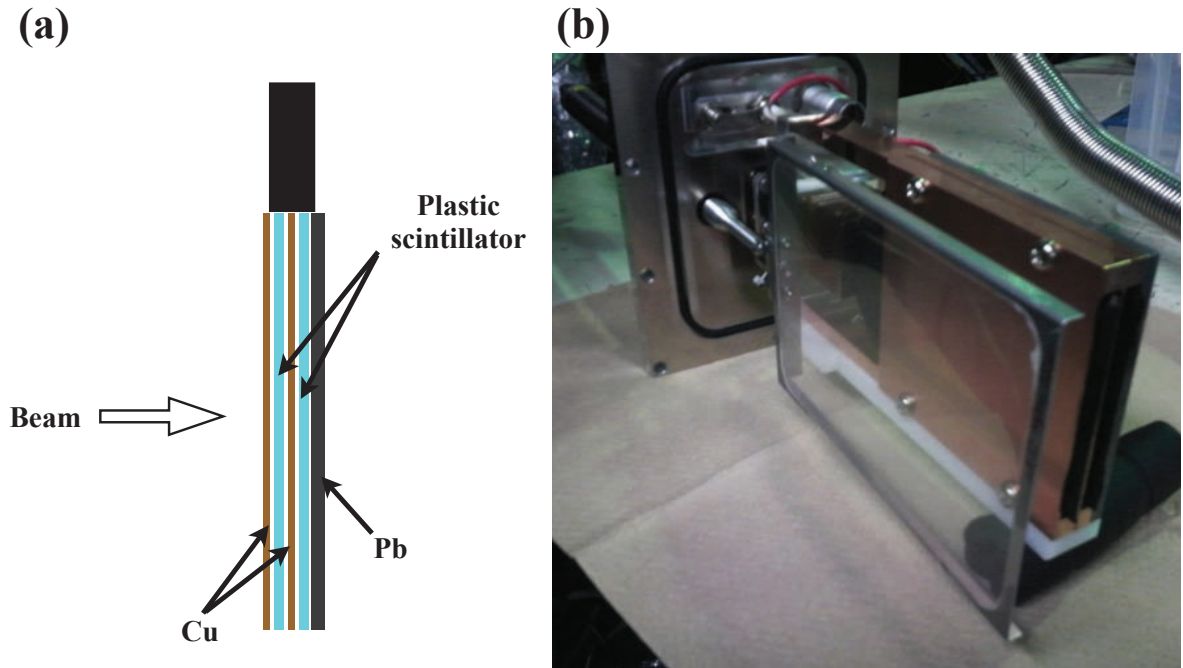


Figure 2.10: (a) Schematic view of the β -activity counter. (b) Photograph of the β -activity counter with the optional fixed degrader.

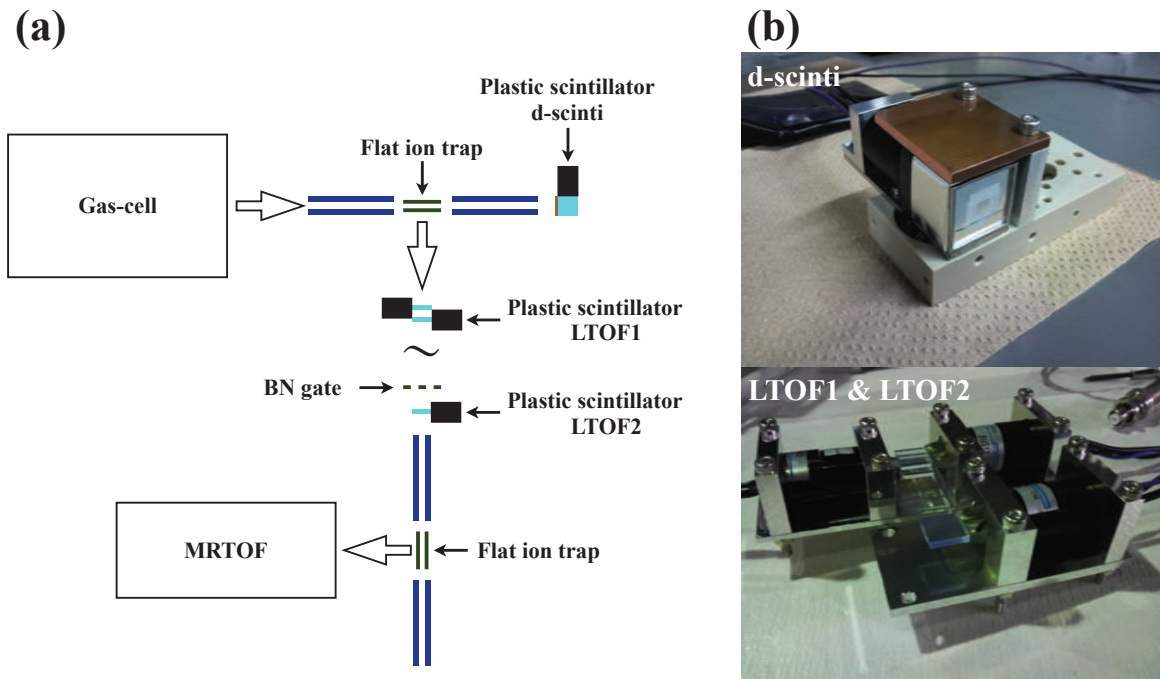


Figure 2.11: (a) Schematic view of the ion transport system. (b) Photographs of d-scinti, LTOF1, and LTOF2.

2.4 Target preparations

As the highest priority of mass measurements for the rp -process are ^{65}As and ^{66}Se , we aimed for the $A \approx 65$ region in the present study. The production cross section of ^{66}Se is predicted to be 120 nb, so targets of ^{32}S that are able to handle an intense ^{36}Ar beam irradiation were needed in order to access such small production cross section nuclei with non-negligible yields. As the natural abundance of ^{32}S is 95%, natural sulfur can be used for the production targets. However, because elemental sulfur is volatile, a chemically stable sulfur compound was needed. We chose to use molybdenum sulfide, $\text{Mo}^{\text{nat}}\text{S}_2$, due to it having a large sulfur composition ratio and being chemically stable.

The MoS_2 targets were prepared by a spray coating technique [93] on Ti backing foils. While MoS_2 is chemically stable, its stability to intense beam irradiation was uncertain. Thus, there was a need to confirm the irradiation tolerance of the MoS_2 targets.

A 40.6 MeV $^{35}\text{Cl}^{6+}$ beam, with average intensity of 20 pA, was provided by the 6 MV tandem electrostatic accelerator at University of Tsukuba. The experimental setup in the scattering chamber of the A7 course is shown in Fig. 2.12. A $\text{Mo}^{\text{nat}}\text{S}_2$ target on 3 μm Ti backing foil was mounted on a target ladder. The target thickness was 0.8 mg/cm². A Si detector and an ^{241}Am α -source were installed diagonally across the target ladder.

Measurements were performed by repeating the following procedure: irradiation of the $^{35}\text{Cl}^{6+}$ beam is carried out over a certain period of time and, subsequently, the thickness of $\text{Mo}^{\text{nat}}\text{S}_2$ target is measured via an energy spectrum of α -particles fed from the ^{241}Am source. Figure 2.13 shows the measured peak energy shift of the α -particle which passed through the $\text{Mo}^{\text{nat}}\text{S}_2$ target. In Fig. 2.13, no significant peak shift is observed for the beam irradiation up to $\sim 1200 \mu\text{C}$; it indicates that the beam irradiation does not affect the stability of the $\text{Mo}^{\text{nat}}\text{S}_2$ target. Total irradiation time was 3 hr. The present test corresponds to a 28 hr irradiation with 1 pA beam by considering that a 30 cm diameter rotating target wheel [94], which is used in the SHE-mass facility. Thus we confirmed that there is no problem in the stability of MoS_2 targets under the intense beam irradiation.

2.5 Online measurement

The online experiment was performed using a beam of $^{36}\text{Ar}^{10+}$ at 3.30 MeV/nucleon with a maximum intensity of 3 pA, which was provided by the RIKEN linear accelerator RILAC. Sixteen $\text{Mo}^{\text{nat}}\text{S}_2$ targets mounted on a 300 mm rotating wheel [94] were employed to produce proton-rich nuclei through fusion-evaporation reactions via $^{\text{nat}}\text{S}(^{36}\text{Ar}, \text{X})$. The $\text{Mo}^{\text{nat}}\text{S}_2$ targets were prepared by a spray coating technique [93] on 3 μm Ti backing foils. The average target thickness was 1.9 mg/cm². The wheel rotated at 2000 rpm during irradiation. The helium gas pressure of GARIS-II was set to 1 mbar during the measurements.

2.5.1 Mean charge state of intermediate-mass ions

Figure 2.14 shows the intensity distribution of β -activities as a function of magnetic rigidity. The largest peak around 1 Tm corresponds to reaction products of titanium, which is used as the backing material of the $\text{Mo}^{\text{nat}}\text{S}_2$ targets. The sulfur reaction products are located in small bump of 0.8 Tm. These count events were gated on β -ray energies by hardware, which is mentioned in Section 2.3. Then by considering production cross section, the largest

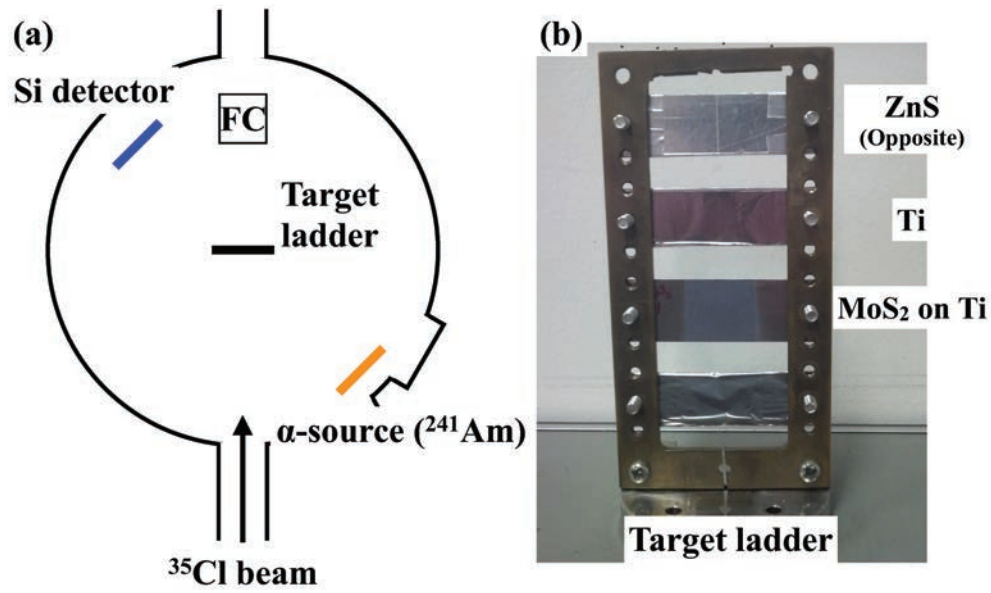


Figure 2.12: (a) the target irradiation test setup. (b) Photograph of the target ladder.

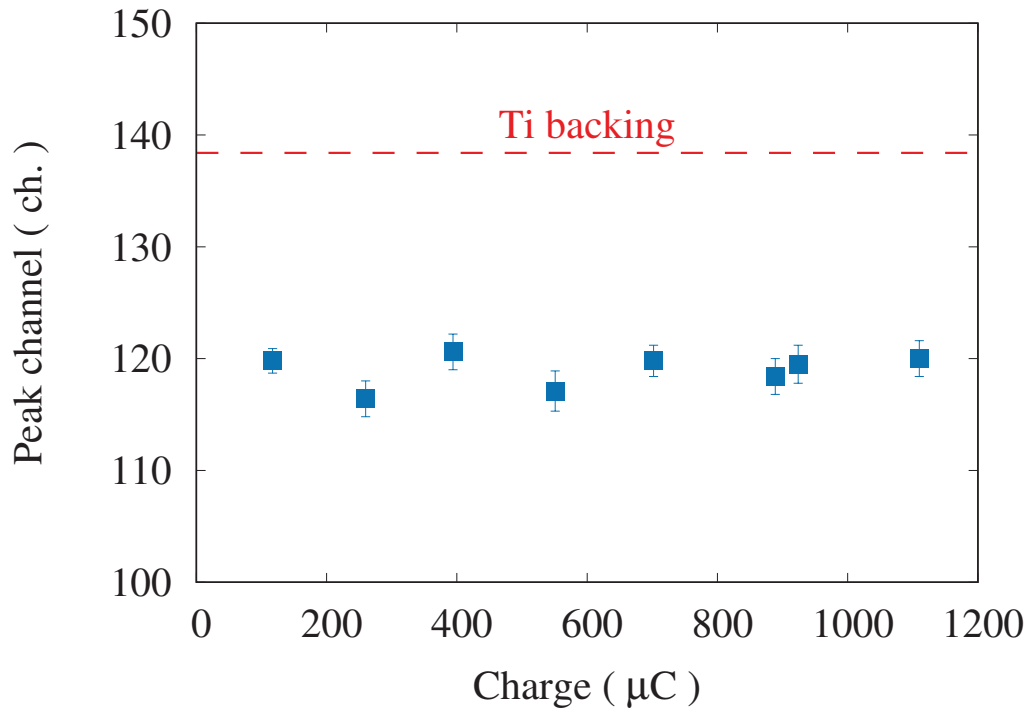


Figure 2.13: Peak energy shift of the α -particles. Red dashed line shows the peak position of the α -particles passed only through the Ti backing foil.

peak could be dominated by ^{80}Rb , which has $Q_{\beta+} = 4.7$ MeV [19]. Existence of ^{80}Rb was confirmed via lifetime measurement as shown in Fig 2.15.

In fitting procedure, it was assumed that the detected events consist of two components, which are dominated by a shorter lived one and a minor longer lived one. Then, a fitting function consisting of two components was employed,

$$f(t) = N_{0,s} \exp\left(-\frac{t - \tau_0}{\tau_{1/2,s}} \ln 2\right) + N_{0,l} \exp\left(-\frac{t - \tau_0}{\tau_{1/2,l}} \ln 2\right) \quad (2.1)$$

where $\tau_{1/2,s}$ and $\tau_{1/2,l}$ are half-lives of shorter and longer lived nuclides, respectively, and τ_0 is beam-off time. For short-lived one, $\tau_{1/2,s} = 34.7(8.3)$ sec was obtained. This value is consistent with the literature value for ^{80}Rb of $\tau_{1/2} = 33.4$ sec [95].

A prediction of the magnetic rigidity dependence of ^{80}Rb in terms of ion transport efficiency is also indicated in Fig. 2.14. The simulation methodology was the same as that employed for ion trajectory estimation (see Fig. 2.3). Predicted optimum $B\rho$ -value was 0.95 Tm, which was slightly lower than the experimental value of $B\rho = 1.017(2)$ Tm. A width of intensity distribution, $\Delta B\rho/B\rho$, which centers in $B\rho = 1.017(2)$ Tm, was obtained to be $(\Delta B\rho/B\rho)_{\text{exp}} = 11.9(6)\%$ by fitting with ± 0.1 Tm range from the peak center. Corresponding value of the simulation is evaluated to be $(\Delta B\rho/B\rho)_{\text{sim}} = 9.6(2)\%$ with the same fit condition.

The discrepancy between the experimental and the simulated optimum $B\rho$ -values evaluates to $\sim 6\%$. An empirical formula to determine the ion mean charge states in the GARIS-II simulation was adopted from Ref [88], which considers both a sinusoidal cor-

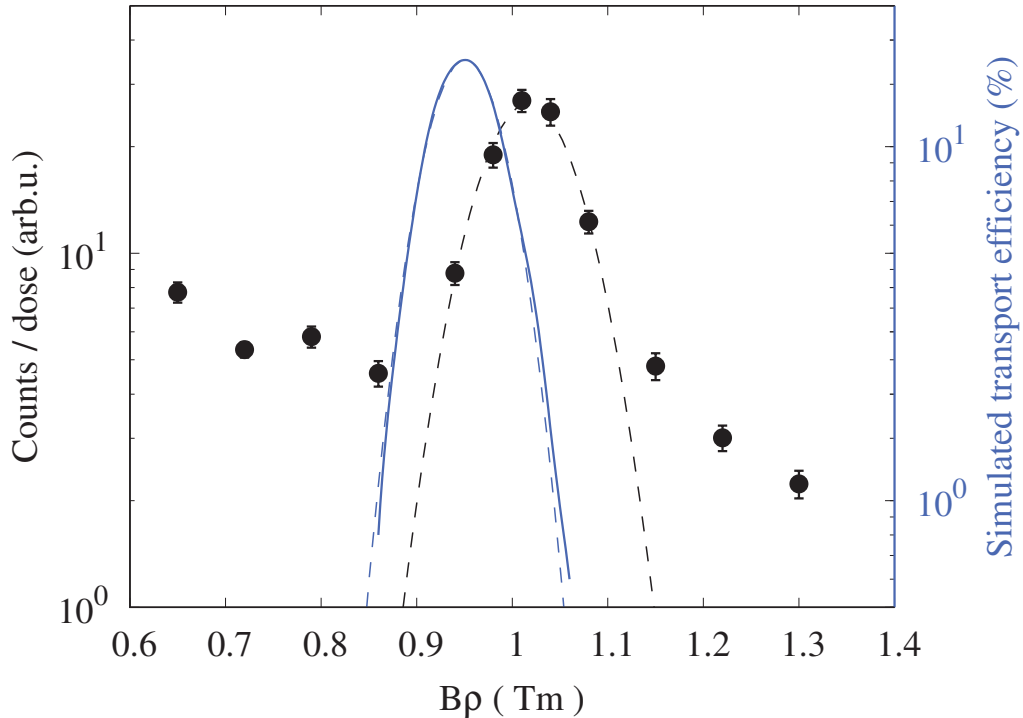


Figure 2.14: Intensity distribution of β -activities as a function of magnetic rigidity. Blue line represents the simulated transport efficiency of ^{80}Rb . Dashed lines show the fit results with gaussian distribution.

rection for the electronic shell structure of ions and a slow velocity collection, and is specialized for (super)heavy elements. Prediction power of this empirical formula is not enough for determine the optimum $B\rho$ -value among the intermediate-mass nuclides of the present study, but is useful as the first step of an optimum $B\rho$ -value search.

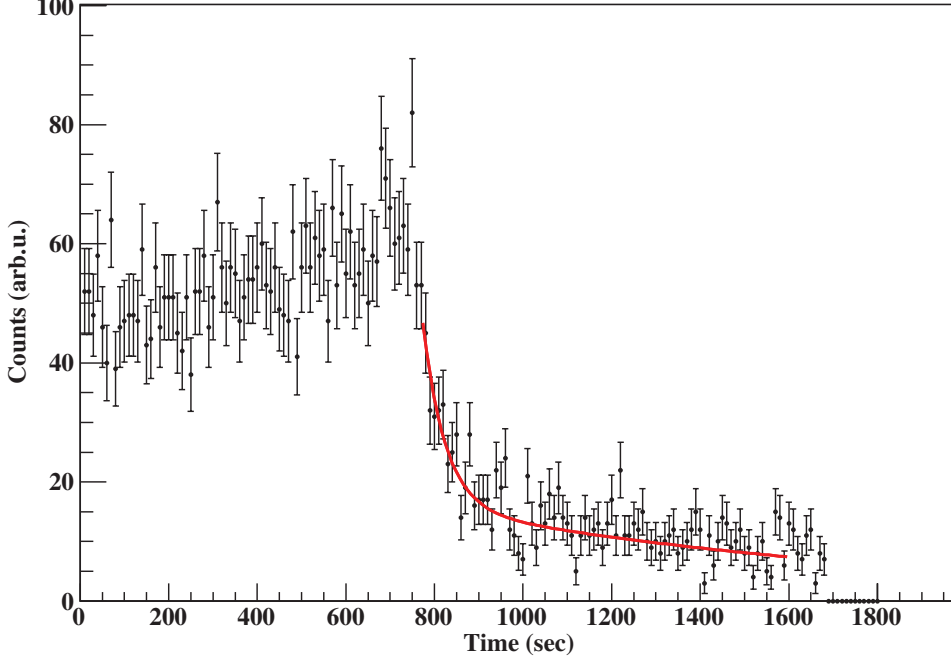


Figure 2.15: Lifetime measurement at the β -activity counter. Red lines represents a fitting result.

2.5.2 Space charge effects on the gas-cell extractions

The gas-cell extraction efficiency has an inverse dependence on the incoming ion rate due to space-charge effects. This dependency can be divided into two distinct regions: a plateau at low incoming rates followed by a reduction at larger incoming rates. In the latter region, the behavior can be represented by the empirical formula [91],

$$\epsilon = \epsilon_0 \left(\frac{I}{I_0} \right)^{-\alpha}, \quad (2.2)$$

where I is the incoming rate of ions and α is a constant. Other constants, I_0 and ϵ_0 , are the typical values of gas-cell: $\epsilon_0 = \epsilon(I_0)$. The α value has been evaluated to be 0.53 [91] in the case of the prototype SLOWRI gas-cell using ^8Li beam produced by fragmentation reactions, and 0.067 [96] for the present gas-cell for heavy elements from the $^{169}\text{Tm}(^{40}\text{Ar}, 4n)^{205}\text{Fr}$ reaction.

An α value measurement was performed in the present study by counting the β -activity events at the plastic scintillator called “d-scinti”, which is installed downstream of the gas-cell (see Fig. 2.11). Measurement results are shown in Fig 2.16. By fitting with Eq. 2.2, $\alpha = 0.46(2)$ was obtained in the present study. This value is far from ^{205}Fr case which likely corresponds to the plateau region, and closer to that of the prototype SLOWRI gas-cell.

This result indicates that a dominant part of space charge effects could be originated from the some energetic ions such as primary beam particle and recoil ions with them. There is non-negligible influence of the primary beam to gas-cell extraction efficiency and there is room to decrease the space charge effects by improving the primary beam separation.

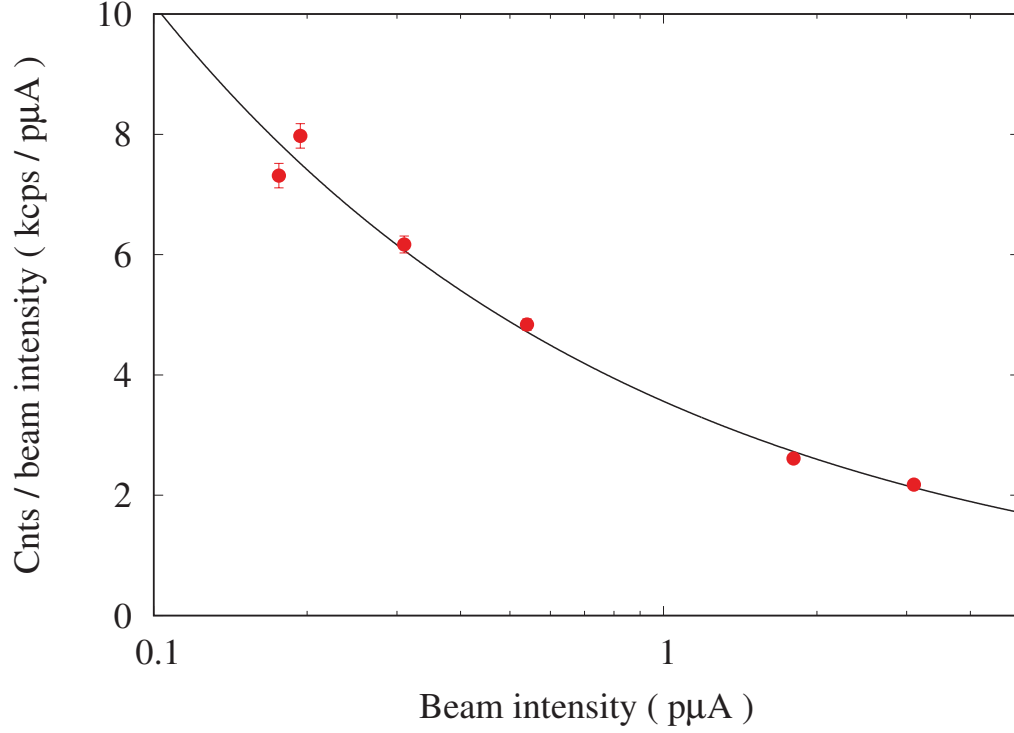


Figure 2.16: Primary beam intensity dependence of gas-cell extraction efficiencies. Black line indicates the fit result with Eq. 2.2.

Chapter 3

ANALYSIS

3.1 Analysis method

The time-of-flight (TOF) values varied as a function of time due to thermal expansion of the MRTOF-MS device and minor instabilities in the HV power supply system for mirror electrodes [70]. These TOF drifts could be compensated by use of isobaric reference species. Before performing such a correction, we first calculated the “standard TOF” of the reference, defined as the TOF determined by fitting the raw TOF data. The raw data were then divided by equal sweeps (measurement times) into i subsets. For ions in each subset i the corrected TOF $t_{\text{corr},i}$ was calculated with the following relation:

$$t_{\text{corr},i} = t_{\text{raw},i} \left(\frac{t_{\text{std}}}{t_i} \right), \quad (3.1)$$

where $t_{\text{raw},i}$ is the uncorrected TOF of each ion in subset i , while t_{std} and t_i are the standard TOF of the isobaric reference species, which is determined by peak fit of accumulated raw TOF data, and the fitted center of the isobaric reference species within the i^{th} subset, respectively. Schematic view of the drift compensation is shown in Fig. 3.1. After applying corrections to each subset, the data were recombined for precision peak fitting. This correction method was applied to all the data presented here.

To determine the masses of observed nuclides, the single reference method [69] was adopted. This method makes use of the delay between ion ejection and TDC start time, t_0 , which has been directly measured to be 40(10) ns. If t_X and t_{ref} are the measured TOF of nuclide X and the reference ion, respectively, then their true TOF would be $t_X - t_0$ and $t_{\text{ref}} - t_0$. We can then define ρ^2 :

$$\rho^2 = \frac{m_{\text{ref}}}{m_X} = \left(\frac{t_X - t_0}{t_{\text{ref}} - t_0} \right)^2, \quad (3.2)$$

where m_X and m_{ref} are the masses of nuclide X and the reference ion, respectively.

In the present measurements, we measured only singly-charged ions. Thus, the atomic mass of nuclide X, M_X , is given by

$$M_X = \rho^2(M_{\text{ref}} - m_e) + m_e, \quad (3.3)$$

where M_{ref} and m_e are the atomic mass of the reference nuclide and the electron rest mass, respectively. For mass values of the references, the 2016 Atomic Mass Evaluation (AME16) values [23, 19] were adopted.

Excluding low statistics species, the least squares fitting routine of the ROOT package [97] was used to determine TOF ratios ρ . For the low statistics cases the maximum likelihood method was used. Figure 3.2 shows an algorithm of the analysis program.

For maximum reliability, the fitting ranges must be determined in a consistent manner. It was decided to define the fitting range as the region(s) where the fit function was greater than 0.1. In this way the range was adjusted dynamically during the fitting process, where the range used for the j^{th} iteration was determined using the parameters from the $(j-1)^{\text{th}}$ iteration. Due to the use of a multi-peak fit function, the fitting region was not necessarily contiguous, as regions with zero ions may be present when peaks are well-separated, and the inclusion of such regions can adversely bias the χ^2 of the fit.

Fitting procedures were iterated until the fit parameters are converged. A convergence condition,

$$\left[\frac{1}{2N} \sum_{i=1}^{2N} \left(\frac{x_i^{(j)} - x_i^{(j-1)}}{x_i^{(j-1)}} \right)^2 \right]^{1/2} \leq 10^{-9}, \quad (3.4)$$

was adopted, where $x_i^{(j)}$ is the i^{th} fit parameter i at the j^{th} step and N is the number of species of interest.

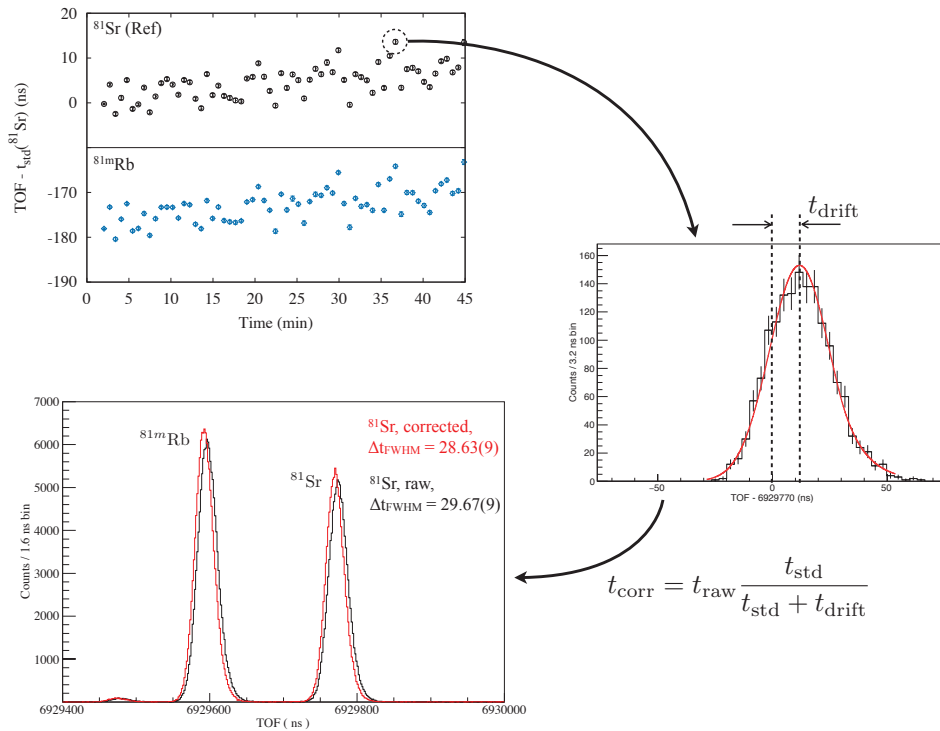


Figure 3.1: Process of time-of-flight (TOF) drift compensation. Raw time data are divided in some subset. For reference nuclei (^{81}Sr in this figure), their deviations t_{drift} from the standard TOF value are determined for each subset. By using the obtained t_{drift} , corrections of the TOF value for all subset are performed with Eq. 3.1 ($t_i = t_{\text{std}} + t_{\text{drift}}$). Improvement of the peak width can be seen in left-bottom panel which shows a comparison between the raw and the corrected TOF spectra. In this figure data of $A/q = 81$ and $\text{lap} = 221$ are used as an example.

To evaluate fitting errors correctly, a scaling factor,

$$s_{\text{hist}} = \chi_{\nu}^2, \quad (3.5)$$

was introduced. If χ_{ν}^2 -values exceeded unity, the statistical error of histogram were increased via multiplying by s_{hist} to χ_{ν}^2 becomes unity. In some cases where χ_{ν}^2 -values were less than one, to avoid overfitting, wider histogram bin widths were adopted.

3.2 Fitting function

A high-quality fitting function, based on an exponential-Gaussian hybrid function [69, 70, 98], was developed through the study of high-statistics offline measurements of $^{85}\text{Rb}^+$ ions. A typical TOF spectrum of $^{85}\text{Rb}^+$ ions is shown in Fig. 3.3. In order to reproduce the shape of main peak, we employed the function:

$$f_p(\tau) = \begin{cases} \mu \exp[-\tau^2/\nu] & (\text{for } t < t_{s1}) \\ \xi \exp[\eta/\tau^2] & (\text{for } t_{s1} \leq t < t_{s2}) \\ (\kappa/\sigma) \exp[-\tau^2/(2\sigma^2)] & (\text{for } t_{s2} \leq t < t_{s3}) \\ (\kappa/\sigma) \exp[t_{s3}(t_{s3} - 2\tau)/(2\sigma^2)] & (\text{for } t \geq t_{s3}), \end{cases} \quad (3.6)$$

where the characteristic times t_{si} indicate the available range of each sub-function. The variable τ is defined as: $\tau \equiv t - t_c$, where t_c is the peak center. Thus, f_p has seven independent parameters, not including the characteristic times t_{si} . The number of parameters can be analytically reduced to three by imposing the continuity condition at each time t_{si} ; the remaining independent parameters are then t_c, κ , and σ .

In addition to the primary peaks, we observed ‘‘bump’’ structures neighboring the intense peaks in sufficiently high-statistics TOF spectra. These bumps maintain a constant intensity and position relative to the primary peak and are deduced to result from the following process: secondary electrons are emitted from the surface of the MCP ion detector, they accelerate to nearby surfaces and produce tertiary ions which accelerate back to the MCP. Hence, these bumps are not actual events and depend only on the intensities of parent peaks. The bump shapes are modeled with the following Gaussian function,

$$f_b(\tau) = (\kappa_b/\sigma_b) \exp[-(\tau - t_b)^2/(2\sigma_b^2)]. \quad (3.7)$$

All independent parameters of the fitting function including the switching times were obtained as an average of the off-line measurement results of the $^{85}\text{Rb}^+$ ions with two different laps and results. In the fitting algorithm, t_{s1} and t_{s2} were determined by scaling the σ parameter of mass reference peaks relative to that of $^{85}\text{Rb}^+$:

$$t_{si} = t_{si,85\text{Rb}} \times (\sigma/\sigma_{85\text{Rb}}) \quad (i = 1, 2). \quad (3.8)$$

The t_{s3} values were determined as independent parameters in fitting the mass reference nuclide peaks, then fixed for each isobaric species of interest. The bump height parameter κ_b was calculated assuming a constant relative intensity,

$$\kappa_b = \kappa_{b,85\text{Rb}} \times (\kappa/\kappa_{85\text{Rb}}). \quad (3.9)$$

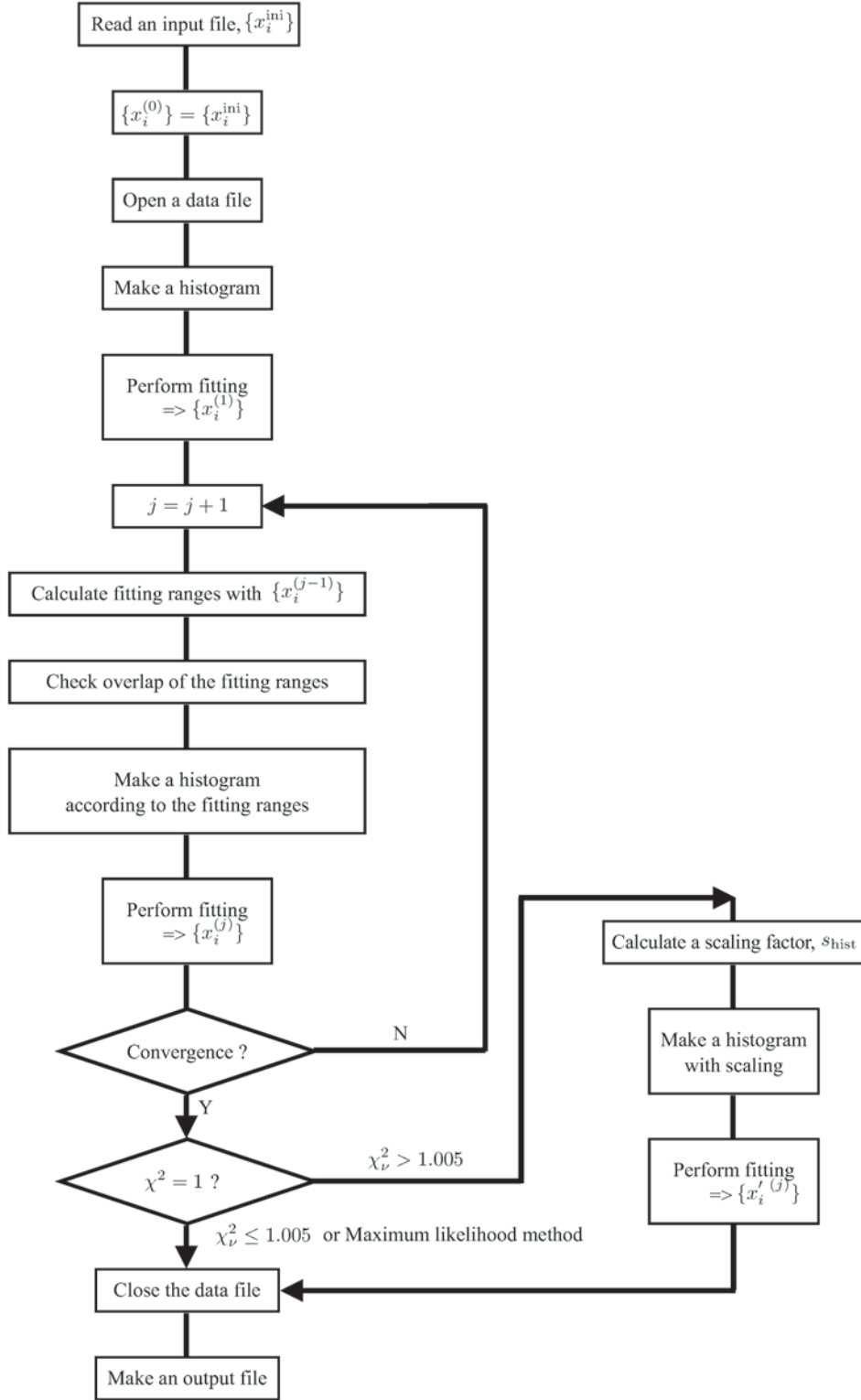


Figure 3.2: Flow chart of the analysis program. $\{x_i^{(j)}\}$ denotes a set of all fitted parameters at j^{th} step. Details are shown in the texts.

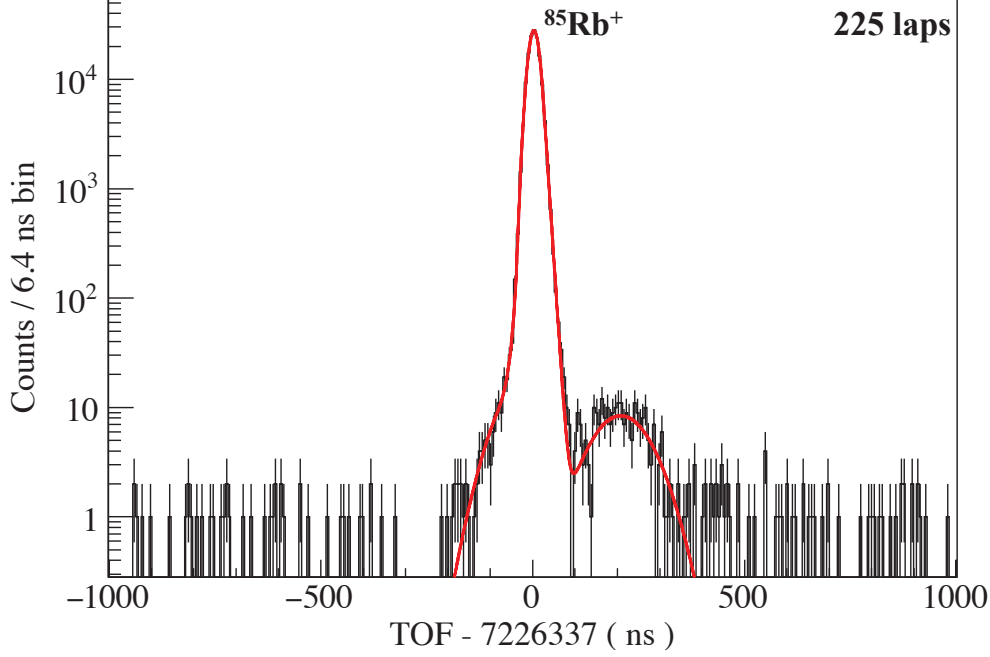


Figure 3.3: Typical time-of-flight spectrum of $^{85}\text{Rb}^+$ ions. Such spectra were used to determine the fitting function, indicated by a red line, based on an exponential-Gaussian hybrid function.

The other two bump parameters, σ_b and t_b , were fixed based on $^{85}\text{Rb}^+$ fitted results.

For the species of interest, the only free parameters in the fitting function are the peak center t_c and the peak height κ . The σ and t_{s3} parameters were determined from the mass reference values. In the fitting algorithm, to enhance the mass precision, the τ parameter was treated as a function of t , t_{ref} , and ρ , where ρ is the TOF ratio from Eq. 5.5. Then the fitting function F for N peaks is described by

$$\begin{aligned}
 F(t, t_{\text{ref}}, \rho_1, \dots, \rho_N, \kappa_1, \dots, \kappa_N) &= \sum_{i=1}^N F_i(t, t_{\text{ref}}, \rho_i, \kappa_i) \\
 &= \sum_{i=1}^N \{f_p(t, t_{\text{ref}}, \rho_i, \kappa_i) + f_b(t, t_{\text{ref}}, \rho_i, \kappa_i)\}. \quad (3.10)
 \end{aligned}$$

If the i^{th} peak corresponds to the mass reference, ρ_i is always unity; the total number of fitting parameters is $2 \times N$.

3.3 Error evaluation

The uncertainty in the atomic mass of nuclide X calculated by Eq. 3.3 can be evaluated as:

$$\delta M_X = \sqrt{(M_{\text{ref}} - m_e)^2 \delta(\rho^2)^2 + \rho^4 \delta M_{\text{ref}}^2 + (1 - \rho^2)^2 \delta m_e^2}, \quad (3.11)$$

where $\delta(\rho^2)$, δM_{ref} , and δm_e are the error of mass ratio ρ^2 , the uncertainty of the reference nuclide's atomic mass, and the uncertainty of the electron rest mass, respectively. The

contribution of the third term of Eq. 3.11 is negligibly small for the present study. The uncertainty of mass reference nuclides δM_{ref} were adopted from AME16.

We consider that the mass ratio error $\delta(\rho^2)$ consists of terms originating from fitting procedure, the drift compensation, and the constant time offset t_0 :

$$\delta(\rho^2) = 2\rho \sqrt{\delta\rho_{\text{fit}}^2 + \left(\frac{\partial\rho}{\partial t_{\text{drift}}}\right)^2 \delta t_{\text{drift}}^2 + \left(\frac{\partial\rho}{\partial t_0}\right)^2 \delta t_0^2}. \quad (3.12)$$

The TOFs of both nuclide X and mass reference nuclide compensated by Eq. 3.1 with same reference TOF data set $\{t_i\}$ are used to evaluate ρ values. The uncertainties of drift compensation of each TOF value must be treated in the same manner. Thus the influence of such uncertainties on δt_{drift} can be found to be strongly correlated: a coefficient of δt_{drift} can be written as

$$\frac{\partial\rho}{\partial t_{\text{drift}}} = \left(\frac{\partial\rho}{\partial t_X}\right) \frac{dt_X}{dt_{\text{drift}}} + \left(\frac{\partial\rho}{\partial t_r}\right) \frac{dt_r}{dt_{\text{drift}}}. \quad (3.13)$$

Total differential parts of variable t_X and t_r are calculated from Eq. 3.1 by considering t_i is given as a summation of t_{std} and t_{drift} ,

$$\frac{dt}{dt_{\text{drift}}} = \frac{d}{dt_{\text{drift}}} \left(t_{\text{raw}} \frac{t_{\text{std}}}{t_{\text{std}} + t_{\text{drift}}} \right) = -\frac{t}{t_i} \quad (t = t_X, t_r). \quad (3.14)$$

By substituting the above relation for Eq. 3.13, one can get

$$\begin{aligned} \frac{\partial\rho}{\partial t_{\text{drift}}} &= - \left[\left(\frac{\partial\rho}{\partial t_X}\right) t_X + \left(\frac{\partial\rho}{\partial t_r}\right) t_r \right] \frac{1}{t_i} \\ &= - \frac{(1-\rho)t_0}{t_r - t_0} \frac{1}{t_i} \\ &\approx (\rho - 1) \frac{t_0}{t_r^2}, \end{aligned} \quad (3.15)$$

where $t_r \approx t_r - t_0$ and $t_r \approx t_i$ are assumed in the last line. By using typical values of the present measurements, the contribution of drift compensation is estimated to be

$$\frac{\partial\rho}{\partial t_{\text{drift}}} \delta t_{\text{drift}} = (\rho - 1) \frac{t_0}{t_r} \frac{\delta t_{\text{drift}}}{t_r} \sim 10^{-16} \left(\frac{\rho - 1}{10^{-4}} \right) \left(\frac{t_0/t_r}{10^{-5}} \right) \left(\frac{\delta t_{\text{drift}}/t_r}{10^{-7}} \right), \quad (3.16)$$

which is negligibly small as compared to the main contribution $\delta\rho_{\text{fit}} \sim 10^{-7}$, assuming $\delta t_{\text{drift}} = 0.5$ ns. One reason for this negligible contribution is the correlation between t_x and t_r . If one assumes that there are no correlations in the drift compensation errors appearing in both t_x and t_r , they become significantly larger values, which are on the order of the error budget of $\delta(\rho^2)$.

The TOF ratio ρ has the constant time offset value t_0 as a parameter. The coefficient of δt_0 term is easily calculated to be

$$\frac{\partial\rho}{\partial t_0} \delta t_0 = \frac{t_X/t_r - 1}{(1 - t_0/t_r)^2} \frac{\delta t_0}{t_r} \approx (\rho - 1) \frac{\delta t_0}{t_r} \sim 10^{-10} \left(\frac{\rho - 1}{10^{-4}} \right) \left(\frac{\delta t_0/t_r}{10^{-6}} \right). \quad (3.17)$$

From this formula a value of δt_0 term is evaluated to be the order of 10^{-10} , negligibly small as compared to the $\delta(\rho^2)$ error budget in the present measurements. More detailed

discussion about the influence of δt_0 term can be found in Ref [99]. Then the $\delta(\rho^2)$ of each measurement is determined by

$$\delta(\rho^2) = 2\rho\delta\rho_{\text{fit}}. \quad (3.18)$$

Measurements were performed with two or more different lap values for each A/q series. Then the final results of these \mathcal{N} measurements belonging to the same A/q series were obtained as their weighted average,

$$\overline{\rho^2} = \frac{\sum_{i=1}^{\mathcal{N}} w_i^2 \rho_i^2}{\sum_{i=1}^{\mathcal{N}} w_i^2}, \quad (3.19)$$

$$\delta(\overline{\rho^2}) = \frac{1}{\sqrt{\sum_{i=1}^{\mathcal{N}} w_i^2}}, \quad (3.20)$$

where w_i is a weight of each measurement and is defined by

$$w_i \equiv \frac{1}{s_{\text{err}}\delta(\rho_i^2)}. \quad (3.21)$$

A parameter s_{err} is set to be one in general. Consistency of the measurements, namely $\overline{\rho^2}$ values, was confirmed via the chi-square test. Observed chi-square value χ_{obs}^2 of \mathcal{N} measurements was given by following formula:

$$\chi_{\text{obs}}^2 = \sum_{i=1}^{\mathcal{N}} w_i^2 \left(\rho_i^2 - \overline{\rho^2} \right)^2 \quad (3.22)$$

If the measurements are consistent to each other, χ_{obs}^2 is smaller than the chi-square values of 95% confidence level, $\chi_{95\%}^2(\mathcal{N}-1)$. In the case of that χ_{obs}^2 is larger than the $\chi_{95\%}^2(\mathcal{N}-1)$, it was assumed that the inconsistency comes from underestimation of each measurement error and s_{err} was adjusted to a level that restored the consistency of the measurements.

Chapter 4

RESULTS

Mass measurements were performed with two different settings of GARIS-II: $B\rho = 0.86$ Tm and $B\rho = 1.01$ Tm, corresponding to reaction products from the sulfur targets ($A = 65-67$) and reactions products from the titanium backings ($A = 79-81$), respectively. Atomic and molecular ions of 25 species were found within the TOF spectra of six different isobaric chains. To maximally suppress mass dependent systematic errors, isobaric references within each isobaric chain were used. Two conditions in the choice of mass reference nuclides were set:

- The mass reference nuclides should be evaluated as “absolute mass-doublet nuclide” in AME16.
- The mass reference nuclides must have no known long-lived isomeric states.

Time-of-flight (TOF) spectra and fit results of each measurement are indicated in Fig. 4.1 to 4.13 and Fig. 4.14 to 4.19, respectively. A summary of the results is shown in Table 4.1 and Fig 4.20. The relative precisions in the present study span the range of $\delta m/m \sim 10^{-7}$ to 10^{-8} . In most cases, the agreement with AME16 is excellent. To understand the few inconsistencies between the present study and AME16 two reliability requirements were imposed on the mass values:

- There are no known, or suspected, long-lived isomeric states of the nuclide.
- A valley must exist between adjacent peaks, and the peak amplitudes must exceed the height of the valley by at least one order of magnitude.

These requirements derive from the mass resolving power of our MRTOF-MS, which does not reach the level needed to distinguish between mass differences below several hundred keV in the range of A/q under study. While it is possible to fit data with unresolved peak convolution, the reliability of such an approach is insufficient for the high-precisions sought in the study of this region.

4.1 $A/q = 65$

For $A/q = 65$ series, mass measurements were performed with three different lap values (225-227 laps). TOF spectra are shown in Fig. 4.1 and 4.2. ^{65}Cu was employed as the mass reference. All mass excess values in this series were in agreement with the AME16 values. For ^{65}Ga , a mass uncertainty of 2.1 keV, corresponding to a relative precision of

$\delta m/m = 3.5 \times 10^{-8}$, was obtained. This is the most precise measurement yet performed by MRTOF-MS. The accumulated number of ^{65}Ga events was 1.9×10^4 .

4.2 $A/q = 66$

Mass excess values of the $A/q = 66$ series were obtained from measurements with six different lap values (223-227, 299 laps). Here, ^{66}Zn was used as the mass reference. A discrepancy with the AME16 value was found for ^{66}Ga . However, from Fig. 4.3 to 4.5 it can be seen that ^{66}Ga peaks are located in the bump structures of ^{66}Zn peaks and they do not satisfy the second reliability requirement. The mass of the peak located between $^{66}\text{Ge}^+$ and $^{65}\text{GeH}^+$, $ME = -55951(14)$ keV, is consistent with the sulfur-dimer $^{32}\text{S}^{34}\text{S}^+$, $ME(^{32}\text{S}^{34}\text{S}) = -55947.22(4)$ keV, however, the source of such a molecule is unclear and only a tentative assignment is made.

4.3 $A/q = 67$

In the $A/q = 67$ series, four measurements (223-225, 227 laps) were performed. The mass reference in this series was ^{67}Zn . The mass values of two nuclides, ^{67}Ga and ^{67}Ge , were inconsistent with the AME16 values. It is seen in Fig. 4.6 and 4.7 that the ^{67}Ga peaks are fully embedded in the ^{67}Zn peaks, eliminating ^{67}Ga from further discussion. In contrast to the case of ^{67}Ga , the ^{67}Ge peaks are well-resolved. The discrepancy in the ^{67}Ge mass value was evaluated to be 17 keV, which corresponds to 2.4σ . The ^{67}Ge mass value of AME16 was evaluated by an indirect method, namely threshold measurements of the $^{64}\text{Zn}(\alpha, n)^{67}\text{Ge}$ reaction [100, 101]. The threshold of $^{64}\text{Zn}(\alpha, n)^{67}\text{Ge}$ was extrapolated by using the correlation between the induced α -particle energy and yields of the γ -rays of ^{67}Ge . In this method the effects of Coulomb interactions cannot be completely removed, leaving some ambiguity in the ^{67}Ge mass value. A new mass excess value, $ME = -62675.2(46)$ keV for ^{67}Ge is proposed.

4.4 $A/q = 79$

For the $A/q=79$ series, ^{79}Rb was taken as the mass reference since it is the highest intensity nuclide in the set which has previously been evaluated in a Penning trap measurement [21] and has no known long-lived isomeric states. There are five measurements in this series (224, 225, 227-229 laps). The mass values obtained for ^{79}Br and ^{79}Sr are in good agreement with those in AME16. The discrepancy of the $^{79\text{m}}\text{Kr}$ mass value is set aside due to an unresolved, long-lived isomeric state.

4.5 $A/q = 80$

There are two measurements with different lap values (224 and 225 laps) for the $A/q = 80$ series. ^{80}Kr was taken as the mass reference since it is the only nuclide which satisfies the requirements to be a mass reference. The mass value of ^{80}Sr in the present study is inconsistent with the AME16 value. However, as can be seen in Fig. 4.11 the second reliability requirement is not met.

4.6 $A/q = 81$

In the $A/q = 81$ series, mass excess values were determined by four measurements with different lap values (221, 222, 224, and 225 laps). ^{81}Sr was selected as a mass reference for the $A/q = 81$ series since its mass value was determined by Penning trap measurements [102, 103] and it also provides high-intensity peaks. In addition, ^{81}Sr has no known long-lived isomeric states. In this series inconsistent mass values were found for two nuclides: $^{81\text{m}}\text{Rb}$ and ^{81}Br . For $^{81\text{m}}\text{Rb}$ we dismiss the discrepancy as being due to the admixture of an unresolved, long-lived isomeric state. The ^{81}Br peak, however, satisfies the reliability requirements. As in the case of ^{67}Ge , the mass value of ^{81}Br was evaluated using the results of indirect measurements connecting to the absolute mass-doublet nuclide ^{82}Kr : $^{81}\text{Br}(n, \gamma)^{82}\text{Br}(\beta^-)^{82}\text{Kr}$. We claim that the connection between ^{82}Br and ^{82}Kr is susceptible to error since it depends on a β -decay endpoint measurement [104]. It has been pointed out that β -decay endpoint measurements are often unreliable [25]. A new mass excess value for ^{81}Br of $\text{ME} = -77955.4(53)$ keV is proposed.

Table 4.1: The squares of time-of-flight ratio ρ^2 , which are equivalent to the mass ratio, and the mass excess values ME_{exp} in the present study. The nuclides used as atomic mass references are shown in column “Ref.”. ME_{lit} indicates mass excess values from AME16 and ΔME represents the differences between mass excess values found in AME16 and those of the present study: $\Delta\text{ME} \equiv \text{ME}_{\text{exp}} - \text{ME}_{\text{lit}}$. The $\delta m/m$ column provides relative mass precisions of the present measurements. The brackets in the ΔME column denote measurements that do not satisfy the reliability conditions as described in the text. The bracket shape designates which criterion was not satisfied: $\langle \dots \rangle$ denotes contamination with unresolvable isomers and $[\dots]$ indicates the undue influence of intense neighboring peaks.

Species	Ref.	ρ^2	ME_{exp} (keV)	ME_{lit} (keV)	ΔME (keV)	$\delta m/m$
$^{63}\text{Cu}^1\text{H}_2^{16}\text{O}^+$	$^{81}\text{Sr}^+$	1.00020961(17)	−55728(13)	−55738.9(4)	11(13)	1.8×10^{-7}
$^{64}\text{Zn}^1\text{H}^+$	$^{65}\text{Cu}^+$	1.00014125(25)	−58721(15)	−58715.0(6)	−6(15)	2.5×10^{-7}
$^{65}\text{Zn}^+$	$^{65}\text{Cu}^+$	1.00002247(20)	−65905(12)	−65912.0(6)	7(12)	2.0×10^{-7}
$^{66}\text{Zn}^1\text{H}^+$	$^{67}\text{Zn}^+$	1.00010072(22)	−61602(14)	−61610.2(7)	9(14)	2.2×10^{-7}
$^{65}\text{Ga}^+$	$^{65}\text{Cu}^+$	1.000076165(33)	−62657.3(21)	−62657.5(8)	0.2(22)	3.5×10^{-8}
$^{66}\text{Ga}^+$	$^{66}\text{Zn}^+$	1.00008385(16)	[−63749.8(97)]	−63723.7(11)	[−21.6(97)]	1.6×10^{-7}
$^{67}\text{Ga}^+$	$^{67}\text{Zn}^+$	1.00001662(16)	[−66845(10)]	−66879.0(12)	[35(10)]	1.6×10^{-7}
$^{65}\text{Ge}^+$	$^{65}\text{Cu}^+$	1.00017854(34)	−56465(20)	−56478.2(22)	13(20)	3.4×10^{-7}
$^{65}\text{Ge}^1\text{H}^+$	$^{66}\text{Zn}^+$	1.00032130(37)	−49168(23)	−49189.2(22)	21(23)	3.8×10^{-7}
$^{66}\text{Ge}^+$	$^{66}\text{Zn}^+$	1.00011868(21)	−61611(13)	−61607.0(24)	−4(13)	2.1×10^{-7}
$^{67}\text{Ge}^+$	$^{67}\text{Zn}^+$	1.000083493(73)	−62675.2(46)	−62658(5)	−17(7)	7.4×10^{-8}
$^{67}\text{As}^+$	$^{67}\text{Zn}^+$	1.00018112(41)	−56589(26)	−56587.2(4)	−2(26)	4.1×10^{-7}
$^{79}\text{Br}^+$	$^{79}\text{Rb}^+$	0.999928378(63)	−76068.4(51)	−76068.0(10)	−0.4(52)	7.0×10^{-8}
$^{81}\text{Br}^+$	$^{81}\text{Sr}^+$	0.999914739(60)	−77955.4(53)	−77977.0(10)	21.6(54)	7.0×10^{-8}
$^{79\text{m}}\text{Kr}^+\text{a}$	$^{79}\text{Rb}^+$	0.99995185(12)	$\langle -74342.7(93) \rangle$	−74312(3)	$\langle -30(10) \rangle$	1.3×10^{-7}
$^{80}\text{Rb}^+$	$^{80}\text{Kr}^+$	1.00007668(15)	−72185(11)	−72175.5(19)	−10(11)	1.5×10^{-7}
$^{81\text{m}}\text{Rb}^+\text{b}$	$^{81}\text{Sr}^+$	0.999948753(11)	$\langle -75391.5(29) \rangle$	−75371(5)	$\langle -21(6) \rangle$	3.9×10^{-8}
$^{79}\text{Sr}^+$	$^{79}\text{Rb}^+$	1.00007227(22)	−65490(16)	−65477(8)	−13(18)	2.2×10^{-7}
$^{80}\text{Sr}^+$	$^{80}\text{Kr}^+$	1.00010148(20)	[−70339(15)]	−70311(3)	[−28(15)]	2.0×10^{-7}

^a $E_X = 129.77$ keV, $t_{1/2} = 50$ sec [105]

^b $E_X = 86.31$ keV, $t_{1/2} = 30.5$ min [106]

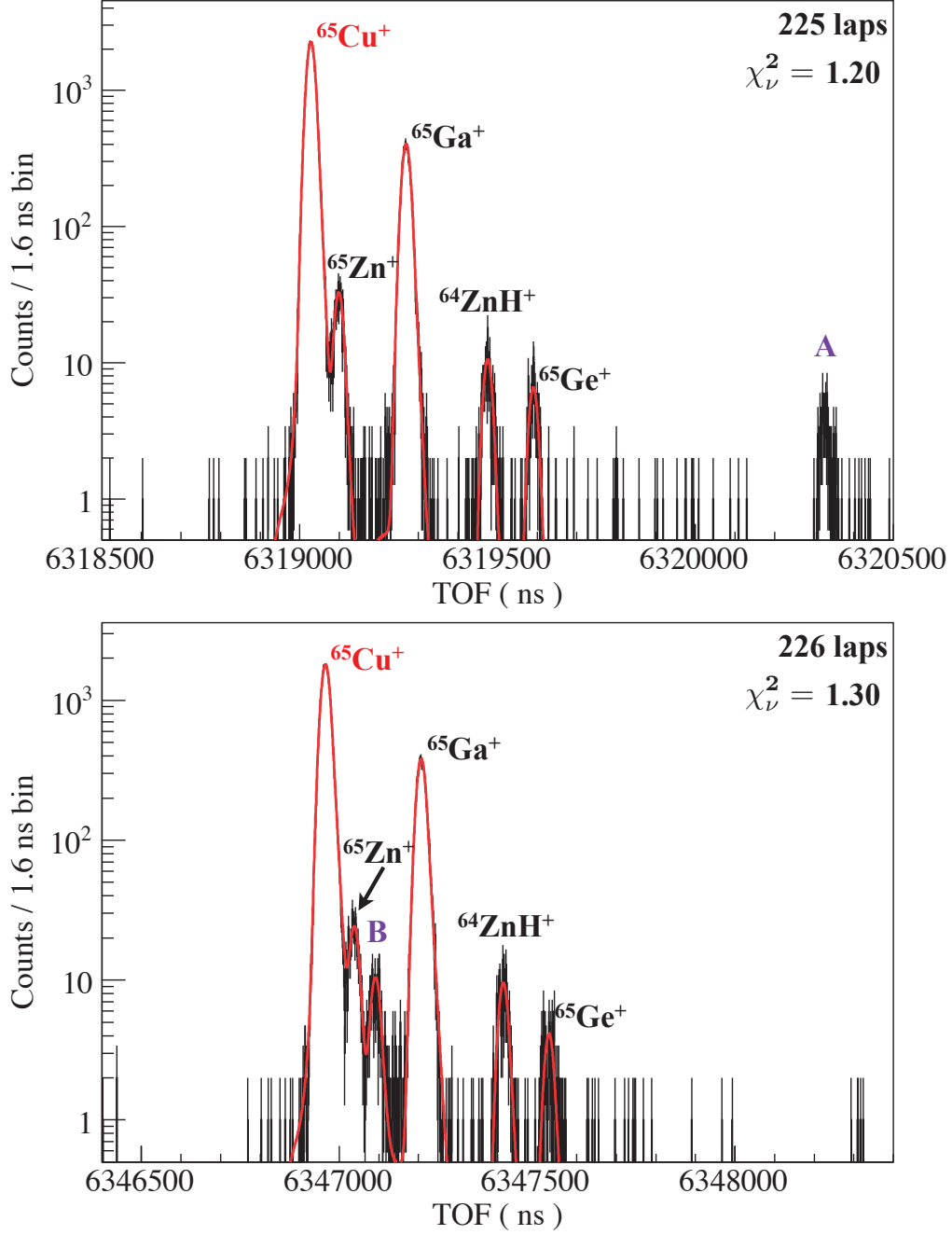


Figure 4.1: Time-of-flight spectra of $A/q = 65$ at 225 and 226 laps. Red lines indicate the fit. The nuclide which is used as the mass reference is indicated by red characters. The peaks labeled “A” and “B” are transient contaminants, making a number of laps different from $A/q = 65$ ions. This can be inferred the apparent movement of the peak between $N_{65}=225$ laps and $N_{65}=226$ laps. Unlabelled peaks in subsequent figures can be presumed to be of similar origin. A reduced χ^2 -value of fit is indicated in below of the number of laps.

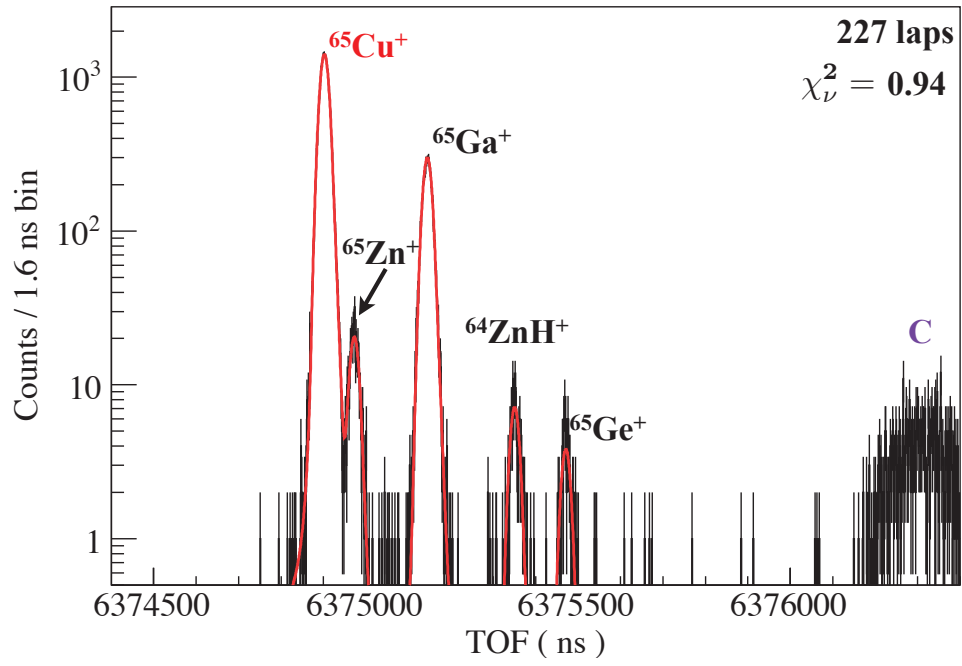


Figure 4.2: Time-of-flight spectra of $A/q = 65$ at 227 laps. Continue of Fig. 4.1. See Fig. 4.1 for details.

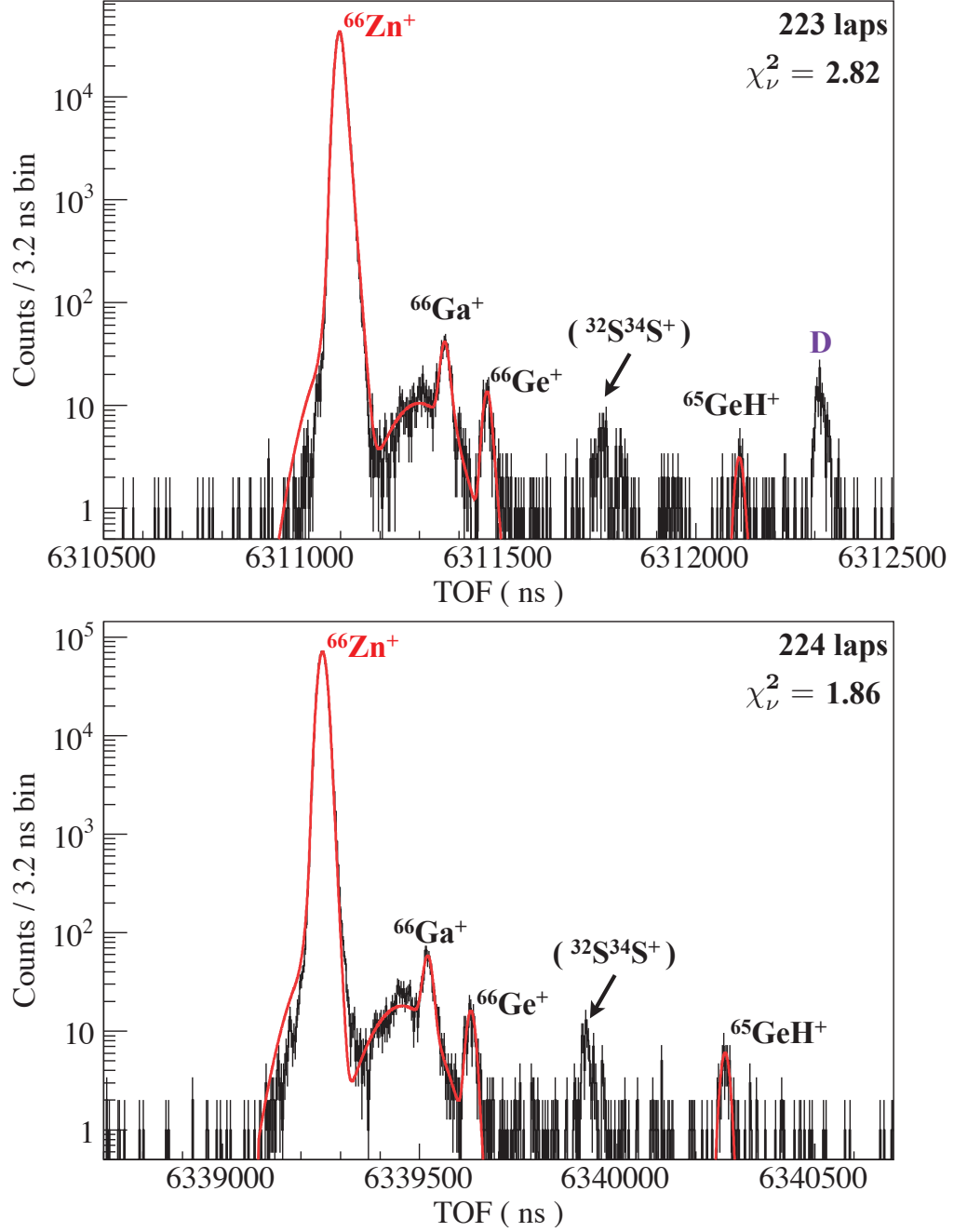


Figure 4.3: Time-of-flight spectra of $A/q = 66$ at 223 and 224 laps. See Fig. 4.1 for details.

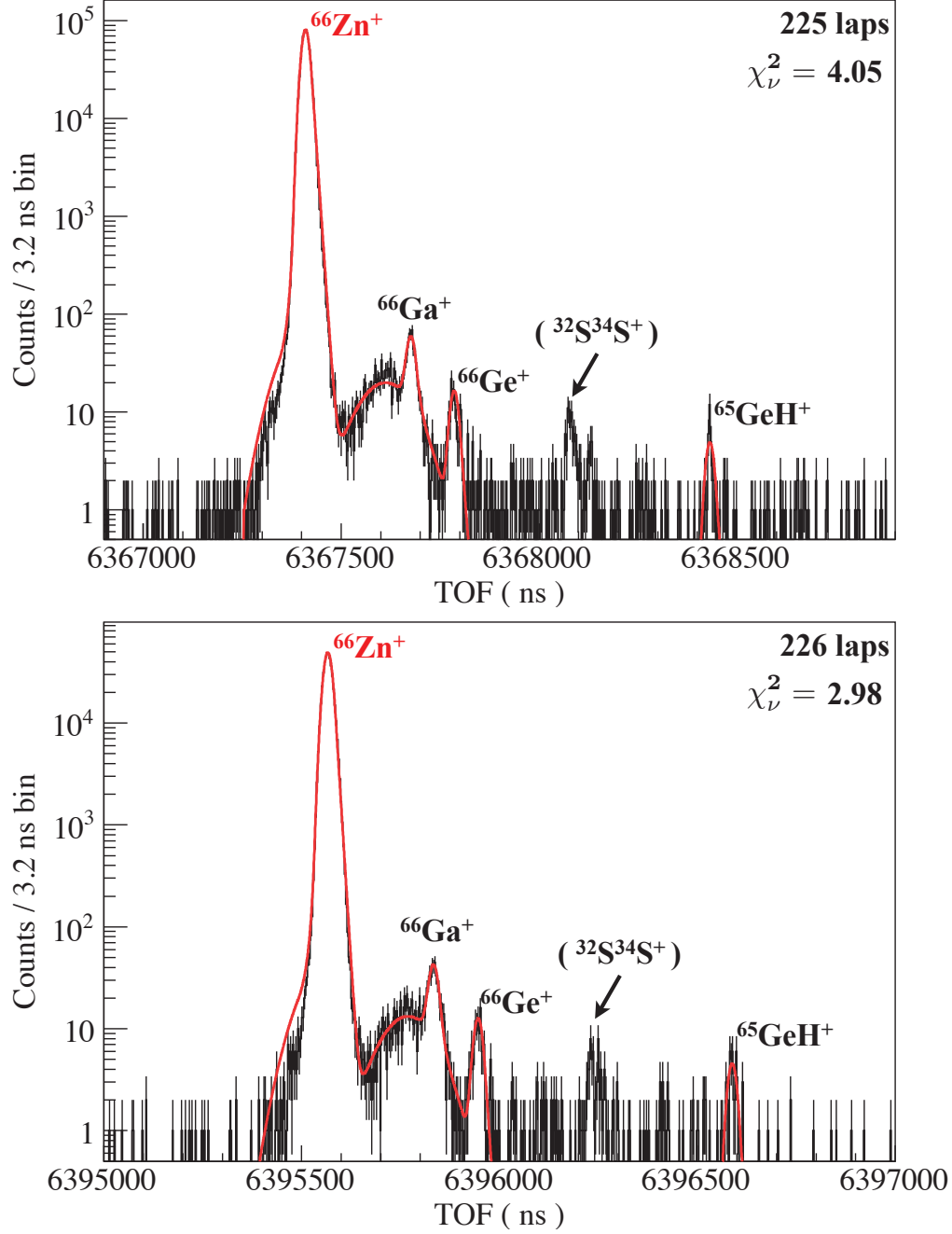


Figure 4.4: Time-of-flight spectra of $A/q = 66$ at 225 and 226 laps. Continue of Fig. 4.3. See Fig. 4.1 for details.

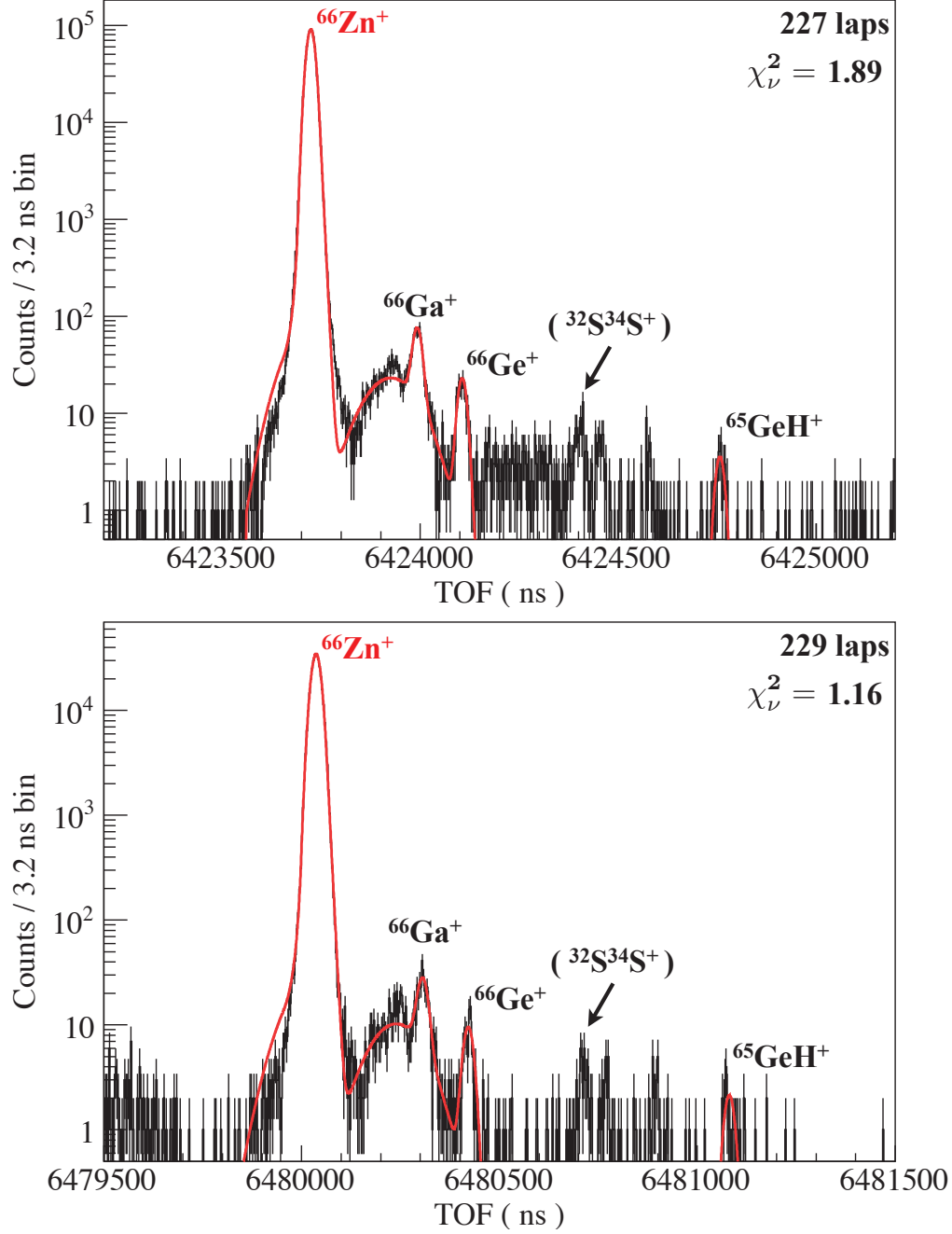


Figure 4.5: Time-of-flight spectra of $A/q = 66$ at 227 and 229 laps. Continue of Fig. 4.4. See Fig. 4.1 for details.

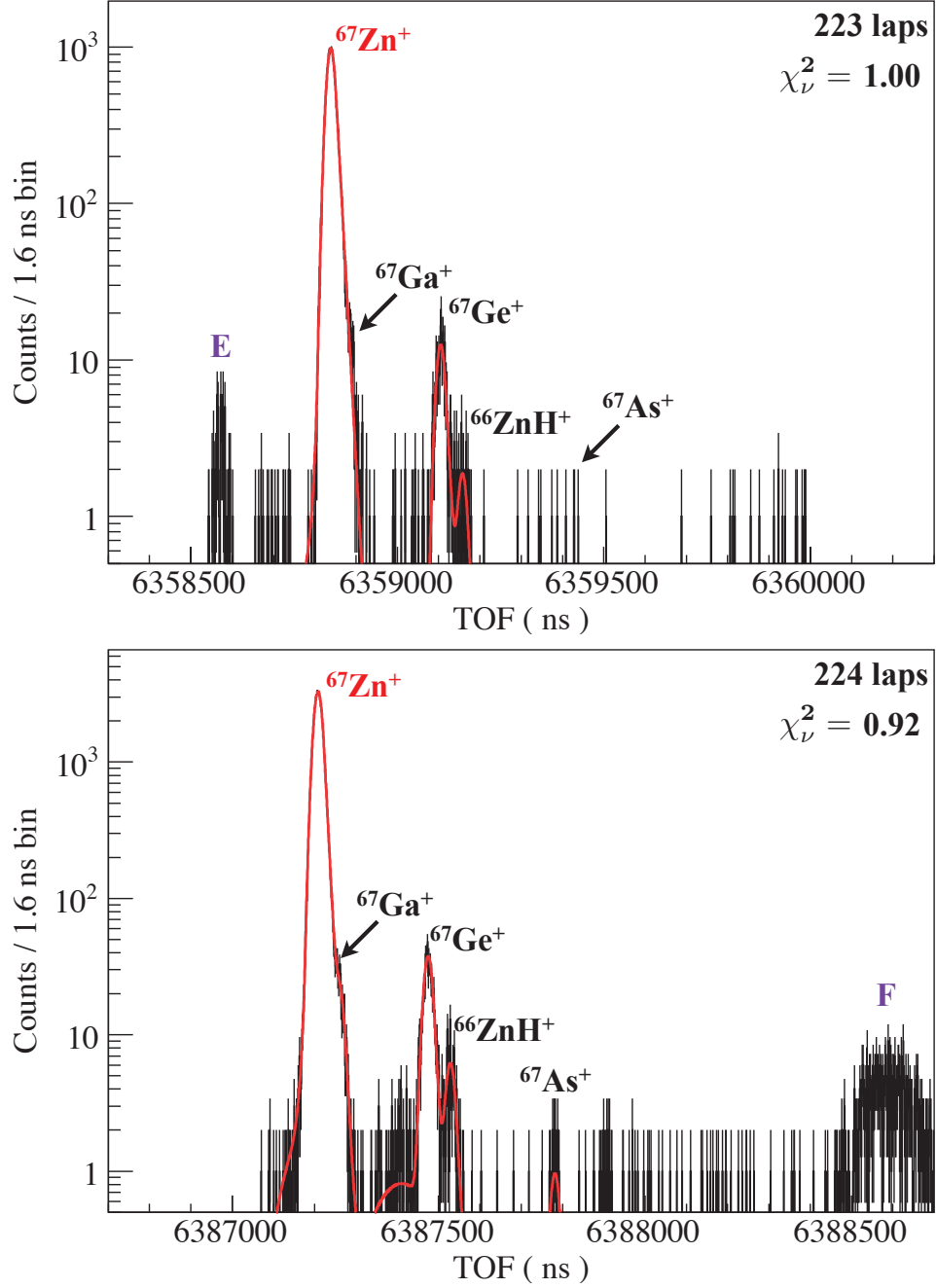


Figure 4.6: Time-of-flight spectra of $A/q = 67$ at 223 and 224 laps. See Fig. 4.1 for details.

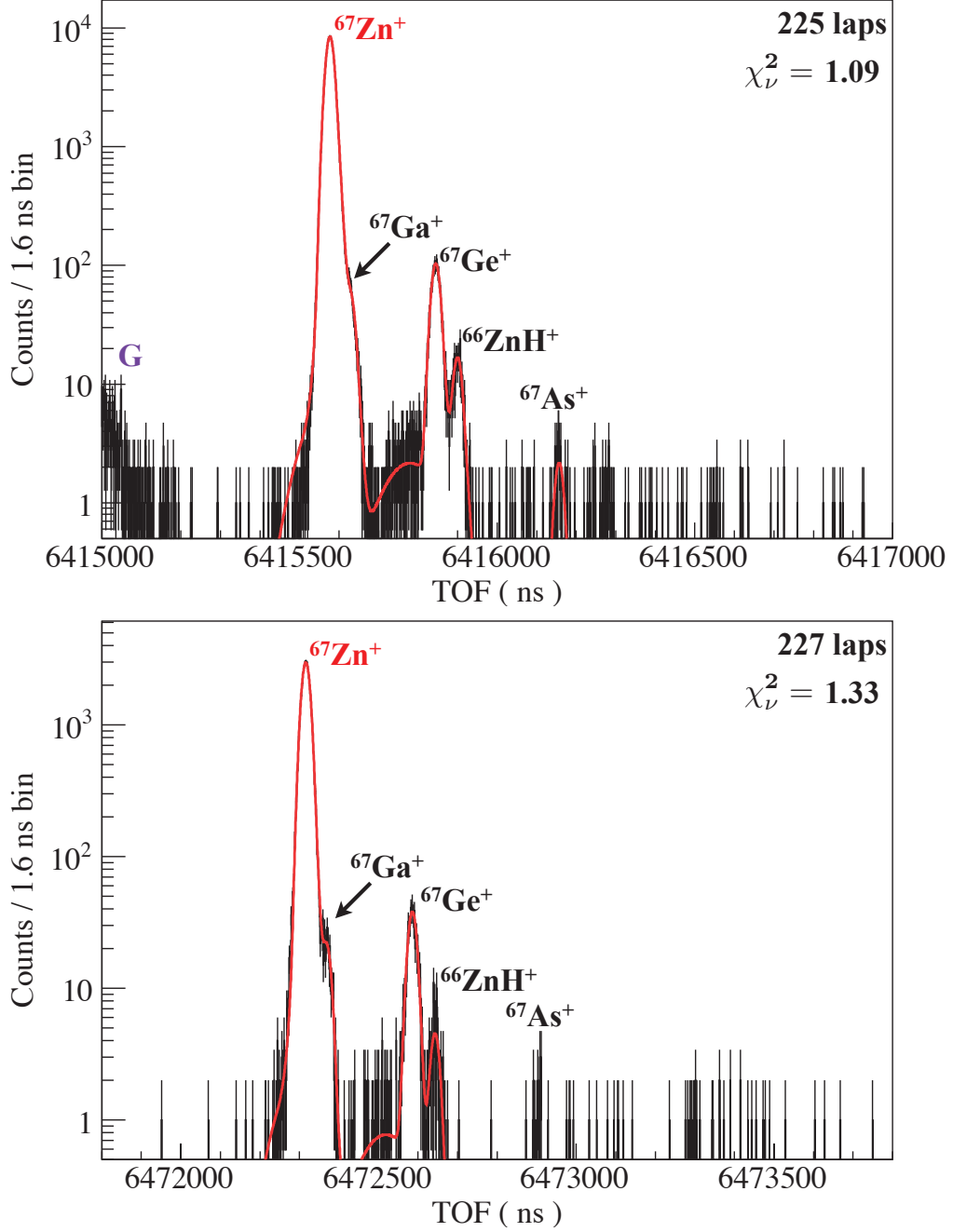


Figure 4.7: Time-of-flight spectra of $A/q = 67$ at 225 and 227 laps. Continue of Fig. 4.6. See Fig. 4.1 for details.

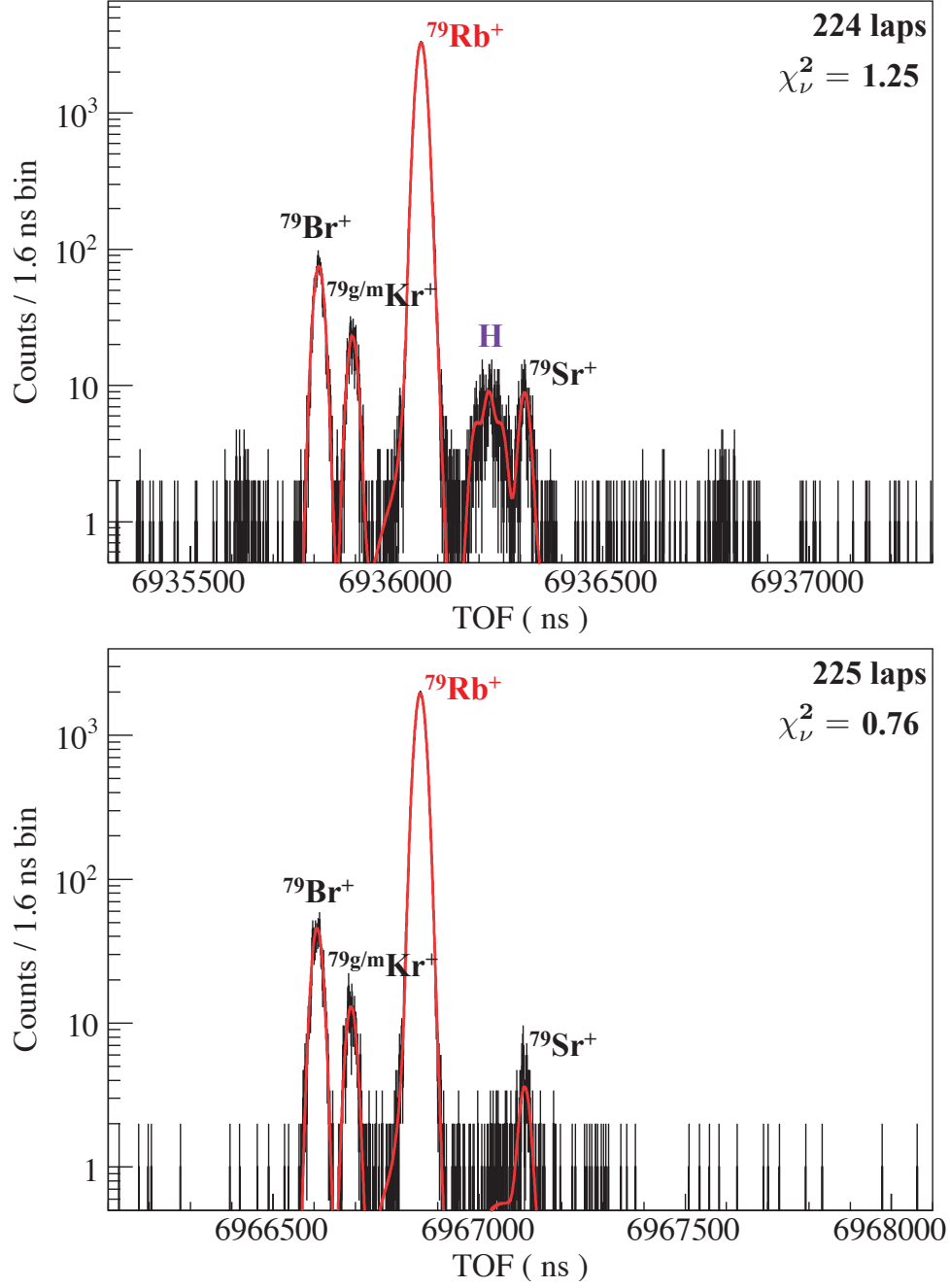


Figure 4.8: Time-of-flight spectra of $A/q = 79$ at 224 and 225 laps. See Fig. 4.1 for details.

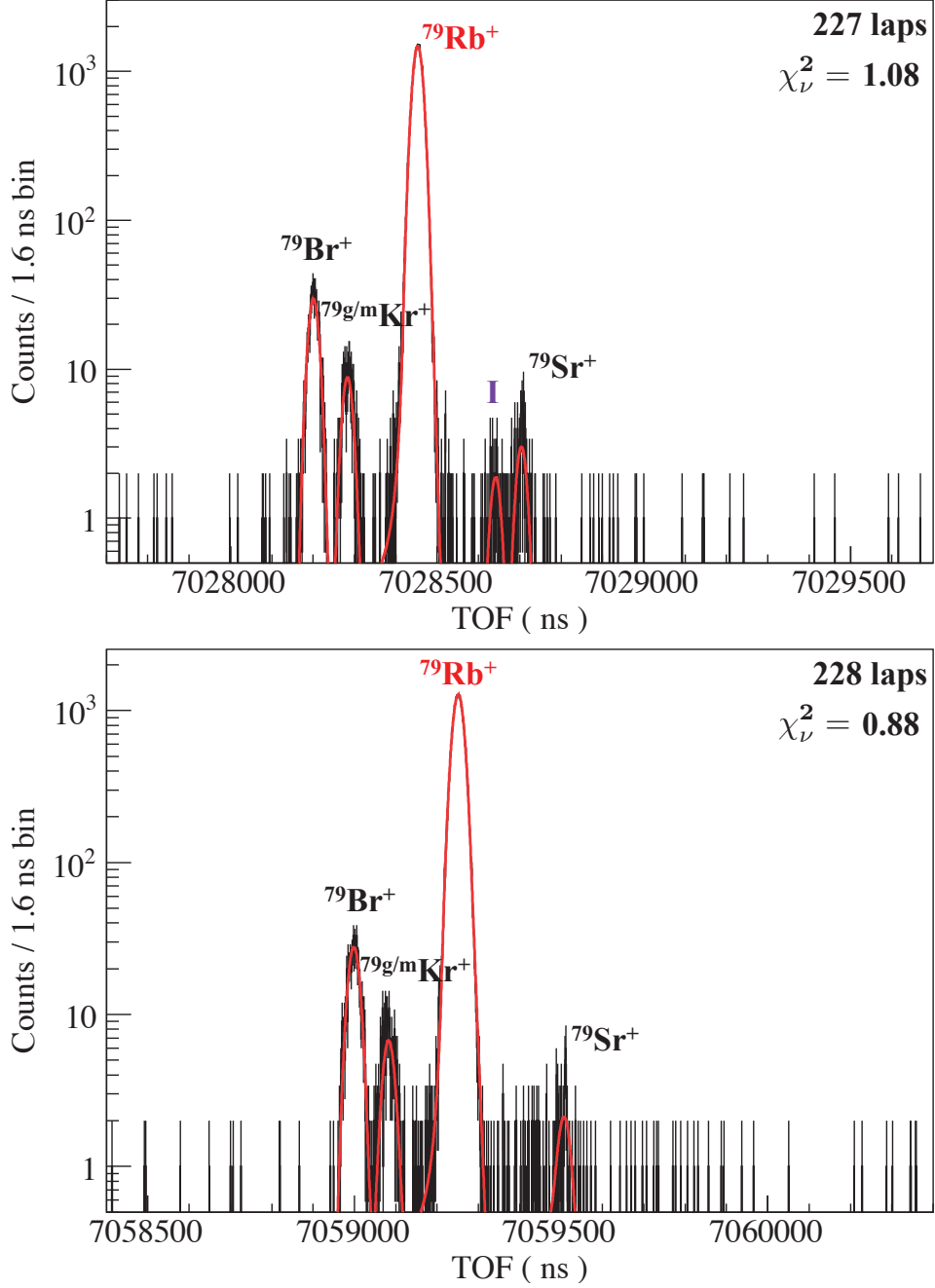


Figure 4.9: Time-of-flight spectra of $A/q = 79$ at 227 and 228 laps. Continue of Fig. 4.8. See Fig. 4.1 for details.

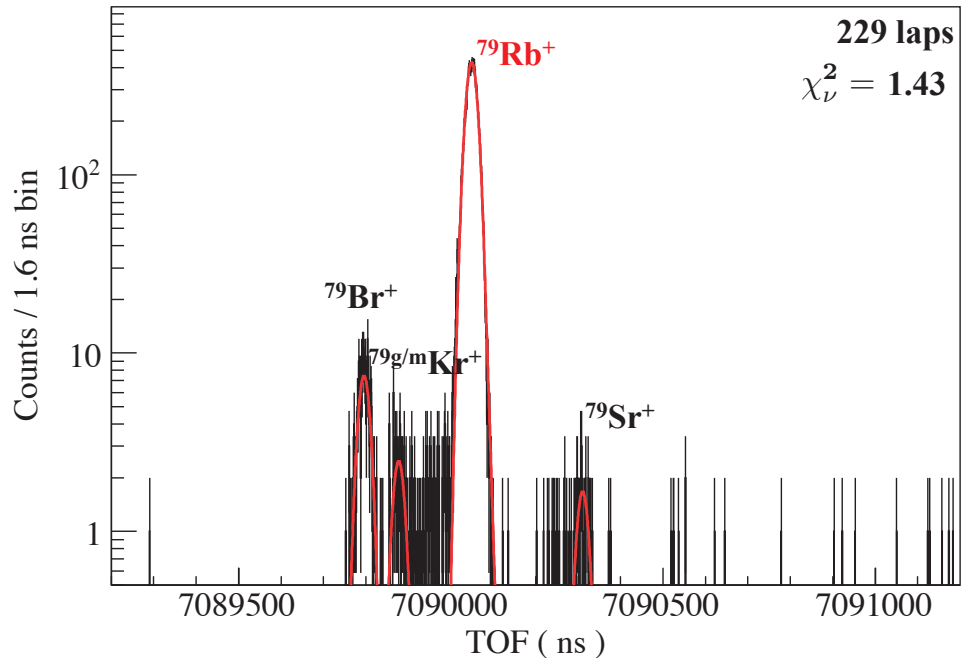


Figure 4.10: Time-of-flight spectra of $A/q = 79$ at 229 laps. Continue of Fig. 4.9. See Fig. 4.1 for details.

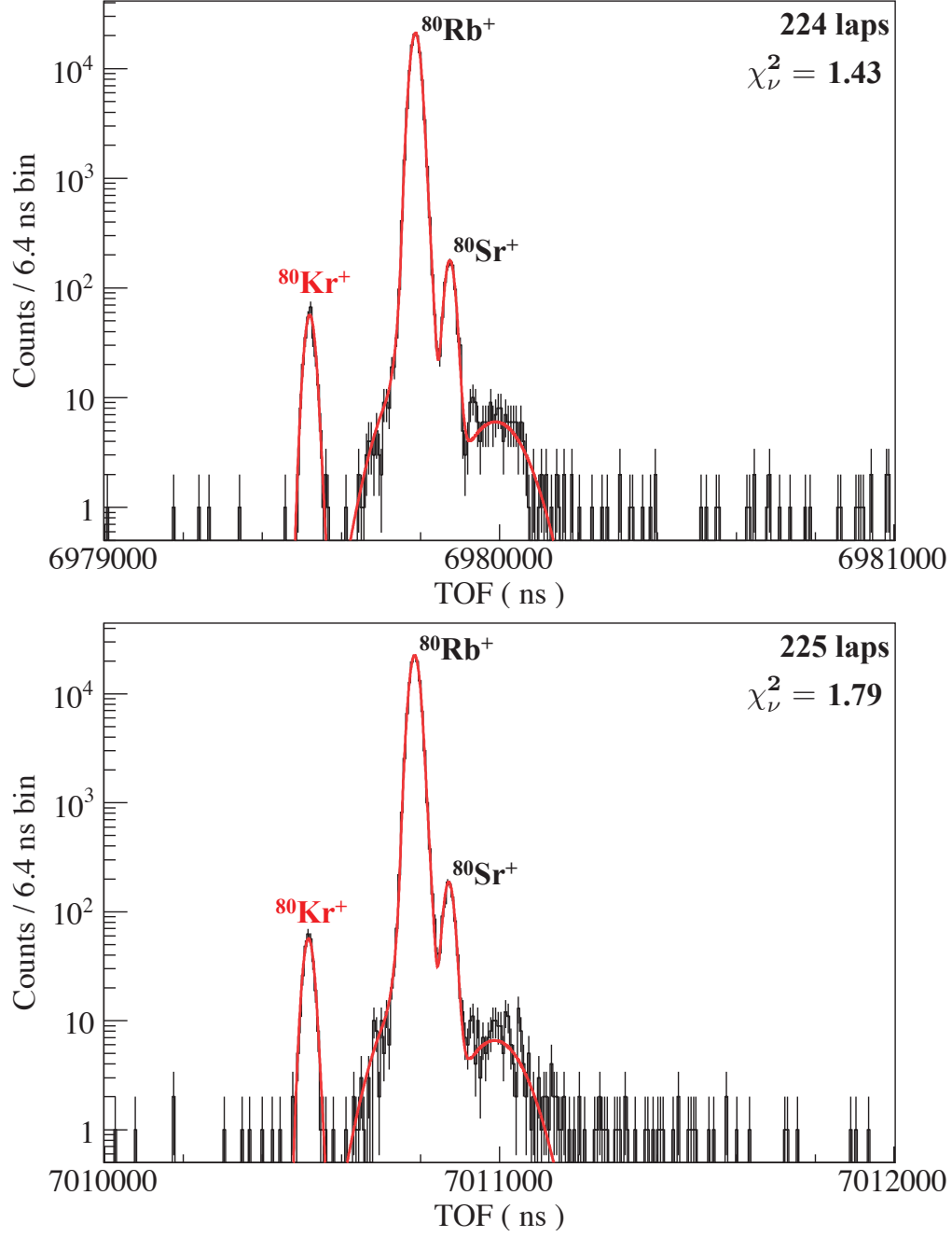


Figure 4.11: Time-of-flight spectra of $A/q = 80$ at 224 and 225 laps. See Fig. 4.1 for details.

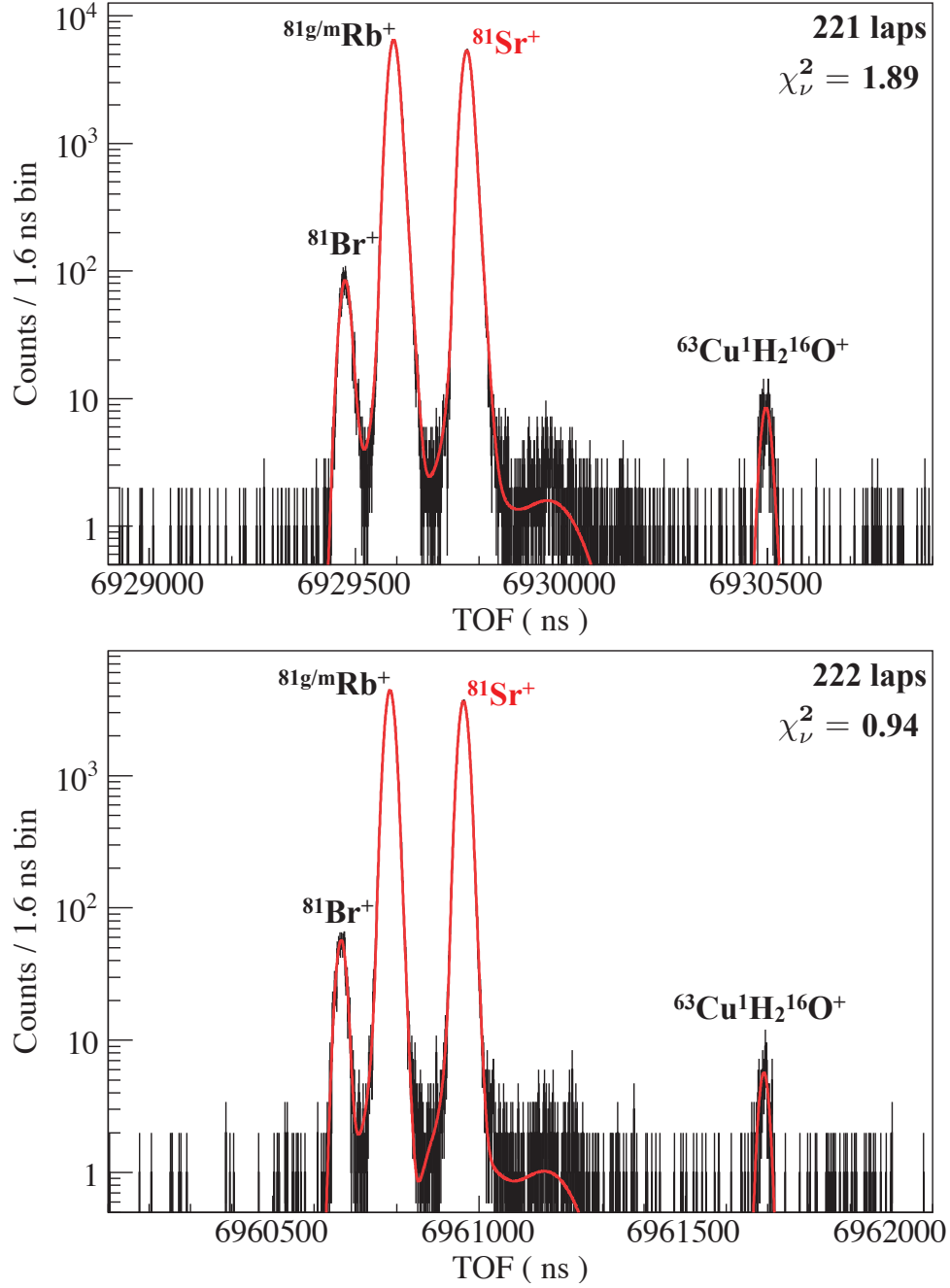


Figure 4.12: Time-of-flight spectra of $A/q = 81$ at 221 and 222 laps. See Fig. 4.1 for details.

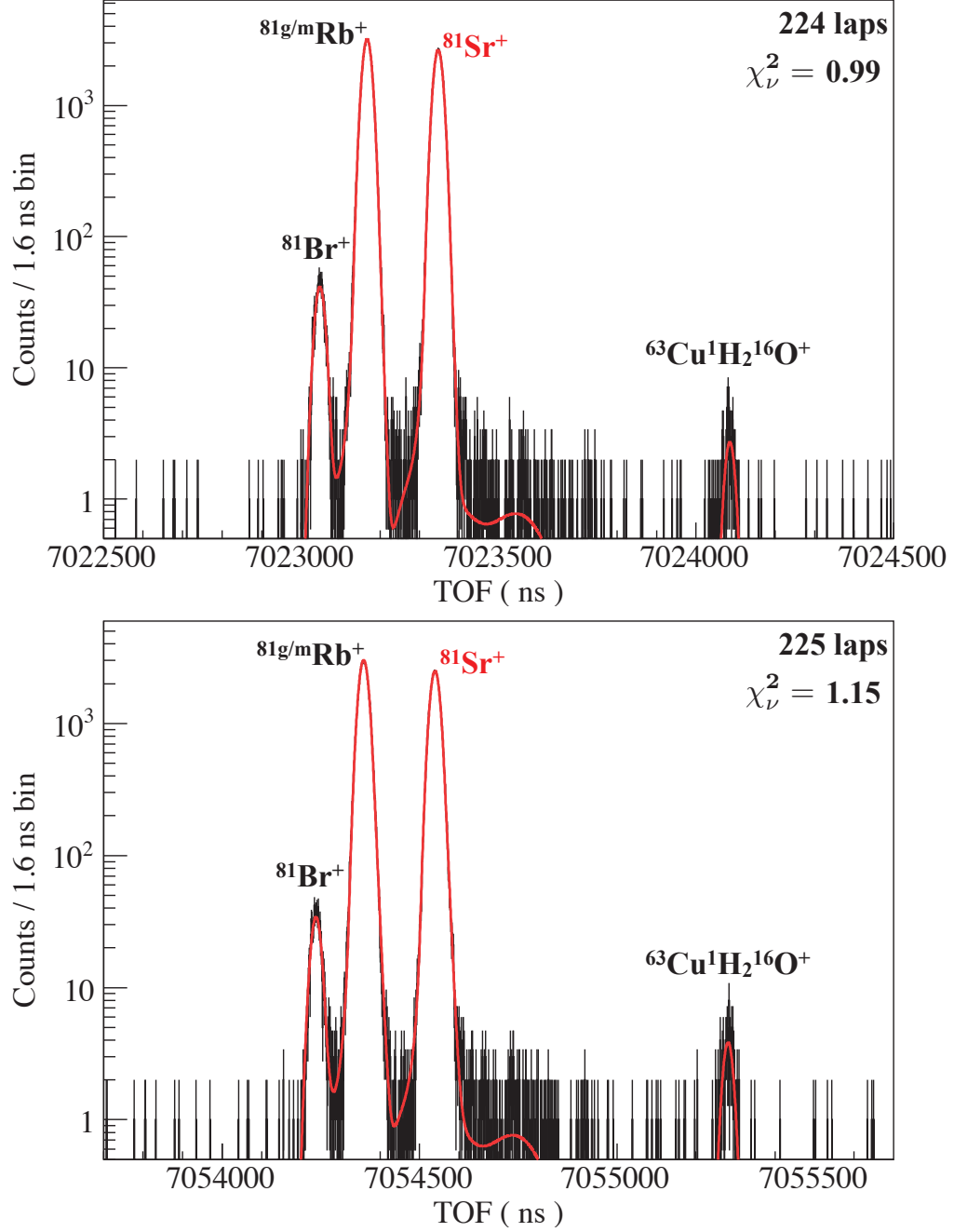


Figure 4.13: Time-of-flight spectra of $A/q = 81$ at 224 and 225 laps. Continue of Fig. 4.12. See Fig. 4.1 for details.

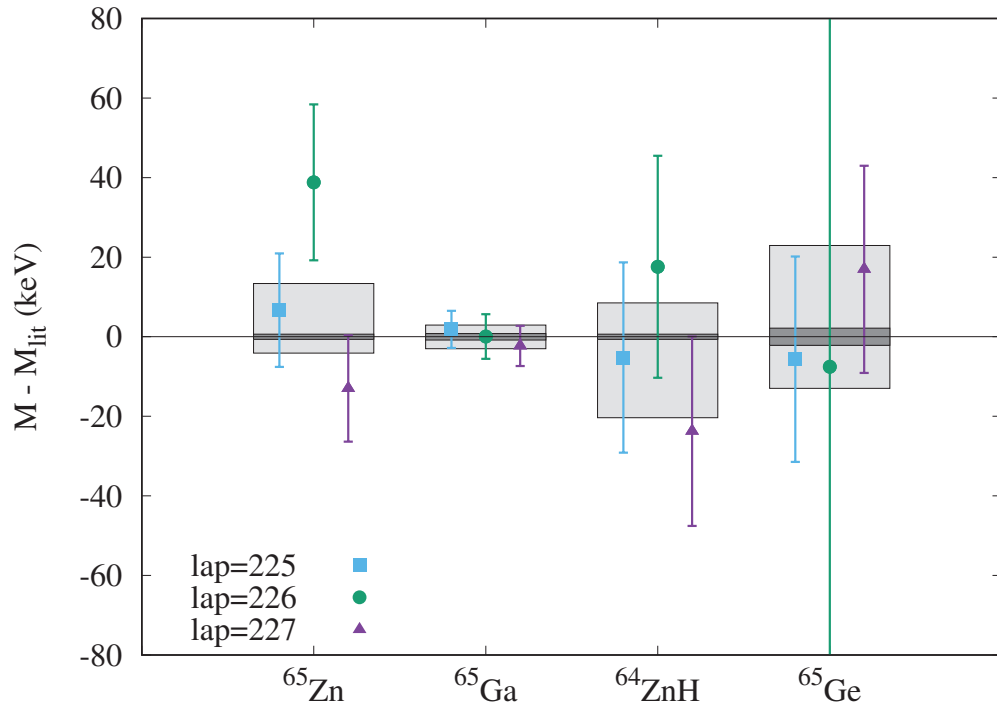


Figure 4.14: Fit results of $A/q = 65$ series. Light-grey band of each species indicates a weighted average of the all measurements and darker-grey band represents error of AME16.

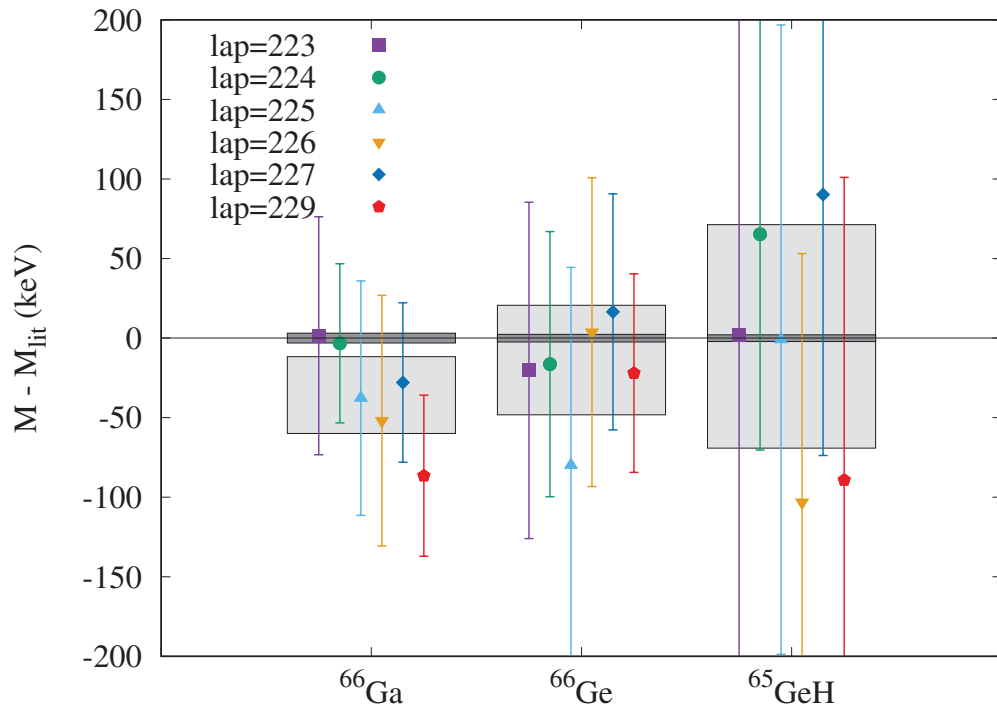


Figure 4.15: Fit results of $A/q = 66$ series. See Fig. 4.14 for details.

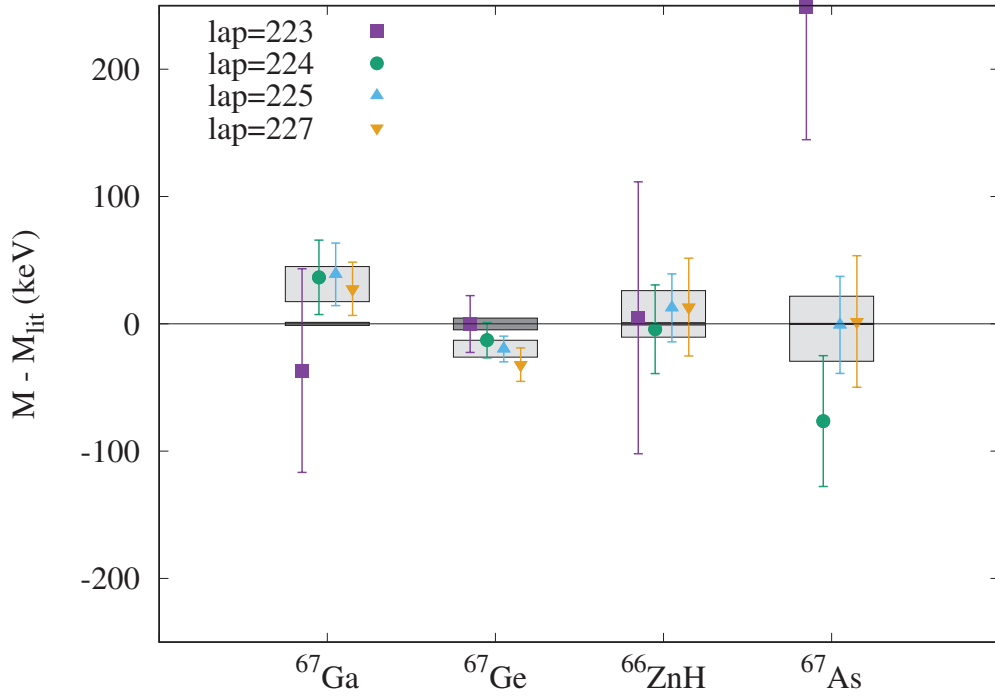


Figure 4.16: Fit results of $A/q = 67$ series. See Fig. 4.14 for details.

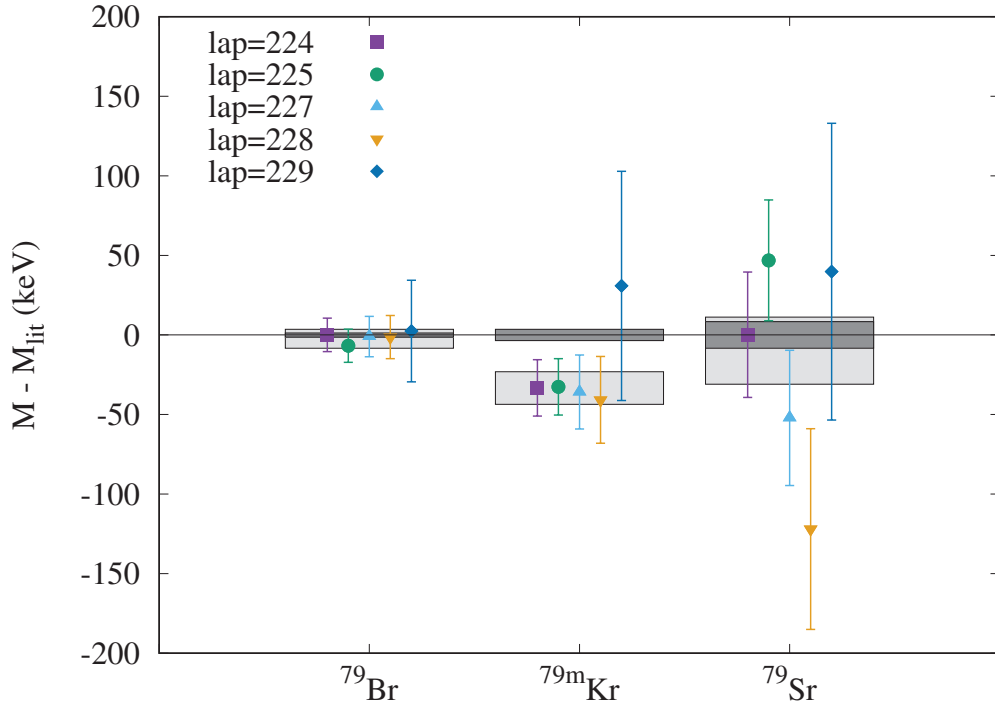


Figure 4.17: Fit results of $A/q = 79$ series. See Fig. 4.14 for details.

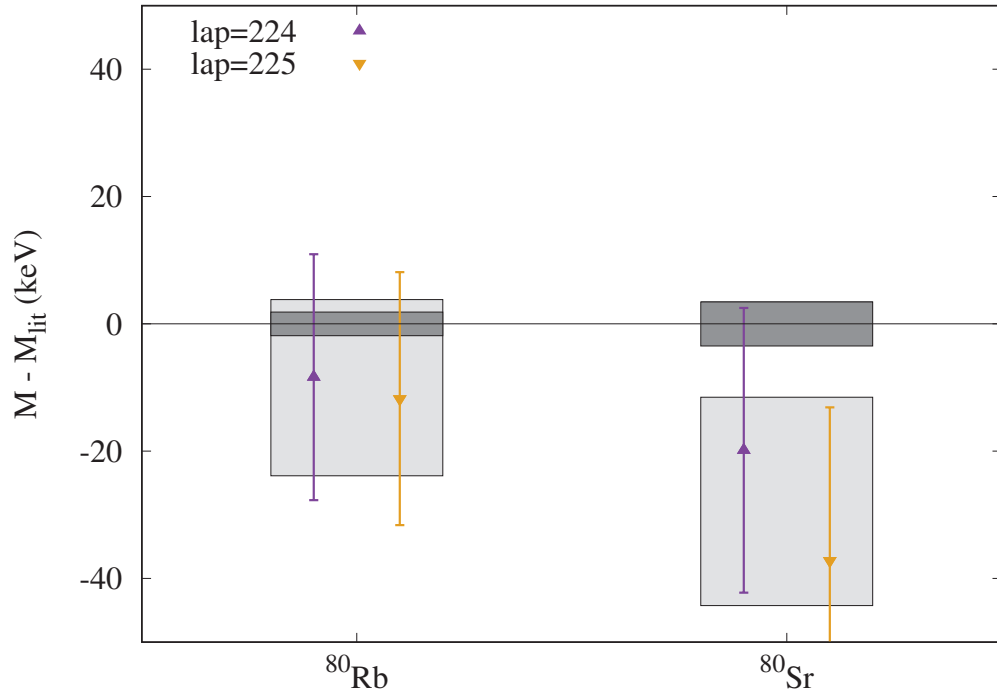


Figure 4.18: Fit results of $A/q = 80$ series. See Fig. 4.14 for details.

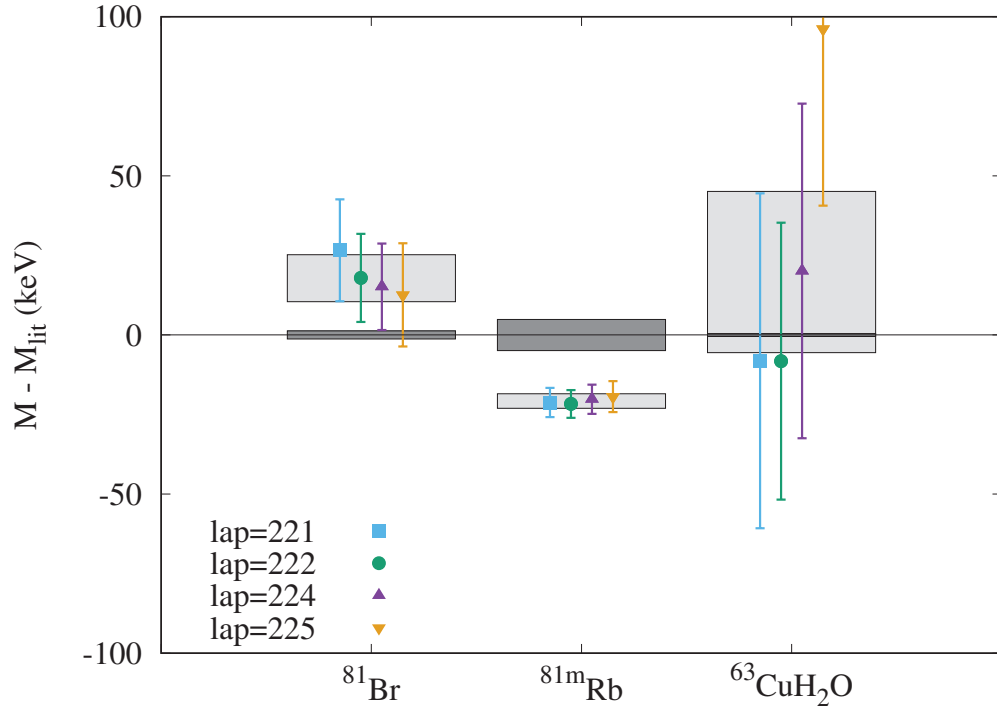


Figure 4.19: Fit results of $A/q = 81$ series. See Fig. 4.14 for details.

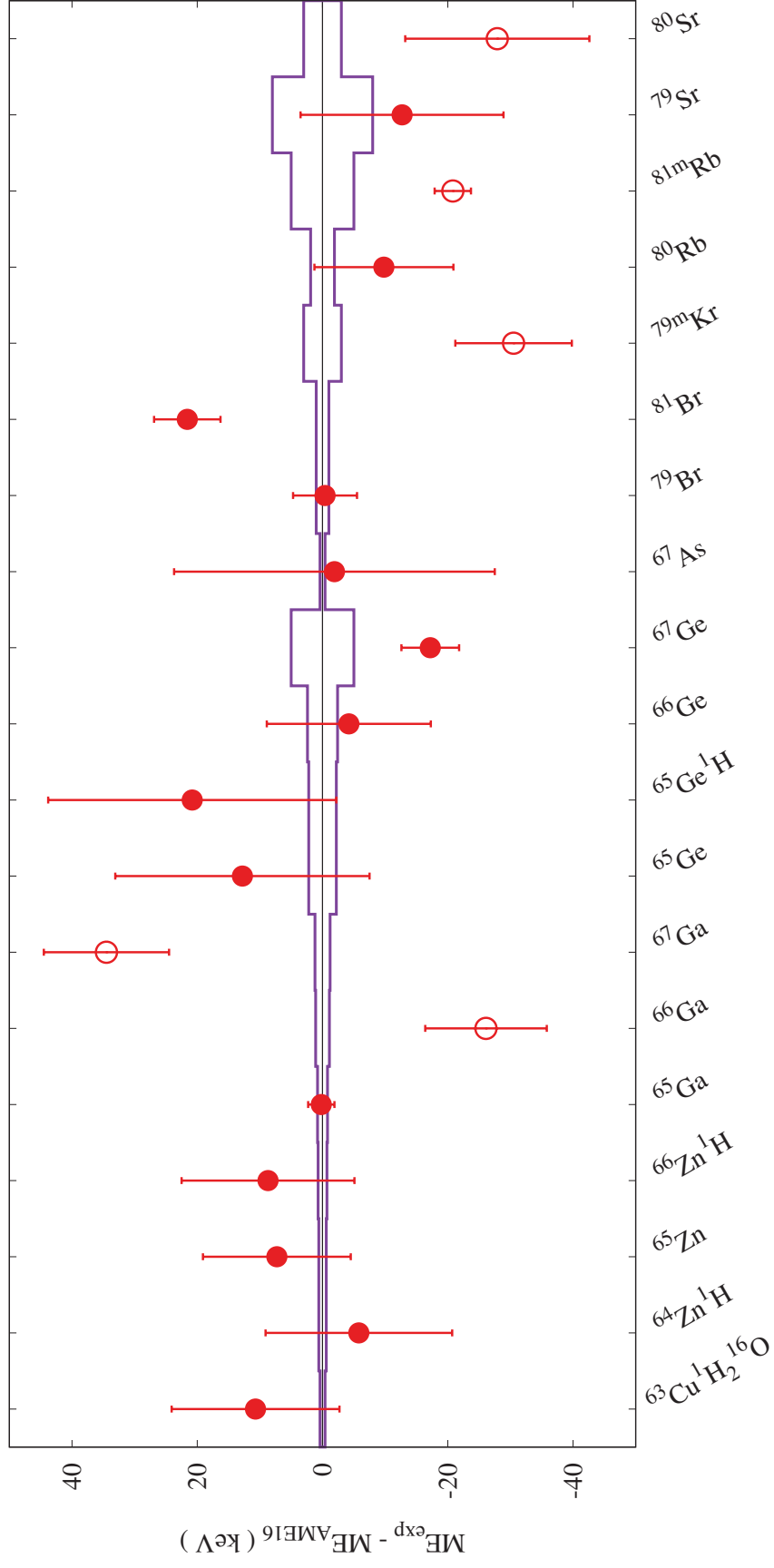


Figure 4.20: Differences between the present measurement results and the AME16 values. Purple lines represent errors of the AME16 values. The open symbols indicate data which do not satisfy the reliability criteria.

Chapter 5

DISCUSSION

In this chapter, we will discuss the details of the results, in particular masses of ^{67}Ge and ^{81}Br , the systematic uncertainties of measurements, and the limitation of mass determination precision. In addition, the overall efficiency of the SHE-mass facility in the present experiment and possible further applications of the SHE-mass facility via the present study are also discussed.

5.1 Mass evaluation of ^{67}Ge and ^{81}Br

In the present study, we find discrepancies with AME16 in the mass values of ^{67}Ge and ^{81}Br . These masses have previously been deduced through indirect measurements and have some ambiguities in themselves. We will discuss the details of the origins of their ambiguities in the following sections.

Mass of ^{67}Ge

In AME16, the mass of ^{67}Ge has been evaluated via the threshold measurements of the $^{64}\text{Zn}(\alpha, n)^{67}\text{Ge}$ reaction. A diagram of the connection to ^{67}Ge from the reference nucleus ^{64}Zn is shown in Fig. 5.1. There are two threshold measurement experiments adopted by

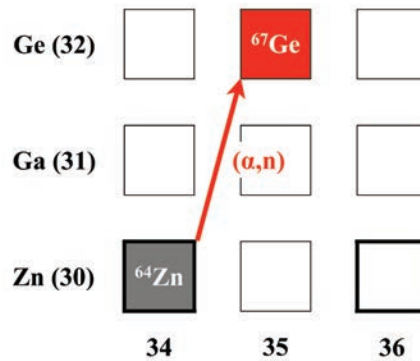
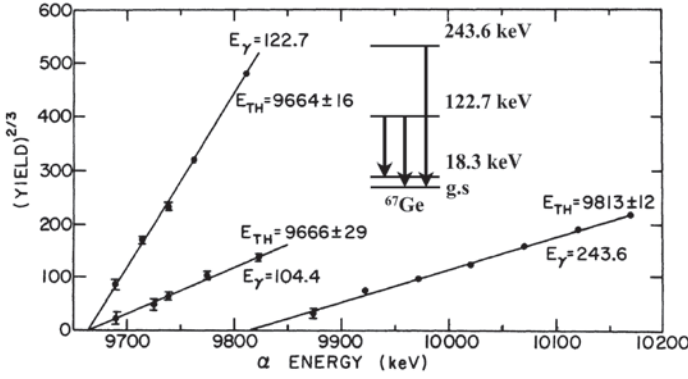


Figure 5.1: Diagram of the connection related to ^{67}Ge . Mass of ^{67}Ge has been evaluated from the mass of ^{64}Zn via a (α, n) reaction. Bold frames represent stable isotopes.

a) Murphy, *et. al.*, 1978



b) Al-Naser, *et. al.*, 1979

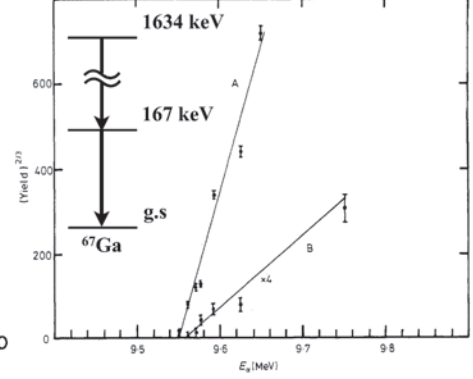


Figure 5.2: Yields of γ -rays from $^{64}\text{Zn}(\alpha, n)^{67}\text{Ge}$ reactions plotted as functions of alpha energy. a) Results of Mu78 [100]. Reaction threshold was deduced using three γ -rays: 104.4 keV, 122.7 keV, and 243.6 keV. b) Results of Al79 [101]. Two γ -rays from ^{67}Ga , 167 keV (“A”) and 1473 keV (“B”), were employed to determine the reaction threshold. In each panel, corresponding decay schemes have been added to the original figures.

AME16: Murphy, *et. al.*, 1978 (Mu78) [100] and Al-Naser, *et. al.*, 1979 (Al79) [101]. In the case of Mu78, induced α -particle energy was varied from 9 MeV up to 12 MeV. The excitation functions of ^{67}Ge were measured for three γ -rays: 104.4 keV, 122.7 keV, and 243.6 keV. The reported excitation functions from Mu78 are shown in “a” of Fig. 5.2. From these data a value of $ME_{\text{Mu78}}(^{67}\text{Ge}) = -62666(12)$ keV was deduced.

In the case of Al79, the excitation function of ^{67}Ge was determined from 167 keV and 1473 keV γ -rays from ^{67}Ga , which is decay daughter of ^{67}Ge . The reported excitation functions are shown in “b” of Fig. 5.2. The mass excess value reported by Al79 was $ME_{\text{Al79}}(^{67}\text{Ge}) = -62659(5)$ keV which is in good agreement with the results of Mu78.

As discussed in Section 1.3.1, reaction threshold measurement is directly connected to the reaction Q -value, but a correction from the Coulomb barrier between projectile and target nuclei are always required. This Coulomb correction can be ignored if a reaction Q -value is sufficiently larger than the Coulomb barrier, which given by

$$V_{\text{Coulmob}} = \frac{Z_1 Z_2 e^2}{r_0 (A_1^{1/3} + A_2^{1/3})} \quad (5.1)$$

where $e^2 = 1.44$ MeV·fm and $r_0 = 1.3$ fm. In the case of $^{64}\text{Zn}(\alpha, n)^{67}\text{Ge}$ reaction, the height of Coulomb barrier can be estimated to be $V_{\text{Coulmob}} = 11.9$ MeV, and is comparable to the reaction Q -value: $Q_{^{64}\text{Zn}(\alpha, n)} = -9.0$ MeV. Under such conditions accurate threshold measurement become difficult as the influence of the Coulomb barrier cannot be ignored.

The neutron yield from (p, n) reactions is given by [107]

$$Y(E_b, \tau_{\text{target}}) = n \int_0^{\tau_{\text{target}}} \int_{E_{th}}^{\infty} \int_{E_{th}}^{\infty} dx dE_i dE \sigma(E) g(E_b, E_i) w(E, E_i, x), \quad (5.2)$$

where $g(E_b, E_i)$ is the energy distribution of the incident beam with average energy E_b and $w(E, E_i, x)$ is the energy distribution accounting for energy spread resulting from energy

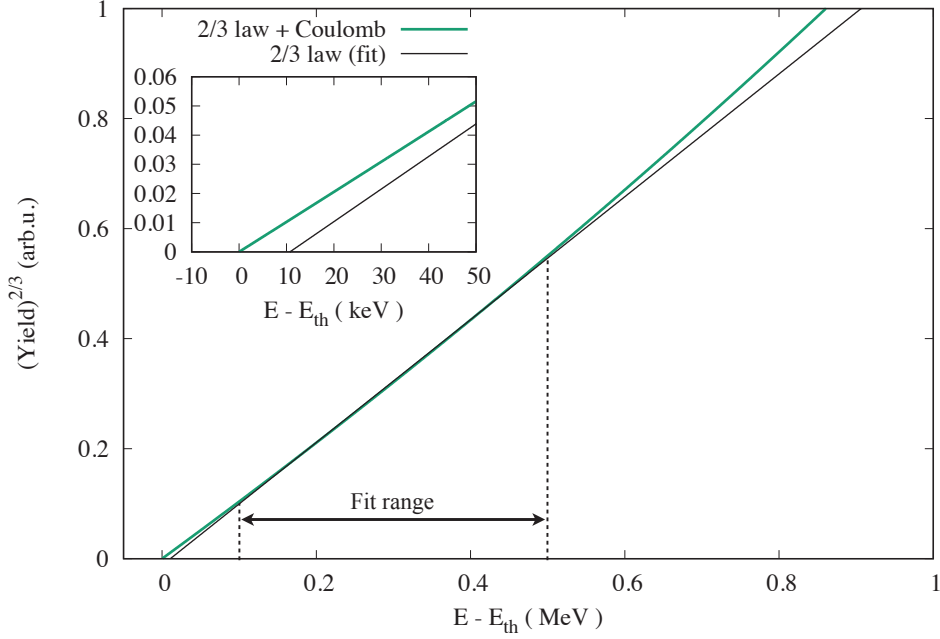


Figure 5.3: Calculated yield curve of $^{64}\text{Zn}(\alpha, n)^{67}\text{Ge}$ reaction. The green line indicates the yield curve accounting for the influence of Coulomb barrier (Eq. 5.4). The black line indicates the fitting result of 2/3 law (Eq. 5.3) to the green line in the range of 0.1 - 0.5 MeV. A top-left panel is an enlarged view near the threshold energy.

loss at a depth x in the target material, and E_{th} is the threshold energy. Neutron emission probability in the case of no resonance near threshold energy is proportional to the velocity of the emitted neutron in the center-of-mass frame (the well-known $1/v$ -law). The if one assumes a mono-energetic beam, a uniform energy loss, and a thick target, Eq. 5.2 can be reduced to

$$Y(\varepsilon) = \text{Const} \times \varepsilon \int_0^\varepsilon dE \frac{1}{\sqrt{E}} \propto \varepsilon^{3/2}, \quad (5.3)$$

where $\varepsilon \equiv E_b - E_{th}$. (Note that $\sigma \propto 1/v \propto 1/\sqrt{E}$.) Therefore plot of $Y^{2/3}$ can be represented by straight lines. However this relation is valid only in the neutron emission reaction with positive Q -value. In the case of the $^{64}\text{Zn}(\alpha, n)^{67}\text{Ge}$ reaction, however, the tunneling probability of induced α -particles must be considered due to the small Q -value as compared with the Coulomb barrier. In order to account for this process, one can modify the neutron yield equation to be

$$Y(\varepsilon) \propto \varepsilon \int_0^\varepsilon dE \frac{1}{\sqrt{E}} \exp(-G(E)), \quad G = \frac{\sqrt{2m_\alpha} Z_\alpha Z_{^{64}\text{Zn}} e^2}{\hbar \sqrt{E + E_{th}}}. \quad (5.4)$$

The results of a calculation of this equation for $^{64}\text{Zn}(\alpha, n)^{67}\text{Ge}$ reactions is plotted in Fig. 5.3 with a green line that can be seen to be slightly curved. The black line in Fig. 5.3 is the result of fitting the green curve with a 2/3 law (Eq. 5.3). The threshold energy

deduced from this fitting is about 10 keV larger than the correct value. The deviantly large threshold energy of $^{64}\text{Zn}(\alpha, n)^{67}\text{Ge}$ reaction gives heavier mass of ^{67}Ge . This fact can explain the result of ^{67}Ge mass in the present study, which has slightly small value ($\Delta m = -17$ keV) than the literature value.

Mass of ^{81}Br

The connection network determining the mass of ^{81}Br , which is slightly more complex than in the case of ^{67}Ge , is shown in Fig. 5.4. The mass anchor point of this network is ^{82}Kr . The mass of ^{81}Br is dominantly determined by the connection of $^{81}\text{Br}(n, \gamma)^{82}\text{Br}(\beta^-)^{82}\text{Kr}$. In general, (n, γ) reactions are an accurate and precise mass determination technique, as discussed in Section 1.3.1. However, we note that the $^{82}\text{Br}(\beta^-)^{82}\text{Kr}$ measurement has some ambiguity. The measurement of the ^{82}Br Q_β -value was performed by employing a β -ray spectrometer (see “a” of Fig. 5.5) [104]. The β -ray spectrometer could collect β -rays with a specific energy, adjusted by changing current in the magnet coils, and could measure the β -ray energy distributions of each γ -ray transition by applying a β - γ coincidence condition. The Q_β -value was deduced using the traditional Kurie plot method by combining the energy information of each γ -ray transition. In this experiment, γ -ray observations were carried out by employing a NaI scintillator. Typical energy resolution of NaI scintillators is around a few percent, which is one order of magnitude worse than the HPGe detectors which are now widely used for γ -ray detection. A comparison between the proposed decay scheme in the β - γ coincidence measurement and the currently adopted excited states of ^{82}Kr are shown in “c” of Fig. 5.5. The proposed excitation energies are smaller than the currently adopted ones on the level of a few tens keV. These lower excitation states lead an underestimate in the mass of ^{81}Br , which supports the mass value proposed in the present study which shows a slightly larger mass, $\Delta m = 21.6$ keV, compared with the literature value.

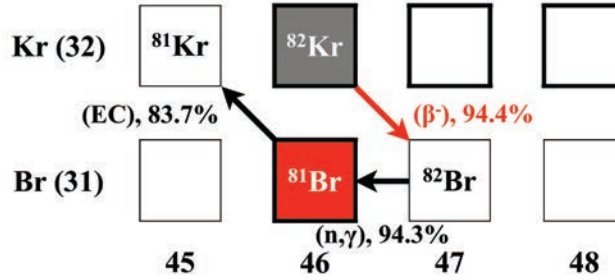


Figure 5.4: Diagram of the connections related to ^{81}Br . The mass of ^{81}Br has been evaluated from the mass of ^{82}Kr via $(\beta^-)^{82}\text{Br}(n, \gamma)$. Percentage of each connection represents its influence on determination the counterpart mass. Bold frames represent stable isotopes.

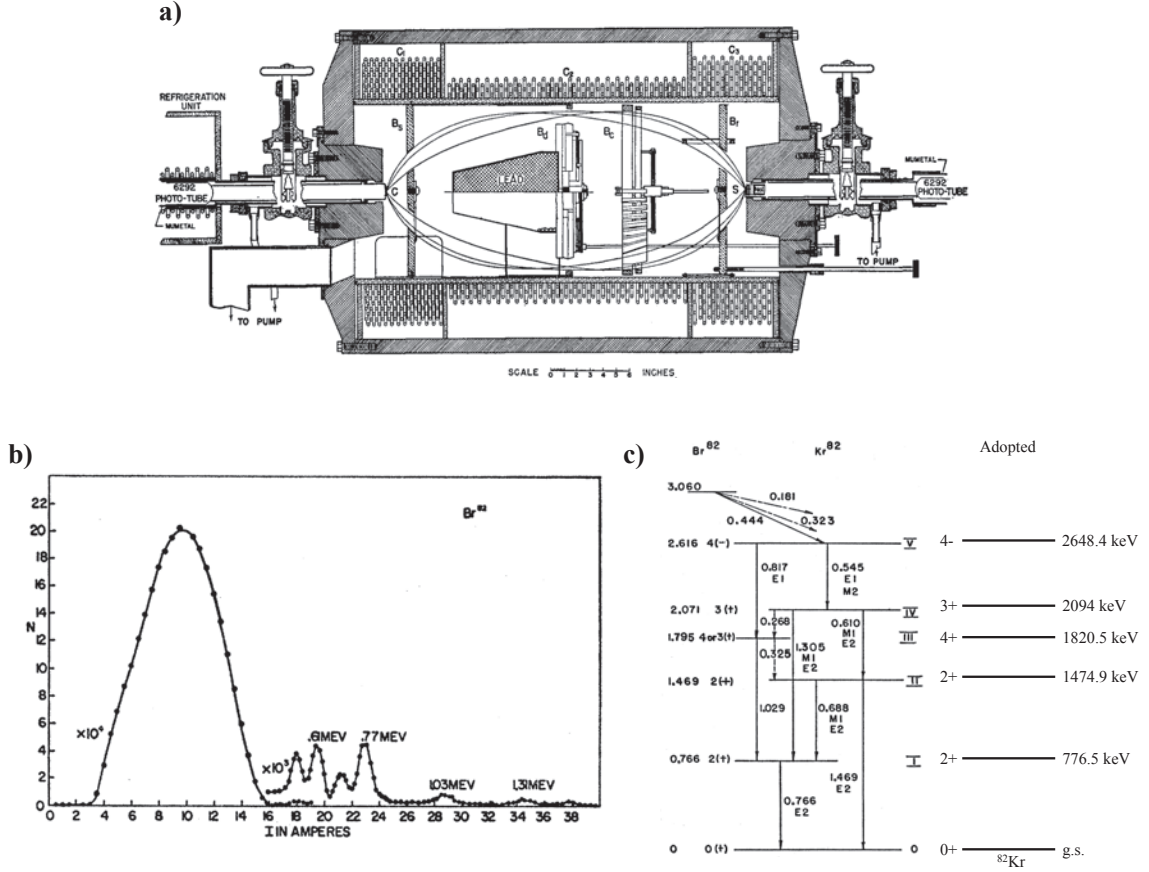


Figure 5.5: Decay measurement of ^{82}Br . a) β -ray spectrometer [108]. “S” represents a source point and the NaI scintillator is installed behind it. “C”, located at the opposite side from “S”, is a β -ray counter consisting of an anthracene crystal. “C₁”, “C₂”, and “C₃” represent coils used to make the U-shaped magnetic field. b) Results of β - γ coincidence measurements [104]. c) Comparison between the proposed decay scheme in [104] and the currently adopted excitation levels of ^{82}Kr [109].

5.2 Measurement precision and its limitation

5.2.1 Position of the present study in the mass measurements

The precisions achieved for the mass measurements in the present study span the range of $\delta m/m = 3.5 \times 10^{-8} - 4.1 \times 10^{-7}$. In several cases the measurements have satisfied the requirement for the rp -process calculations for X-ray bursts, $\delta m < 10$ keV. Total measurement times in the present study are shorter than 30 msec and relative precision reaches the level of $\delta m/m \sim 10^{-8}$. Thus we have proven with unstable isotopes that the MRTOF-MS can, in principle, fill the blank region, located at bottom right of the mass precision versus half-life plot shown in Fig. 5.6.

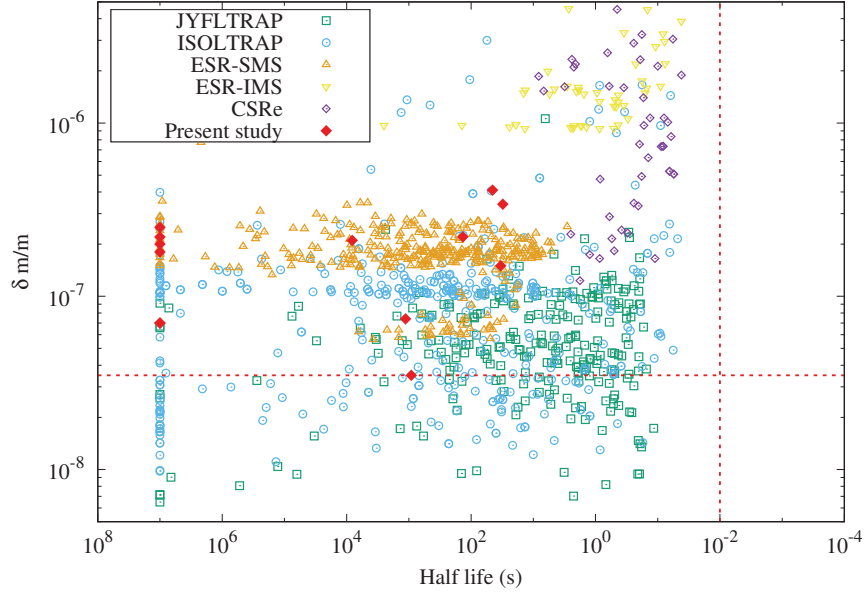


Figure 5.6: Reported relative mass precisions and half-lives. Mass data are taken from [110, 111, 42, 112, 113, 45, 6, 114, 115, 116, 117, 118, 48] and the all half-lives are adopted from NUBASE2016 [119]. Data corresponding to isomeric states are excluded from this figure. If a nuclide is identified as stable isotope or has a half-life which exceeds 1×10^7 sec, its mass precision is plotted at $t_{1/2} = 1 \times 10^7$ sec. The results of the present study are represented by red diamonds. The horizontal red-colored dashed line corresponds to the highest mass precision of the present study, the case of ^{65}Ga , while vertical red line indicates the half-life of ^{219}Ra ($t_{1/2} = 10$ ms) which is the most short lived nuclide have been measured with the SHE-mass facility so far [120].

5.2.2 Systematic error originating from δt_{drift}

In the present study, the single reference method with isobaric reference has been used for determination of the masses. The single reference method can be represented by two different expressions, depending on the choice of parameters:

$$\begin{cases} m_X = \rho^2 m_{\text{ref}} \\ m_X = C_{\text{single}}(t_X - t_0)^2 m_{\text{ref}}, \end{cases} \quad (5.5)$$

where $C_{\text{single}} \equiv 1/(t_{\text{ref}} - t_0)^2$. The first formula, which has the time-of-flight (TOF) ratio ρ as a variable, is adopted in the present study and its systematic error can be estimated by

$$\begin{aligned} (\delta(\rho^2)_{\text{sys}})^2 &= 4\rho^2 \left[\left(\frac{\partial \rho}{\partial t_{\text{drift}}} \right)^2 \delta t_{\text{drift}}^2 + \left(\frac{\partial \rho}{\partial t_0} \right)^2 \delta t_0^2 \right] \\ &\approx 4\rho^2 (\rho - 1)^2 \left(\frac{\delta t_0}{t_r} \right)^2 \left[1 + \left(\frac{\delta t_{\text{drift}}}{t_r} \right)^2 \right] \end{aligned} \quad (5.6)$$

In order to estimate the δt_{drift} term, we assume that the influence of the δt_{drift} can be found to be strongly correlated with t_X and t_{ref} (see Section 3.3). If we introduce the

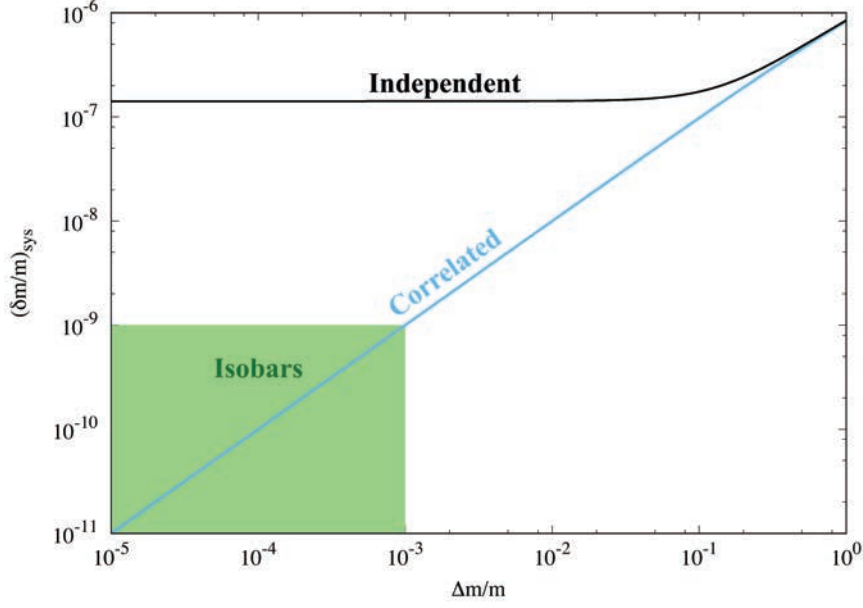


Figure 5.7: The systematic error as a function of relative mass difference. See the texts for details.

variable $\Delta m = m_X - m_{\text{ref}}$, the TOF ratio ρ can be rewritten as a function of Δm : $\rho = \sqrt{1 + \Delta m/m_{\text{ref}}}$. Equation 5.6 is plotted in Fig. 5.7 with label “Correlated”. In this case, the systematic error is dominated by the δt_0 term and could be suppressed down to $(\delta m/m)_{\text{sys}} \leq 10^{-9}$ (green area of Fig. 5.7) by employing isobaric reference.

In the second formula of Eq. 5.5, the two TOF values, t_X and t_{ref} , are treated independently. Then one can calculate the systematic error to be

$$\begin{aligned}
 (\delta(\rho^2)_{\text{sys}})^2 &= 4\rho^2 \left[\left\{ \left(\frac{\partial \rho}{\partial t_X} \right)^2 \left(\frac{dt_X}{dt_{\text{drift}}} \right)^2 + \left(\frac{\partial \rho}{\partial t_r} \right)^2 \left(\frac{dt_r}{dt_{\text{drift}}} \right)^2 \right\} \delta t_{\text{drift}}^2 + \left(\frac{\partial \rho}{\partial t_0} \right)^2 \delta t_0^2 \right] \\
 &\approx 4\rho^2 \left[\left\{ \left(1 + \frac{t_r^2}{(t_r - t_0)^2} \right) \rho^2 + \frac{t_0^2}{(t_r - t_0)^2} \right\} \left(\frac{\delta t_{\text{drift}}}{t_i} \right)^2 + (\rho - 1)^2 \left(\frac{\delta t_0}{t_r} \right)^2 \right] \\
 &\approx 4\rho^2 \left[2 \left(\frac{\delta t_{\text{drift}}}{t_r} \right)^2 + (\rho - 1)^2 \left(\frac{\delta t_0}{t_r} \right)^2 \right]. \tag{5.7}
 \end{aligned}$$

The result of calculating this equation is also plotted in Fig. 5.7 with label “Independent”. In this case, the δt_{drift} term is the dominant component and the systematic error cannot be reduced to the level of $(\delta m/m)_{\text{sys}} \sim 10^{-8}$. Therefore, in order to achieve high precision results, the reference and analyte data should not be treated independently in the analysis procedure.

5.2.3 Systematic error originating from binning

The highest precision achieved among the present measurements is $\delta m = 2.1$ keV in the case of ^{65}Ga . In this case, the main contribution to the error is a fitting error $\delta \rho_{\text{fit}}$. The error due to the mass uncertainty of the reference nuclei ^{65}Cu has been evaluated to be 0.6 keV in

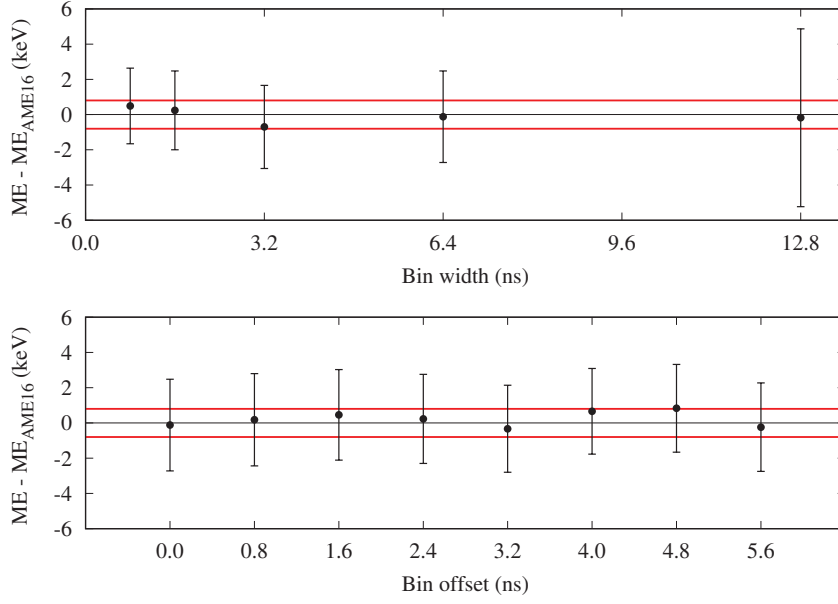


Figure 5.8: Fit parameter dependencies for ^{65}Ga mass excess value. Upper (lower) panel shows bin width (center offset) dependence of ^{65}Ga mass excess value. Red lines indicates the mass uncertainty of ^{65}Ga mass value in AME16. The bin width was chosen to be 6.4 ns in bin offset analysis.

AME16. We assume that further reduction of the fitting errors might be possible if higher statistics data are available. In the situation where the fit error becomes negligibly small, the main contribution to the error budget would be systematic uncertainties originating from the external degrees of freedom in the fit process, *e.g.*, bin width and bin center choice. This bias has been studied with ^{65}Ga data and the results are shown in Fig 5.8. Changing the bin width may have an influence on the results, but it would be even smaller than the AME16 uncertainty in the ^{65}Ga mass value, which can be seen in the upper panel of Fig 5.8. As with the bin width investigation, the choice of bin center also has an affect on the fitting results which is below the level of the nominal fitting uncertainty (see lower panel of Fig 5.8). Standard deviations of bin width and bin offset analysis are $\sigma_{\text{width}} = 0.49$ keV and $\sigma_{\text{offset}} = 0.42$ keV, respectively, and then systematic uncertainty from binning is evaluated to be $\delta m = 0.64$ keV corresponding to $\delta m/m = 1.1 \times 10^{-8}$. Therefore this value is suggested as the precision limit of our MRTOF-MS with isobaric referencing.

5.3 Overall efficiency in the present measurement

Figure 5.9 shows the theoretical production cross-sections of $^{\text{nat}}\text{S}(^{36}\text{Ar}, \text{X})$ reactions in the present measurement setting. The LisFus code [84] was used to calculate these values. In the present study it was possible to access nuclides with cross-sections slightly less than one millibarn. The desired nuclides, however, are predicted to have cross-sections that are one to three orders of magnitude smaller than those measured in the present study (see Fig. 5.9).

The total efficiency of the SHE-mass facility in the present measurements could be

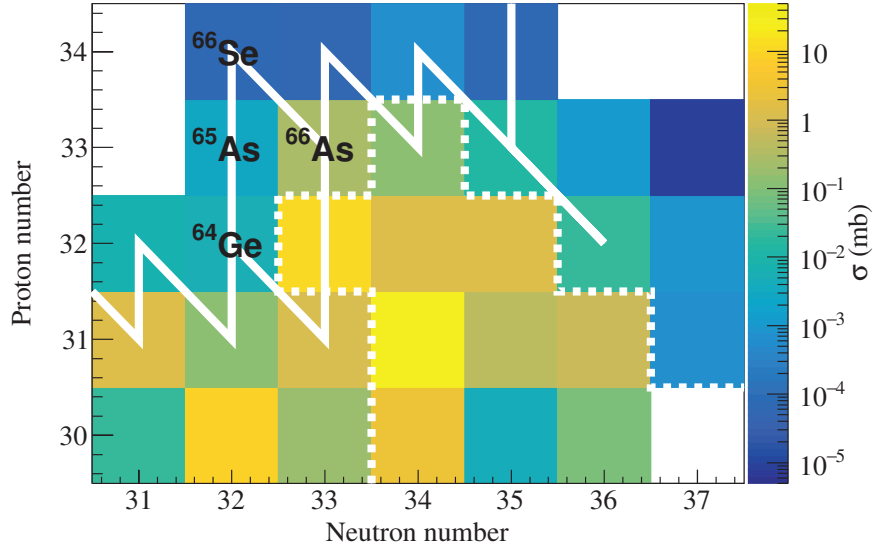


Figure 5.9: Predicted production cross-sections of the fusion-evaporation reaction ${}^{\text{nat}}\text{S}({}^{36}\text{Ar},\text{X})$. The white dotted line shows the boundary of nuclides whose masses were measured in the present study. The bold white line represents the rp -process pathway branches that have more than 10% fractional mass flow [5].

estimated by counting the number of ${}^{80}\text{Rb}$ events in both the β -activity counter and the MRTOF-MS. The intensity of ${}^{80}\text{Rb}$ ions at the GARIS-II focal plane was estimated from β -activity counting rate, combined with GEANT4-based simulations for the estimation of the detection efficiency. This allowed us to determine an incoming ${}^{80}\text{Rb}$ rate of 1×10^6 cps \cdot pμA $^{-1}$ assuming detected β -decay events were dominated by ${}^{80}\text{Rb}$ events and the evaporation residues have uniform distribution at the GARIS-II focal plane. The counting rate at the MRTOF-MS was 4×10^2 cps \cdot pμA $^{-1}$. The total efficiency of the SHE-mass facility for the present measurements was estimated to be $\sim 0.03\%$.

In the present series of measurements, only the singly-charged ions have been studied in the MRTOF-MS spectra. A recent cryogenic gas-cell (CGC) study suggests that most elements would be extracted as doubly-charged ions [121]. This implies that the singly-charged state could be a very minor component among all ionization states in the CGC and provides room for great improvement in the total efficiency. In the case of super-heavy element mass measurements at the SHE-mass facility, ions were extracted as doubly-charged ions and the total efficiencies reached the few percent level [122], which is roughly one hundred times higher than the present value. This improved total efficiency could allow access to nuclides with microbarn, or even sub-microbarn, production cross sections. The SHE-mass facility can be used not only for the study of super-heavy elements but also for the intermediate-mass proton-rich nuclides, which are crucial to the rp -process.

5.4 Further applications of the SHE-mass facility

5.4.1 Vicinity of ^{100}Sn

The shape of later tail part in the X-ray burst light curve is governed by how the reaction flow proceeds in the end-point region of the rp -process. By the one-zone simulations of Schatz and his collaborators, it is shown that the rp -process reaction flow is terminated in a closed SnSbTe-cycle due to the neutron-deficient Te isotopes having strong (γ, α) branches [5]. The rp -process path around this end-point region are shown in Fig.1.1. In the region shown in Fig.5.10, most nuclear masses on the rp -process path have not been measured with sufficient precision for rp -process calculations to be performed with negligible uncertainties from the masses, a requisite for performing meaningful comparisons between the XRB models. The ^{98}Cd has a longer half-life, $t_{1/2} = 9.2$ s, among the nuclei on the rp -process path in this region, and it can be expected that the effective lifetime of ^{98}Cd has significant effect to the rp -process reaction flow. The Q-value sensitive study also shows $^{98}\text{Cd}(p, \gamma)^{99}\text{In}$ has significant impact to the rp -process calculations [3]. Then by performing the precision mass measurements of end-point region centering the ^{98}Cd , we also could a set strong constraint to the theoretical model of X-ray bursts.

To produce the neutron-deficient nuclei in the rp -process end-point region, the fusion evaporation reactions between the iron group elements are preferable. Production cross-

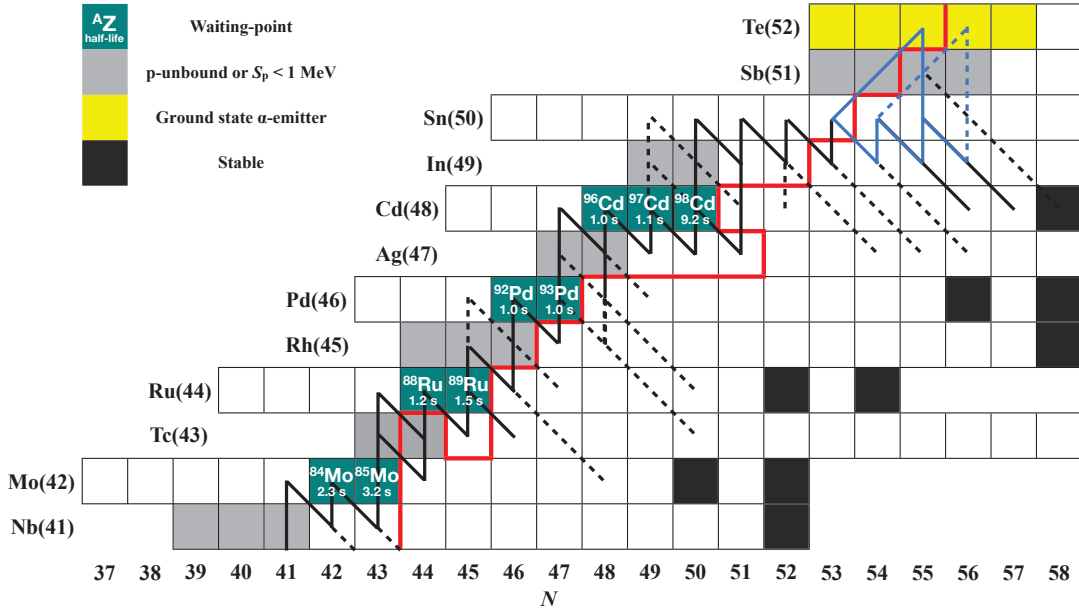


Figure 5.10: The rp -process path in the type I X-ray bursts for the end-point region. The bold lines indicate the reaction flows of more than 10% and the bold dashed line indicate reaction flows of 1% - 10%, respectively, and blue solid and dashed lines represent the SnSbTe-cycle. The bold red line indicates the boundary of that masses have been measured with uncertainties less than 10 keV, which is requirement of theoretical calculation for X-ray burst. The rp -process path is adopted from [5].

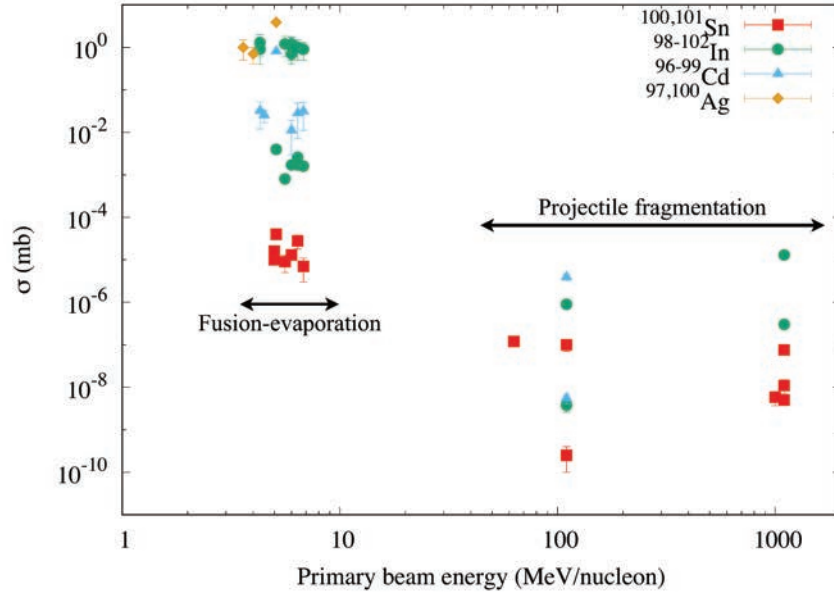


Figure 5.11: Experimental production cross section of proton-rich Ag to Sn isotopes. The experimental data of production cross-section are taken from [123, 124, 125, 126, 127, 128, 129, 130, 131, 132]

section measurements of interesting nuclei have been performed with different combinations such as $^{58}\text{Ni}+^{58}\text{Ni}$ [123], $^{50}\text{Cr}+^{58}\text{Ni}$ [123, 124, 125, 126], and $^{46}\text{Ti}+^{58}\text{Ni}$ [127, 128], and their results summarized in Fig 5.11 with the experimental data of projectile fragmentation. Production cross-sections of the fusion-evaporation reactions are distributed in the range of 10^1 to 10^{-5} mb. In the case of projectile fragmentations, targets thicker than the three orders of magnitude of that employed in the fusion-evaporation reactions can be used. But, by consider the primary beam intensity, the fusion-evaporation reactions have an advantage to access the vicinity of ^{100}Sn . The lowest cross-section of the fusion-evaporation reactions, 10^{-5} mb, would still be accessible with the improved overall efficiency discussed above, indicating the feasibility to measurement masses of the proton-rich Ag to Sn nuclei with the SHE-mass facility.

5.4.2 Neutron-rich superheavy nuclei

A region in nuclear chart centered around $Z \sim 110 - 120$ and $N \sim 184$, where long-lived and neutron-rich superheavy nuclei are predicted, called the “island of stability”, is an important topic in not only nuclear physics and also nuclear chemistry. Fusion evaporation reactions between stable nuclei are widely employed to access superheavy nuclei but cannot reach such a neutron-rich region due to the “curvature” of the β -stability line. This limitation can be found in left panel of Fig 5.12.

Multinucleon transfer (MNT) reactions with actinide elements (e.g.: $^{248}\text{Cm} + ^{238}\text{U}$, $^{238}\text{U} + ^{238}\text{U}$) have been discussed as a possible way to access the neutron-rich (super)heavy nuclei [134]. However there are two technical issues impeding performing efficient experiments with MNT reactions due to their characteristic properties: experimental equipment must have sufficient capability to handle the very wide angular and energy distributions

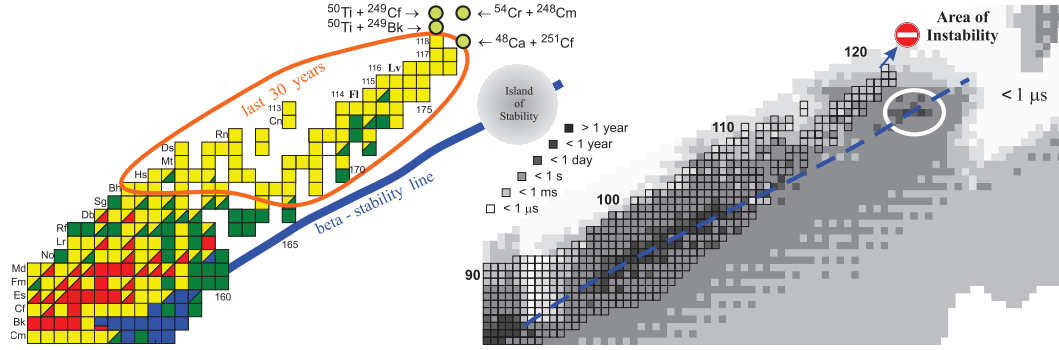


Figure 5.12: (Left) Upper part of the nuclear chart. Current and planned experiments on synthesis of elements 118-120 are shown. Each box is color-coded by its decay processes: yellow is α -decay, red is β^+ /EC-decay, blue is β^- -decay, and green is spontaneous fission. (Right) Predicted half-lives of superheavy nuclei. Known nuclei are shown by the outlined rectangles. This figure is taken from [133]

of the MNT reaction products. The gas-filled type separators like GARIS-II could cancel out the large energy dispersion of ions in principle, as discussed in Section 2.2. Main components of MNT reaction products are distributed in the range of $\sim 0^\circ - 60^\circ$ in both $^{248}\text{Cm} + ^{238}\text{U}$ [135] and $^{238}\text{U} + ^{238}\text{U}$ [136] cases. The angular acceptance of GARIS-II is 18.5 msr, thus it could collect and transport about 40% of nobelium isotopes produced via the $^{248}\text{Cm} + ^{238}\text{U}$ reaction, by considering the predicted angular distribution [135].

While gas-filled type separators have the capability to handle the MNT reaction products, an additional problem is primary beam separation, is a limitation that appears due to a minimal difference in the $B\rho$ -values of the MNT and primary beam. We have demonstrated this primary beam separation problem can be solved by employing the beam stoppers we developed. Thus mass measurements of neutron-rich (super)heavy nuclei produced by MNT reactions are a good candidate for one of the further applications of the SHE-mass facility.

Mass measurements of neutron-rich superheavy nuclei are important for another side problem – particle identification. Because the dominant decay process for neutron-rich superheavy nuclei is predicted to be spontaneous fission, and extremely long lifetimes are predicted, the conventional identification technique of observation of α -decay chains toward known nuclei cannot be applied in this region. Therefore precision mass measurements are notable as a possible new identification technique for superheavy nuclei.

Chapter 6

SUMMARY AND CONCLUSIONS

Nuclear masses of proton-rich nuclei along the $N = Z$ line in the $A \sim 60 - 80$ region are crucial for the several topics in nuclear- and nuclear astro-physics, such as, the rp -process in the X-ray bursts, the unitarity of the CKM matrix, and Coulomb displacement energy. However, in the many cases, accuracy and precision of mass data have not satisfied their requirements. Then the precision mass measurement experiments of these intermediate-mass proton-rich nuclei with The SHE-mass facility were proposed in the present study.

The intermediate-mass proton-rich nuclei can be produced using symmetric fusion-evaporation reactions. In performing mass measurements at the SHE-mass facility with symmetric reactions, a difficulty arises from the lack of separation between the primary beams and the reaction products in GARIS-II due to the small difference of their $B\rho$ -values. Thus, the use of these symmetric reactions with intense primary beams could lead to damages to the experimental equipments by irradiation with intense contaminants.

To overcome this, the two independent beam stoppers, Stopper1 and Stopper2, have been designed and developed to enhance the suppression of such particles in GARIS-II. A performance evaluation was carried out by using the $^{208}\text{Pb}(^{18}\text{O}, 3n)^{223}\text{Th}$ reaction. Stopper1 can suppress $\sim 95\%$ of the contaminants from reaching the GARIS-II focal plane, while maintaining $\sim 80\%$ of ^{223}Th . The Stopper2 measurement shows results similar to those obtained with Stopper1. Consequently, we have achieved a 200-fold enhancement of the signal-to-noise ratio at the GARIS-II focal plane.

The masses of ^{63}Cu , $^{64-66}\text{Zn}$, $^{65-67}\text{Ga}$, $^{65-67}\text{Ge}$, ^{67}As , $^{78,81}\text{Br}$, $^{79\text{m}}\text{Kr}$, $^{80,81\text{m}}\text{Rb}$, and $^{79,80}\text{Sr}$ were measured by using the SHE-mass facility with the beam stoppers. The masses of these nuclides have been determined by the single reference method using isobaric references of well-known mass. There are some inconsistencies with the 2016 Atomic Mass Evaluation (AME16) values, and two corrected mass excess values are proposed: $\text{ME}(^{67}\text{Ge}) = -62675.2(46)$ keV and $\text{ME}(^{81}\text{Br}) = -77955.4(53)$ keV. This result reinforces the need for direct mass measurements of all nuclides, even for stable isotopes, if their masses were previously evaluated by indirect techniques. The relative mass precisions in the present study span the range of $\delta m/m \sim 10^{-7}$ to 10^{-8} . In the most precise measurement, that of ^{65}Ga , a mass uncertainty of 2.1 keV was obtained. This result shows that mass measurements satisfying the requirement of the CKM matrix can be achieved with the MRTOF-MS, given sufficient statistics.

In conclusion, we demonstrate that the SHE-mass facility is suitable for precision mass measurements of not only SHE but also intermediate-mass proton-rich nuclei, which are crucial to the rp -process.

Acknowledgement

I could never have achieved the study in this thesis without the cooperation of both the SLOWRI and Superheavy Element Device Development teams of RIKEN Nishina Center and KEK Wako Nuclear Science Center, and would like to express my gratitude to them. I also thank the RIKEN Nishina Center LINAC operators for their support of the experiments.

First and foremost, my heartfelt appreciation goes to Prof. Michiharu Wada, who has always given me insightful advice. I would like to thank Prof. Hiroari Miyatake who gave me an opportunity to address this study. I have had the gracious support of Prof. Akira Ozawa in proceeding with the study and thesis and also want to thank him. I would like to offer my special thanks to Dr. Yuta Ito who has cooperated with me on these studies from early days; I never could have proceeded with these studies nor carried out these experiments without him. I am deeply grateful to Dr. Daiya Kaji. His advice and suggestions were indispensable for producing these results. I would particularly like to thank Dr. Peter Schury, who always gave great help to any problems with both these studies and English. Prof. Marion MacCormick and Prof. Hendrik Schatz gave many insightful comments and suggestions, and I would also like to express gratitude to them. I would also like to thank Dr. Tetsuaki Moriguchi for his kind support in the experiment at Univ. of Tsukuba. My special thanks belong to the members of our experiments, Dr. Kouji Morimoto, Dr. Hiromitsu Haba, Dr. Marco Rosenbusch, Dr. Aiko Takamine, Mr. Ian Murray, Mr. Taiki Tanaka, Prof. Hermann Wollnik, Dr. Yoshikazu Hirayama, Dr. Yutaka Watanabe, and Ms. Momo Mukai. I am also very grateful to all other collaborators in the experiments.

I must also express my sincere gratitude to my family for encouraging me when I was young and instilling me with a desire for education and a strong work ethic.

Bibliography

- [1] A. Parikh, J. José, G. Sala, and C. Iliadis. Nucleosynthesis in type I X-ray bursts. *Progress in Particle and Nuclear Physics*, 69:225–253, 2013.
- [2] F. Özel and P. Freire. Masses, radii, and the equation of state of neutron stars. *Annual Review of Astronomy and Astrophysics*, 54(1):401–440, 2016.
- [3] A. Parikh, J. José, C. Iliadis, F. Moreno, and T. Rauscher. Impact of uncertainties in reaction q values on nucleosynthesis in type i x-ray bursts. *Phys. Rev. C*, 79:045802, Apr 2009.
- [4] H. Schatz and W.-J. Ong. Dependence of x-ray burst models on nuclear masses. *The Astrophysical Journal*, 844(2):139, 2017.
- [5] H. Schatz, A. Aprahamian, V. Barnard, L. Bildsten, A. Cumming, M. Ouellette, T. Rauscher, F.-K. Thielemann, and M. Wiescher. End point of the rp process on accreting neutron stars. *Phys. Rev. Lett.*, 86:3471–3474, Apr 2001.
- [6] X. L. Tu, H. S. Xu, M. Wang, Y. H. Zhang, Yu. A. Litvinov, Y. Sun, H. Schatz, X. H. Zhou, Y. J. Yuan, J. W. Xia, G. Audi, K. Blaum, C. M. Du, P. Geng, Z. G. Hu, W. X. Huang, S. L. Jin, L. X. Liu, Y. Liu, X. Ma, R. S. Mao, B. Mei, P. Shuai, Z. Y. Sun, H. Suzuki, S. W. Tang, J. S. Wang, S. T. Wang, G. Q. Xiao, X. Xu, T. Yamaguchi, Y. Yamaguchi, X. L. Yan, J. C. Yang, R. P. Ye, Y. D. Zang, H. W. Zhao, T. C. Zhao, X. Y. Zhang, and W. L. Zhan. Direct Mass Measurements of Short-Lived $A = 2Z - 1$ Nuclides ^{63}Ge , ^{65}As , ^{67}Se , and ^{71}Kr and Their Impact on Nucleosynthesis in the rp Process. *Phys. Rev. Lett.*, 106:112501, Mar 2011.
- [7] B. A. Brown, R. R. C. Clement, H. Schatz, A. Volya, and W. A. Richter. Proton drip-line calculations and the rp process. *Phys. Rev. C*, 65:045802, Mar 2002.
- [8] H. Schatz. The importance of nuclear masses in the astrophysical rp -process. *International Journal of Mass Spectrometry*, 251(2-3):293–299, 2006.
- [9] H. Schatz. Nuclear masses in astrophysics. *International Journal of Mass Spectroscopy*, 349–350:181–186, apr 2013.
- [10] P. Schury, C. Bachelet, M. Block, G. Bollen, D. A. Davies, M. Facina, C. M. Folden III, C. Guénaut, J. Huikari, E. Kwan, A. Kwiatkowski, D. J. Morrissey, R. Ringle, G. K. Pang, A. Prinke, J. Savory, H. Schatz, S. Schwarz, C. S. Sumithrarachchi, and T. Sun. Precision mass measurements of rare isotopes near $n = z = 33$ produced by fast beam fragmentation. *Phys. Rev. C*, 75:055801, May 2007.

- [11] J. Savory, P. Schury, C. Bachelet, M. Block, G. Bollen, M. Facina, C. M. Folden, C. Guénaut, E. Kwan, A. A. Kwiatkowski, D. J. Morrissey, G. K. Pang, A. Prinke, R. Ringle, H. Schatz, S. Schwarz, and C. S. Sumithrarachchi. *rp*. *Phys. Rev. Lett.*, 102:132501, Mar 2009.
- [12] D. Rodríguez, V. S. Kolhinen, G. Audi, J. Äystö, D. Beck, K. Blaum, G. Bollen, F. Herfurth, A. Jokinen, A. Kellerbauer, H. J. Kluge, M. Oinonen, H. Schatz, E. Sauvan, and S. Schwarz. Mass measurement on the *rp*-process waiting point ^{72}Kr . *Phys. Rev. Lett.*, 93:161104, Oct 2004.
- [13] A. M. Rogers, M. A. Famiano, W. G. Lynch, M. S. Wallace, F. Amorini, D. Bazin, R. J. Charity, F. Delaunay, R. T. de Souza, J. Elson, A. Gade, D. Galaviz, M.-J. van Goethem, S. Hudan, J. Lee, S. Lobastov, S. Lukyanov, M. Matoš, M. Mocko, H. Schatz, D. Shapira, L. G. Sobotka, M. B. Tsang, and G. Verde. Ground-state proton decay of ^{69}Br and implications for the ^{68}Se astrophysical rapid proton-capture process waiting point. *Phys. Rev. Lett.*, 106:252503, Jun 2011.
- [14] I. S. Towner and J. C. Hardy. The evaluation of V_{ud} and its impact on the unitarity of the Cabibbo-Kobayashi-Maskawa quark-mixing matrix. *Reports on Progress in Physics*, 73(4):046301, 2010.
- [15] J. C. Hardy and I. S. Towner. Superaligned $0^+ \rightarrow 0^+$ nuclear β decays: 2014 critical survey, with precise results for V_{ud} and CKM unitarity. *Phys. Rev. C*, 91(2), feb 2015.
- [16] M. Karny, L. Batist, D. Jenkins, M. Kavatsyuk, O. Kavatsyuk, R. Kirchner, A. Korogul, E. Roeckl, and J. Żylicz. Excitation energy of the $t = 0$ β -decaying 9^+ isomer in ^{70}Br . *Phys. Rev. C*, 70:014310, Jul 2004.
- [17] C. N. Davids. *Masses of New Isotopes in the fp Shell*, pages 419–430. Springer US, Boston, MA, 1980.
- [18] G. Gürdal and E.A. McCutchan. Nuclear data sheets for $a = 70$. *Nuclear Data Sheets*, 136:1 – 162, 2016.
- [19] Meng Wang, G. Audi, F.G. Kondev, W.J. Huang, S. Naimi, and Xing Xu. The ame2016 atomic mass evaluation (ii). tables, graphs and references. *Chinese Physics C*, 41(3):030003, 2017.
- [20] A. Kellerbauer, G. Audi, D. Beck, K. Blaum, G. Bollen, B. A. Brown, P. Delahaye, C. Guénaut, F. Herfurth, H.-J. Kluge, D. Lunney, S. Schwarz, L. Schweikhard, and C. Yazidjian. Direct mass measurements on the superallowed emitter ^{74}Rb and its daughter ^{74}Kr : Isospin-symmetry-breaking correction for standard-model tests. *Phys. Rev. Lett.*, 93:072502, Aug 2004.
- [21] A. Kellerbauer, G. Audi, D. Beck, K. Blaum, G. Bollen, C. Guénaut, F. Herfurth, A. Herlert, H.-J. Kluge, D. Lunney, S. Schwarz, L. Schweikhard, C. Weber, and C. Yazidjian. High-precision masses of neutron-deficient rubidium isotopes using a penning trap mass spectrometer. *Phys. Rev. C*, 76:045504, Oct 2007.

- [22] S. Malbrunot-Ettenauer, T. Brunner, U. Chowdhury, A. T. Gallant, V. V. Simon, M. Brodeur, A. Chaudhuri, E. Mané, M. C. Simon, C. Andreoiu, G. Audi, J. R. Crespo López-Urrutia, P. Delheij, G. Gwinner, A. Lapierre, D. Lunney, M. R. Pearson, R. Ringle, J. Ullrich, and J. Dilling. Penning trap mass measurements utilizing highly charged ions as a path to benchmark isospin-symmetry breaking corrections in ^{74}Rb . *Phys. Rev. C*, 91:045504, Apr 2015.
- [23] W.J. Huang, G. Audi, Meng Wang, F.G. Kondev, S. Naimi, and Xing Xu. The ame2016 atomic mass evaluation (i). evaluation of input data; and adjustment procedures. *Chinese Physics C*, 41(3):030002, 2017.
- [24] E. Wigner. On the Consequences of the Symmetry of the Nuclear Hamiltonian on the Spectroscopy of Nuclei. *Phys. Rev.*, 51:106–119, Jan 1937.
- [25] G. Audi, M. Wang, A.H. Wapstra, F.G. Kondev, M. MacCormick, X. Xu, and B. Pfeiffer. The ame2012 atomic mass evaluation. *Chinese Physics C*, 36(12):1287, 2012.
- [26] M. MacCormick. private communication.
- [27] W. E. Ormand. Mapping the proton drip line up to $A = 70$. *Phys. Rev. C*, 55:2407–2417, May 1997.
- [28] K. Kaneko, Y. Sun, T. Mizusaki, and S. Tazaki. Variation in Displacement Energies Due to Isospin-Nonconserving Forces. *Phys. Rev. Lett.*, 110:172505, Apr 2013.
- [29] P. Ruotsalainen, D. G. Jenkins, M. A. Bentley, R. Wadsworth, C. Scholey, K. Auranen, P. J. Davies, T. Grahn, P. T. Greenlees, J. Henderson, A. Herzán, U. Jakobsson, P. Joshi, R. Julin, S. Juutinen, J. Konki, M. Leino, G. Lotay, A. J. Nichols, A. Obertelli, J. Pakarinen, J. Partanen, P. Peura, P. Rahkila, M. Sandzelius, J. Sarén, J. Sorri, S. Stolze, and J. Uusitalo. Spectroscopy of proton-rich ^{66}Se up to $J^{\pi} = 6^{+}$: Isospin-breaking effect in the $A = 66$ isobaric triplet. *Phys. Rev. C*, 88:041308, Oct 2013.
- [30] D. M. Debenham, M. A. Bentley, P. J. Davies, T. Haylett, D. G. Jenkins, P. Joshi, L. F. Sinclair, R. Wadsworth, P. Ruotsalainen, J. Henderson, K. Kaneko, K. Auranen, H. Badran, T. Grahn, P. Greenlees, A. Herzán, U. Jakobsson, J. Konki, R. Julin, S. Juutinen, M. Leino, J. Sorri, J. Pakarinen, P. Papadakis, P. Peura, J. Partanen, P. Rahkila, M. Sandzelius, J. Sarén, C. Scholey, S. Stolze, J. Uusitalo, H. M. David, G. de Angelis, W. Korten, G. Lotay, M. Mallaburn, and E. Sahin. Spectroscopy of ^{70}Kr and isospin symmetry in the $t = 1fpg$ shell nuclei. *Phys. Rev. C*, 94:054311, Nov 2016.
- [31] J. Henderson, D. G. Jenkins, K. Kaneko, P. Ruotsalainen, P. Sarriguren, K. Auranen, M. A. Bentley, P. J. Davies, A. Görden, T. Grahn, P. T. Greenlees, A. Hay, T. W. Henry, A. Herzán, U. Jakobsson, R. Julin, S. Juutinen, J. Konki, M. Leino, C. McPeake, S. Milne, A. J. Nichols, J. Pakarinen, P. Papadakis, J. Partanen, P. Peura, P. Rahkila, E. Sahin, M. Sandzelius, J. Sarén, C. Scholey, M. Siciliano, L. Sinclair, J. Sorri, S. Stolze, J. Uusitalo, R. Wadsworth, and M. Zielińska. Spectroscopy on the proton drip-line: Probing the structure dependence of isospin nonconserving interactions. *Phys. Rev. C*, 90:051303, Nov 2014.

- [32] F. P. Heßberger, S. Hofmann, D. Ackermann, V. Ninov, M. Leino, S. Saro, A. Andreyev, A. Lavrentev, A. G. Popeko, and A. V. Yeremin. Decay properties of neutron-deficient nuclei in the region $z = 86\text{--}92$. *The European Physical Journal A*, 8(4):521–535, Jul 2000.
- [33] H. Keller, R. Kirchner, O. Klepper, E. Roeckl, D. Schardt, R. S. Simon, P. Kleinheinz, R. Menegazzo, C. F. Liang, P. Paris, K. Rykaczewski, and J. Żylicz. β^+ -endpoint measurements near 100sn and 146gd. *Zeitschrift für Physik A Hadrons and Nuclei*, 340(4):363–370, Dec 1991.
- [34] David G. Jenkins. Waiting points in the astrophysical rp process: How unbound are ^{69}Br and ^{73}Rb ? *Phys. Rev. C*, 78:012801, Jul 2008.
- [35] G. F. Lima, A. Lépine-Szily, G. Audi, W. Mittig, M. Chartier, N. A. Orr, R. Lichtenhaler, J. C. Angelique, J. M. Casandjian, A. Cunsolo, C. Donzaud, A. Foti, A. Gillibert, M. Lewitowicz, S. Lukyanov, M. MacCormick, D. J. Morrissey, A. N. Ostrowski, B. M. Sherrill, C. Stephan, T. Suomijarvi, L. Tassan-Got, D. J. Vieira, A. C. C. Villari, and J. M. Wouters. Direct mass measurements of proton-rich isotopes of ge, as, se, and br. *Phys. Rev. C*, 65:044618, Apr 2002.
- [36] B. Jurado, H. Savajols, W. Mittig, N.A. Orr, P. Roussel-Chomaz, D. Baiborodin, W.N. Catford, M. Chartier, C.E. Demonchy, Z. Dlouhý, A. Gillibert, L. Giot, A. Khouaja, A. Lépine-Szily, S. Lukyanov, J. Mrazek, Y.E. Penionzhkevich, S. Pita, M. Rousseau, and A.C. Villari. Mass measurements of neutron-rich nuclei near the $n=20$ and 28 shell closures. *Physics Letters B*, 649(1):43 – 48, 2007.
- [37] M. B. Gómez-Hornillos, M. Chartier, W. Mittig, A. Lépine-Szily, L. Caballero, C. E. Demonchy, G. Georgiev, N. A. Orr, G. Politi, M. Rousseau, P. Roussel-Chomaz, and A. C. C. Villari. Direct mass measurements of ^{68}Se and ^{80}Y . *Phys. Rev. C*, 78:014311, Jul 2008.
- [38] M. Matoš, A. Estradé, H. Schatz, D. Bazin, M. Famiano, A. Gade, S. George, W.G. Lynch, Z. Meisel, M. Portillo, A. Rogers, D. Shapira, A. Stolz, M. Wallace, and J. Yurkon. Time-of-flight mass measurements of exotic nuclei. *Nuclear Instruments and Methods in Physics Research Section A: Accelerators, Spectrometers, Detectors and Associated Equipment*, 696(Supplement C):171 – 179, 2012.
- [39] M. Kobayashi, S. Michimasa, Y. Kiyokawa, H. Baba, G.P.A. Berg, M. Dozono, N. Fukuda, T. Furuno, E. Ideguchi, N. Inabe, T. Kawabata, S. Kawase, K. Kisamori, K. Kobayashi, T. Kubo, Y. Kubota, C.S. Lee, M. Matsushita, H. Miya, A. Mizukami, H. Nagakura, D. Nishimura, H. Oikawa, S. Ota, H. Sakai, S. Shimoura, A. Stolz, H. Suzuki, M. Takaki, H. Takeda, S. Takeuchi, H. Tokieda, T. Uesaka, K. Yako, Y. Yamaguchi, Y. Yanagisawa, R. Yokoyama, and K. Yoshida. Time-of-flight mass measurements of neutron-rich ca isotopes beyond $n = 34$. *RIKEN Accelerator Progress Report*, 49:48, 2016.
- [40] H. Wollnik. Laterally and longitudinally dispersive recoil mass separators. *Nuclear Instruments and Methods in Physics Research Section B: Beam Interactions with Materials and Atoms*, 26(1):267 – 272, 1987.

- [41] W. Mittig, A. Lépine-Szily, and N. A. Orr. Mass measurement far from stability. *Annual Review of Nuclear and Particle Science*, 47(1):27–66, 1997.
- [42] Yu.A. Litvinov, H. Geissel, T. Radon, F. Attallah, G. Audi, K. Beckert, F. Bosch, M. Falch, B. Franzke, M. Hausmann, M. Hellström, Th. Kerscher, O. Klepper, H.-J. Kluge, C. Kozhuharov, K.E.G. Löbner, G. Münzenberg, F. Nolden, Yu.N. Novikov, W. Quint, Z. Patyk, H. Reich, C. Scheidenberger, B. Schlitt, M. Steck, K. Sümmerer, L. Vermeeren, M. Winkler, Th. Winkler, and H. Wollnik. Mass measurement of cooled neutron-deficient bismuth projectile fragments with time-resolved schottky mass spectrometry at the frs-esr facility. *Nuclear Physics A*, 756(1):3 – 38, 2005.
- [43] M Hausmann, F Attallah, K Beckert, F Bosch, A Dolinskiy, H Eickhoff, M Falch, B Franczak, B Franzke, H Geissel, Th Kerscher, O Klepper, H.-J Kluge, C Kozhuharov, K.E.G Löbner, G Münzenberg, F Nolden, Yu.N Novikov, T Radon, H Schatz, C Scheidenberger, J Stadlmann, M Steck, T Winkler, and H Wollnik. First isochronous mass spectrometry at the experimental storage ring esr. *Nuclear Instruments and Methods in Physics Research Section A: Accelerators, Spectrometers, Detectors and Associated Equipment*, 446(3):569 – 580, 2000.
- [44] Bernhard Franzke. The heavy ion storage and cooler ring project esr at gsi. *Nuclear Instruments and Methods in Physics Research Section B: Beam Interactions with Materials and Atoms*, 24(Part 1):18 – 25, 1987.
- [45] L. Chen, W.R. Plaß, H. Geissel, R. Knöbel, C. Kozhuharov, Yu.A. Litvinov, Z. Patyk, C. Scheidenberger, K. Siegień-Iwaniuk, B. Sun, H. Weick, K. Beckert, P. Beller, F. Bosch, D. Boutin, L. Caceres, J.J. Carroll, D.M. Cullen, I.J. Cullen, B. Franzke, J. Gerl, M. Górská, G.A. Jones, A. Kishada, J. Kurcewicz, S.A. Litvinov, Z. Liu, S. Mandal, F. Montes, G. Münzenberg, F. Nolden, T. Ohtsubo, Zs. Podolyák, R. Propri, S. Rigby, N. Saito, T. Saito, M. Shindo, M. Steck, P.M. Walker, S. Williams, M. Winkler, H.-J. Wollersheim, and T. Yamaguchi. New results on mass measurements of stored neutron-rich nuclides in the element range from pt to u with the frs-esr facility at 360–400 mev/u. *Nuclear Physics A*, 882(Supplement C):71 – 89, 2012.
- [46] J.W. Xia, W.L. Zhan, B.W. Wei, Y.J. Yuan, M.T. Song, W.Z. Zhang, X.D. Yang, P. Yuan, D.Q. Gao, H.W. Zhao, X.T. Yang, G.Q. Xiao, K.T. Man, J.R. Dang, X.H. Cai, Y.F. Wang, J.Y. Tang, W.M. Qiao, Y.N. Rao, Y. He, L.Z. Mao, and Z.Z. Zhou. The heavy ion cooler-storage-ring project (hirfl-csr) at lanzhou. *Nuclear Instruments and Methods in Physics Research Section A: Accelerators, Spectrometers, Detectors and Associated Equipment*, 488(1):11 – 25, 2002.
- [47] A. Ozawa, T. Uesaka, M. Wakasugi, and the Rare-RI Ring Collaboration. The rare-ri ring. *Progress of Theoretical and Experimental Physics*, 2012(1):03C009, 2012.
- [48] X. Xu, P. Zhang, P. Shuai, R. J. Chen, X. L. Yan, Y. H. Zhang, M. Wang, Yu. A. Litvinov, H. S. Xu, T. Bao, X. C. Chen, H. Chen, C. Y. Fu, S. Kubono, Y. H. Lam, D. W. Liu, R. S. Mao, X. W. Ma, M. Z. Sun, X. L. Tu, Y. M. Xing, J. C. Yang, Y. J. Yuan, Q. Zeng, X. Zhou, X. H. Zhou, W. L. Zhan, S. Litvinov, K. Blaum, G. Audi, T. Uesaka, Y. Yamaguchi, T. Yamaguchi, A. Ozawa, B. H. Sun, Y. Sun, A. C. Dai, and F. R. Xu. Identification of the lowest $t = 2$, $J^\pi = 0^+$ isobaric analog state in

- ^{52}Co and its impact on the understanding of β -decay properties of ^{52}Ni . *Phys. Rev. Lett.*, 117:182503, Oct 2016.
- [49] D A Nesterenko, A Kankainen, L Canete, M Block, D Cox, T Eronen, C Fahlander, U Forsberg, J Gerl, P Golubev, J Hakala, A Jokinen, V S Kolhinen, J Koponen, N Lalović?, Ch Lorenz, I D Moore, P Papadakis, J Reinikainen, S Rinta-Antila, D Rudolph, L G Sarmiento, A Voss, and J Äystö. High-precision mass measurements for the isobaric multiplet mass equation at $a = 52$. *Journal of Physics G: Nuclear and Particle Physics*, 44(6):065103, 2017.
 - [50] Y Abe, Y Yamaguchi, M Wakasugi, T Uesaka, A Ozawa, F Suzaki, D Nagae, H Miura, T Yamaguchi, and Y Yano. Isochronous field study of the rare-ri ring. *Physica Scripta*, 2015(T166):014047, 2015.
 - [51] Klaus Blaum. High-accuracy mass spectrometry with stored ions. *Physics Reports*, 425(1):1 – 78, 2006.
 - [52] G Bollen, S Becker, H.-J Kluge, M Knig, R.B Moore, T Otto, H Raimbault-Hartmann, G Savard, L Schweikhard, and H Stolzenberg. Isoltrap: a tandem penning trap system for accurate on-line mass determination of short-lived isotopes. *Nuclear Instruments and Methods in Physics Research Section A: Accelerators, Spectrometers, Detectors and Associated Equipment*, 368(3):675 – 697, 1996.
 - [53] M. Smith, M. Brodeur, T. Brunner, S. Ettenauer, A. Lapierre, R. Ringle, V. L. Ryjkov, F. Ames, P. Bricault, G. W. F. Drake, P. Delheij, D. Lunney, F. Sarazin, and J. Dilling. First penning-trap mass measurement of the exotic halo nucleus ^{11}Li . *Phys. Rev. Lett.*, 101:202501, Nov 2008.
 - [54] A. Chaudhuri, C. Andreoiu, T. Brunner, U. Chowdhury, S. Ettenauer, A. T. Gallant, G. Gwinner, A. A. Kwiatkowski, A. Lennarz, D. Lunney, T. D. Macdonald, B. E. Schultz, M. C. Simon, V. V. Simon, and J. Dilling. Evidence for the extinction of the $n = 20$ neutron-shell closure for ^{32}Mg from direct mass measurements. *Phys. Rev. C*, 88:054317, Nov 2013.
 - [55] K. Blaum, G. Audi, D. Beck, G. Bollen, F. Herfurth, A. Kellerbauer, H.-J. Kluge, E. Sauvan, and S. Schwarz. Masses of ^{32}Ar and ^{33}Ar for fundamental tests. *Phys. Rev. Lett.*, 91:260801, Dec 2003.
 - [56] S. Naimi, G. Audi, D. Beck, K. Blaum, Ch. Böhm, Ch. Borgmann, M. Breitenfeldt, S. George, F. Herfurth, A. Herlert, A. Kellerbauer, M. Kowalska, D. Lunney, E. Minaya Ramirez, D. Neidherr, M. Rosenbusch, L. Schweikhard, R. N. Wolf, and K. Zuber. Surveying the $n = 40$ island of inversion with new manganese masses. *Phys. Rev. C*, 86:014325, Jul 2012.
 - [57] V. Manea, D. Atanasov, D. Beck, K. Blaum, C. Borgmann, R. B. Cakirli, T. Eronen, S. George, F. Herfurth, A. Herlert, M. Kowalska, S. Kreim, Yu. A. Litvinov, D. Lunney, D. Neidherr, M. Rosenbusch, L. Schweikhard, F. Wienholtz, R. N. Wolf, and K. Zuber. Collective degrees of freedom of neutron-rich $a \approx 100$ nuclei and the first mass measurement of the short-lived nuclide ^{100}rb . *Phys. Rev. C*, 88:054322, Nov 2013.

- [58] A. Casares, A. Kholomeev, and H. Wollnik. Multipass time-of-flight mass spectrometers with high resolving powers. *International Journal of Mass Spectrometry*, 206(3):267 – 273, 2001.
- [59] H. Wollnik and A. Casares. An energy-isochronous multi-pass time-of-flight mass spectrometer consisting of two coaxial electrostatic mirrors. *International Journal of Mass Spectrometry*, 227(2):217 – 222, 2003.
- [60] Robert N. Wolf, Gerrit Marx, Marco Rosenbusch, and Lutz Schweikhard. Static-mirror ion capture and time focusing for electrostatic ion-beam traps and multi-reflection time-of-flight mass analyzers by use of an in-trap potential lift. *International Journal of Mass Spectrometry*, 313(Supplement C):8 – 14, 2012.
- [61] P. Schury, Y. Ito, M. Wada, and H. Wollnik. Wide-band mass measurements with a multi-reflection time-of-flight mass spectrograph. *International Journal of Mass Spectrometry*, 359(Supplement C):19 – 25, 2014.
- [62] F. Wienholtz, D. Beck, K. Blaum, Ch. Borgmann, M. Breitenfeldt, R. B. Cakirli, S. George, F. Herfurth, J. D. Holt, M. Kowalska, S. Kreim, D. Lunney, V. Manea, J. Menendez, D. Neidherr, M. Rosenbusch, L. Schweikhard, A. Schwenk, J. Simonis, J. Stanja, R. N. Wolf, and K. Zuber. Masses of exotic calcium isotopes pin down nuclear forces. *Nature*, 498:346 – 349, 2013.
- [63] M. Rosenbusch, P. Ascher, D. Atanasov, C. Barbieri, D. Beck, K. Blaum, Ch. Borgmann, M. Breitenfeldt, R. B. Cakirli, A. Cipollone, S. George, F. Herfurth, M. Kowalska, S. Kreim, D. Lunney, V. Manea, P. Navrátil, D. Neidherr, L. Schweikhard, V. Somà, J. Stanja, F. Wienholtz, R. N. Wolf, and K. Zuber. Probing the $n = 32$ shell closure below the magic proton number $z = 20$: Mass measurements of the exotic isotopes $^{52,53}\text{K}$. *Phys. Rev. Lett.*, 114:202501, May 2015.
- [64] R.N. Wolf, F. Wienholtz, D. Atanasov, D. Beck, K. Blaum, Ch. Borgmann, F. Herfurth, M. Kowalska, S. Kreim, Yu. A. Litvinov, D. Lunney, V. Manea, D. Neidherr, M. Rosenbusch, L. Schweikhard, J. Stanja, and K. Zuber. Isoltrap’s multi-reflection time-of-flight mass separator/spectrometer. *International Journal of Mass Spectrometry*, 349(Supplement C):123 – 133, 2013. 100 years of Mass Spectrometry.
- [65] T. Dickel, W.R. Plaß, A. Becker, U. Czok, H. Geissel, E. Haettner, C. Jesch, W. Kinsel, M. Petrick, C. Scheidenberger, A. Simon, and M.I. Yavor. A high-performance multiple-reflection time-of-flight mass spectrometer and isobar separator for the research with exotic nuclei. *Nuclear Instruments and Methods in Physics Research Section A: Accelerators, Spectrometers, Detectors and Associated Equipment*, 777(Supplement C):172 – 188, 2015.
- [66] T. Dickel, W.R. Plaß, S. Ayet San Andres, J. Ebert, H. Geissel, E. Haettner, C. Hornung, I. Miskun, S. Pietri, S. Purushothaman, M.P. Reiter, A.-K. Rink, C. Scheidenberger, H. Weick, P. Dendooven, M. Diwisch, F. Greiner, F. Heiß, R. Knöbel, W. Lippert, I.D. Moore, I. Pohjalainen, A. Prochazka, M. Ranjan, M. Takechi, J.S. Winfield, and X. Xu. First spatial separation of a heavy ion isomeric beam with a multiple-reflection time-of-flight mass spectrometer. *Physics Letters B*, 744(Supplement C):137 – 141, 2015.

- [67] J.S. Winfield, H. Geissel, J. Gerl, G. Münzenberg, C. Nociforo, W.R. Plaß, C. Scheidenberger, H. Weick, M. Winkler, and M.I. Yavor. A versatile high-resolution magnetic spectrometer for energy compression, reaction studies and nuclear spectroscopy. *Nuclear Instruments and Methods in Physics Research Section A: Accelerators, Spectrometers, Detectors and Associated Equipment*, 704(Supplement C):76 – 83, 2013.
- [68] W.R. Plaß, T. Dickel, S. Purushothaman, P. Dendooven, H. Geissel, J. Ebert, E. Haettner, C. Jesch, M. Ranjan, M.P. Reiter, H. Weick, F. Amjad, S. Ayet, M. Diwisch, A. Estrade, F. Farinon, F. Greiner, N. Kalantar-Nayestanaki, R. Knöbel, J. Kurcewicz, J. Lang, I. Moore, I. Mukha, C. Nociforo, M. Petrick, M. Pfützner, S. Pietri, A. Prochazka, A.-K. Rink, S. Rinta-Antila, D. Schäfer, C. Scheidenberger, M. Takechi, Y.K. Tanaka, J.S. Winfield, and M.I. Yavor. The frs ion catcher – a facility for high-precision experiments with stopped projectile and fission fragments. *Nuclear Instruments and Methods in Physics Research Section B: Beam Interactions with Materials and Atoms*, 317(Part B):457 – 462, 2013. XVIth International Conference on ElectroMagnetic Isotope Separators and Techniques Related to their Applications, December 2–7, 2012 at Matsue, Japan.
- [69] Y. Ito, P. Schury, M. Wada, S. Naimi, T. Sonoda, H. Mita, F. Arai, A. Takamine, K. Okada, A. Ozawa, and H. Wollnik. Single-reference high-precision mass measurement with a multireflection time-of-flight mass spectrograph. *Phys. Rev. C*, 88:011306, Jul 2013.
- [70] P. Schury, M. Wada, Y. Ito, F. Arai, S. Naimi, T. Sonoda, H. Wollnik, V.A. Shchepunov, C. Smorra, and C. Yuan. A high-resolution multi-reflection time-of-flight mass spectrograph for precision mass measurements at RIKEN/SLOWRI. *Nuclear Instruments and Methods in Physics Research Section B: Beam Interactions with Materials and Atoms*, 335:39 – 53, 2014.
- [71] Toshiyuki Kubo. In-flight ri beam separator bigrips at riken and elsewhere in japan. *Nuclear Instruments and Methods in Physics Research Section B: Beam Interactions with Materials and Atoms*, 204(Supplement C):97 – 113, 2003. 14th International Conference on Electromagnetic Isotope Separators and Techniques Related to their Applications.
- [72] D. Kaji, K. Morimoto, N. Sato, A. Yoneda, and K. Morita. Gas-filled recoil ion separator garis-ii. *Nuclear Instruments and Methods in Physics Research Section B: Beam Interactions with Materials and Atoms*, 317, Part B:311 – 314, 2013.
- [73] S. C. Jeong, N. Imai, H. Ishiyama, H. Miyatake, and Y. X. Watanabe. Kiss:kek isotope separation system for β -decay spectroscopy. *KEK Report*, 2010(2), 2010.
- [74] M. Wada, Y. Ishida, T. Nakamura, Y. Kanai, T. M. Kojima, A. Takamine, Y. Yamazaki, K. Okada, A. Yoshida, T. Kubo, I. Katayama, S. Ohtani, V. Varentsov, H. Wollnik, V. Lioubimov, and H. A. Schuessler. *Laser spectroscopy of trapped ^7Be and ^{10}Be at a prototype slow RI-beam facility of RIKEN*, pages 309–319. Springer Berlin Heidelberg, Berlin, Heidelberg, 2007.
- [75] T. Sonoda, M. Wada, H. Tomita, C. Sakamoto, T. Takatsuka, T. Noto, H. Iimura, Y. Matsuo, T. Kubo, T. Shinozuka, T. Wakui, H. Mita, S. Naimi, T. Furukawa,

- Y. Itou, P. Schury, H. Miyatake, S. Jeong, H. Ishiyama, Y. Watanabe, and Y. Hirayama. Development of a gas cell-based laser ion source for riken palis. *Hyperfine Interactions*, 216(1):103–107, Apr 2013.
- [76] T. Kubo, M. Ishihara, N. Inabe, H. Kumagai, I. Tanihata, K. Yoshida, T. Nakamura, H. Okuno, S. Shimoura, and K. Asahi. The riken radioactive beam facility. *Nuclear Instruments and Methods in Physics Research Section B: Beam Interactions with Materials and Atoms*, 70(1):309 – 319, 1992.
- [77] P. Schury, M. Wada, Y. Ito, D. Kaji, F. Arai, M. MacCormick, I. Murray, H. Haba, S. Jeong, S. Kimura, H. Koura, H. Miyatake, K. Morimoto, K. Morita, A. Ozawa, M. Rosenbusch, M. Reponen, P.-A. Söderström, A. Takamine, T. Tanaka, and H. Wollnik. First online multireflection time-of-flight mass measurements of isobar chains produced by fusion-evaporation reactions: Toward identification of superheavy elements via mass spectroscopy. *Phys. Rev. C*, 95:011305, Jan 2017.
- [78] P. Armbruster, J. Eidens, J.W. Grter, H. Lawin, E. Roeckl, and K. Sistemich. Are gas-filled magnetic separators a useful tool to investigate heavy fast recoils from nuclear reactions? *Nuclear Instruments and Methods*, 91(3):499 – 507, 1971.
- [79] P. Sigmund and K.B. Winterbon. Small-angle multiple scattering of ions in the screened coulomb region. *Nuclear Instruments and Methods*, 119:541 – 557, 1974.
- [80] D. Kaji, K. Morimoto, H. Haba, Y. Kudou, K. Ozeki, T. Sumita, A. Yoneda, N. Sato, Y. Wakabayashi, M. Murakami, F. Tokanai, S. Namai, and K. Morita. Garis-ii commissioning # 1. *RIKEN Accelerator Progress Report*, 44:226 – 227, 2010.
- [81] P. Schury, M. Wada, Y. Ito, F. Arai, D. Kaji, S. Kimura, K. Morimoto, H. Haba, S. Jeong, H. Koura, H. Miyatake, K. Morita, M. Reponen, A. Ozawa, T. Sonoda, A. Takamine, and H. Wollnik. Status of the low-energy super-heavy element facility at riken. *Nuclear Instruments and Methods in Physics Research Section B: Beam Interactions with Materials and Atoms*, 376(Supplement C):425 – 428, 2016. Proceedings of the XVIIth International Conference on Electromagnetic Isotope Separators and Related Topics (EMIS2015), Grand Rapids, MI, U.S.A., 11-15 May 2015.
- [82] Y. Ito, P. Schury, M. Wada, S. Naimi, C. Smorra, T. Sonoda, H. Mita, A. Takamine, K. Okada, A. Ozawa, and H. Wollnik. A novel ion cooling trap for multi-reflection time-of-flight mass spectrograph. *Nuclear Instruments and Methods in Physics Research Section B: Beam Interactions with Materials and Atoms*, 317:544 – 549, 2013. XVIth International Conference on ElectroMagnetic Isotope Separators and Techniques Related to their Applications, December 2-???, 2012 at Matsue, Japan.
- [83] T. Brunner, A.R. Mueller, K. O’Sullivan, M.C. Simon, M. Kossick, S. Ettenauer, A.T. Gallant, E. Man, D. Bishop, M. Good, G. Gratta, and J. Dilling. A large bradbury nielsen ion gate with flexible wire spacing based on photo-etched stainless steel grids and its characterization applying symmetric and asymmetric potentials. *International Journal of Mass Spectrometry*, 309(Supplement C):97 – 103, 2012.
- [84] O.B. Tarasov and D. Bazin. Development of the program LISE: application to fusion-evaporation. *Nuclear Instruments and Methods in Physics Research Section B: Beam Interactions with Materials and Atoms*, 204:174–178, 2003.

- [85] J. C. Batchelder. PhD thesis, University of California, 1993.
- [86] J. C. Batchelder, D. M. Moltz, T. J. Ognibene, M. W. Rowe, and Joseph Cerny. Beta-delayed proton decay of ^{65}Se . *Phys. Rev. C*, 47:2038–2042, May 1993.
- [87] J. C. Batchelder, D. M. Moltz, T. J. Ognibene, M. W. Rowe, R. J. Tighe, and Joseph Cerny. Beta-delayed proton decay of ^{73}Sr . *Phys. Rev. C*, 48:2593–2597, Dec 1993.
- [88] K.E. Gregorich. Simulation of recoil trajectories in gas-filled magnetic separators. *Nuclear Instruments and Methods in Physics Research Section A: Accelerators, Spectrometers, Detectors and Associated Equipment*, 711:47 – 59, 2013.
- [89] G Schiwietz and P.L Grande. Improved charge-state formulas. *Nuclear Instruments and Methods in Physics Research Section B: Beam Interactions with Materials and Atoms*, 175:125 – 131, 2001. Twelfth International Conference of Ion Beam Modification of Materials.
- [90] S. Agostinelli et al. Geant4-simulation toolkit. *Nuclear Instruments and Methods in Physics Research Section A: Accelerators, Spectrometers, Detectors and Associated Equipment*, 506(3):250 – 303, 2003.
- [91] A. Takamine, M. Wada, Y. Ishida, T. Nakamura, K. Okada, Y. Yamazaki, T. Kambara, Y. Kanai, T. M. Kojima, Y. Nakai, N. Oshima, A. Yoshida, T. Kubo, S. Ohtani, K. Noda, I. Katayama, P. Hostain, V. Varentsov, and H. Wollnik. Space-charge effects in the catcher gas cell of a rf ion guide. *Review of Scientific Instruments*, 76(10):103503, 2005.
- [92] Reiko co., ltd., <http://www.reiko.co.jp>.
- [93] John P Greene and Christopher J Lister. The production of sulfur targets for γ -ray spectroscopy. *Nuclear Instruments and Methods in Physics Research Section A: Accelerators, Spectrometers, Detectors and Associated Equipment*, 480(1):79 – 83, 2002.
- [94] D. Kaji and K. Morimoto. Double-layered target and identification method of individual target correlated with evaporation residues. *Nuclear Instruments and Methods in Physics Research Section A: Accelerators, Spectrometers, Detectors and Associated Equipment*, 792:11 – 14, 2015.
- [95] Balraj Singh. Nuclear data sheets for $a = 80$. *Nuclear Data Sheets*, 105(2):223 – 418, 2005.
- [96] F. Arai. private communication.
- [97] Rene Brun and Fons Rademakers. Root-an object oriented data analysis framework. *Nuclear Instruments and Methods in Physics Research Section A: Accelerators, Spectrometers, Detectors and Associated Equipment*, 389(1):81 – 86, 1997.
- [98] K. Lan and J. W. Jorgenson. A hybrid of exponential and gaussian functions as a simple model of asymmetric chromatographic peaks. *Journal of Chromatography A*, 915(1–2):1–13, 2001.

- [99] Y. Ito. *A multi-reflection time-of-flight mass spectrograph for high-precision mass measurements of short-lived nuclei*. PhD thesis, University of Tsukuba, 2013.
- [100] M. J. Murphy, C. N. Davids, E. B. Norman, and R. C. Pardo. Mass and low-lying levels of ^{67}Ge ; trends in the structure of $^{63,65}\text{Ni}$, $^{65,67}\text{Zn}$, and $^{67,69}\text{Ge}$. *Phys. Rev. C*, 17:1574–1582, May 1978.
- [101] A M Al-Naser, A H Behbehani, P A Butler, L L Green, A N James, C J Lister, P J Nolan, N R F Rammo, J F Sharpey-Schafer, H M Sheppard, L H Zybert, and R Zybert. Decay scheme of excited states in 67 ge. *Journal of Physics G: Nuclear Physics*, 5(3):423, 1979.
- [102] T. Otto, G. Bollen, G. Savard, L. Schweikhard, H. Stolzenberg, G. Audi, R.B. Moore, G. Rouleau, J. Szerypo, and Z. Patyk. Penning-trap mass measurements of neutron-deficient rb and sr isotopes. *Nuclear Physics A*, 567(2):281 – 302, 1994.
- [103] E. Haettner, D. Ackermann, G. Audi, K. Blaum, M. Block, S. Eliseev, T. Fleckenstein, F. Herfurth, F. P. Heßberger, S. Hofmann, J. Ketelaer, J. Ketter, H.-J. Kluge, G. Marx, M. Mazzocco, Yu. N. Novikov, W. R. Plaß, S. Rahaman, T. Rauscher, D. Rodríguez, H. Schatz, C. Scheidenberger, L. Schweikhard, B. Sun, P. G. Thirolf, G. Vorobjev, M. Wang, and C. Weber. Mass measurements of very neutron-deficient mo and tc isotopes and their impact on rp process nucleosynthesis. *Phys. Rev. Lett.*, 106:122501, Mar 2011.
- [104] R. C. Waddell and E. N. Jensen. Decay scheme of br^{82} . *Phys. Rev.*, 102:816–823, May 1956.
- [105] Balraj Singh. Nuclear data sheets for $a = 79$. *Nuclear Data Sheets*, 96(1):1 – 176, 2002.
- [106] Coral M. Baglin. Nuclear data sheets for $a = 81$. *Nuclear Data Sheets*, 109(10):2257 – 2437, 2008.
- [107] R. O. Bondelid and E. E. Dowling Whiting. (p, n) threshold-curve shapes and measurements of threshold enelrgy with h_1^+ beams. *Phys. Rev.*, 134:B591–B594, May 1964.
- [108] R. T. Nichols, A. V. Pohm, J. H. Talboy Jr., and E. N. Jensen. Beta-ray spectrometer for coincidence measurements. *Review of Scientific Instruments*, 26(6):580–583, 1955.
- [109] J.K. Tuli. Nuclear data sheets for $a = 82$. *Nuclear Data Sheets*, 98(2):209 – 334, 2003.
- [110] <http://research.jyu.fi./igisol/jyfltrap-masses/>.
- [111] <https://isoltrap.web.cern.ch/isoltrap/database/isodb.asp>.
- [112] Knöbel, R., Diwisch, M., Geissel, H., Litvinov, Yu. A., Patyk, Z., Plaß?, W. R., Scheidenberger, C., Sun, B., Weick, H., Bosch, F., Boutin, D., Chen, L., Dimopoulou, C., Dolinskii, A., Franczak, B., Franzke, B., Hausmann, M., Kozhuharov, C., Kurcewicz, J., Litvinov, S. A., Matoš, M., Mazzocco, M., Münzenberg, G., Nakajima, S., Nociforo, C., Nolden, F., Ohtsubo, T., Ozawa, A., Stadlmann, J., Steck, M., Suzuki, T.,

- Walker, P. M., Winkler, M., and Yamaguchi, T. New results from isochronous mass measurements of neutron-rich uranium fission fragments with the frs-esr-facility at gsi. *Eur. Phys. J. A*, 52(5):138, 2016.
- [113] L. Chen, Yu. A. Litvinov, W. R. Plaß, K. Beckert, P. Beller, F. Bosch, D. Boutin, L. Caceres, R. B. Cakirli, J. J. Carroll, R. F. Casten, R. S. Chakrawarthy, D. M. Cullen, I. J. Cullen, B. Franzke, H. Geissel, J. Gerl, M. Górski, G. A. Jones, A. Kishada, R. Knöbel, C. Kozhuharov, S. A. Litvinov, Z. Liu, S. Mandal, F. Montes, G. Münzenberg, F. Nolden, T. Ohtsubo, Z. Patyk, Zs. Podolyák, R. Propri, S. Rigby, N. Saito, T. Saito, C. Scheidenberger, M. Shindo, M. Steck, P. Ugorowski, P. M. Walker, S. Williams, H. Weick, M. Winkler, H.-J. Wollersheim, and T. Yamaguchi. Schottky mass measurement of the ^{208}Hg isotope: Implication for the proton-neutron interaction strength around doubly magic ^{208}Pb . *Phys. Rev. Lett.*, 102:122503, Mar 2009.
- [114] X.L. Tu, M. Wang, Yu.A. Litvinov, Y.H. Zhang, H.S. Xu, Z.Y. Sun, G. Audi, K. Blaum, C.M. Du, W.X. Huang, Z.G. Hu, P. Geng, S.L. Jin, L.X. Liu, Y. Liu, B. Mei, R.S. Mao, X.W. Ma, H. Suzuki, P. Shuai, Y. Sun, S.W. Tang, J.S. Wang, S.T. Wang, G.Q. Xiao, X. Xu, J.W. Xia, J.C. Yang, R.P. Ye, T. Yamaguchi, X.L. Yan, Y.J. Yuan, Y. Yamaguchi, Y.D. Zang, H.W. Zhao, T.C. Zhao, X.Y. Zhang, X.H. Zhou, and W.L. Zhan. Precision isochronous mass measurements at the storage ring csre in lanzhou. *Nuclear Instruments and Methods in Physics Research Section A: Accelerators, Spectrometers, Detectors and Associated Equipment*, 654(1):213 – 218, 2011.
- [115] Y. H. Zhang, H. S. Xu, Yu. A. Litvinov, X. L. Tu, X. L. Yan, S. Typel, K. Blaum, M. Wang, X. H. Zhou, Y. Sun, B. A. Brown, Y. J. Yuan, J. W. Xia, J. C. Yang, G. Audi, X. C. Chen, G. B. Jia, Z. G. Hu, X. W. Ma, R. S. Mao, B. Mei, P. Shuai, Z. Y. Sun, S. T. Wang, G. Q. Xiao, X. Xu, T. Yamaguchi, Y. Yamaguchi, Y. D. Zang, H. W. Zhao, T. C. Zhao, W. Zhang, and W. L. Zhan. Mass measurements of the neutron-deficient ^{41}Ti , ^{45}Cr , ^{49}Fe , and ^{53}Ni nuclides: First test of the isobaric multiplet mass equation in *fp*-shell nuclei. *Phys. Rev. Lett.*, 109:102501, Sep 2012.
- [116] X. L. Yan, H. S. Xu, Yu. A. Litvinov, Y. H. Zhang, H. Schatz, X. L. Tu, K. Blaum, X. H. Zhou, B. H. Sun, J. J. He, Y. Sun, M. Wang, Y. J. Yuan, J. W. Xia, J. C. Yang, G. Audi, G. B. Jia, Z. G. Hu, X. W. Ma, R. S. Mao, B. Mei, P. Shuai, Z. Y. Sun, S. T. Wang, G. Q. Xiao, X. XU, T. Yamaguchi, Y. Yamaguchi, Y. D. Zang, H. W. Zhao, T. C. Zhao, W. Zhang, and W. L. Zhan. Mass measurement of ^{45}Cr and its impact on the ca-sc cycle in x-ray bursts. *The Astrophysical Journal Letters*, 766(1):L8, 2013.
- [117] P. Shuai, H.S. Xu, X.L. Tu, Y.H. Zhang, B.H. Sun, M. Wang, Yu.A. Litvinov, K. Blaum, X.H. Zhou, J.J. He, Y. Sun, K. Kaneko, Y.J. Yuan, J.W. Xia, J.C. Yang, G. Audi, X.L. Yan, X.C. Chen, G.B. Jia, Z.G. Hu, X.W. Ma, R.S. Mao, B. Mei, Z.Y. Sun, S.T. Wang, G.Q. Xiao, X. Xu, T. Yamaguchi, Y. Yamaguchi, Y.D. Zang, H.W. Zhao, T.C. Zhao, W. Zhang, and W.L. Zhan. Charge and frequency resolved isochronous mass spectrometry and the mass of ^{51}Co . *Physics Letters B*, 735(Supplement C):327 – 331, 2014.

- [118] Xu Xing, Wang Meng, Zhang Yu-Hu, Xu Hu-Shan, Shuai Peng, Tu Xiao-Lin, Yuri A. Litvinov, Zhou Xiao-Hong, Sun Bao-Hua, Yuan You-Jin, Xia Jia-Wen, Yang Jian-Cheng, Klaus Blaum, Chen Rui-Jiu, Chen Xiang-Cheng, Fu Chao-Yi, Ge Zhuang, Hu Zheng-Guo, Huang Wen-Jia, Liu Da-Wei, Lam Yi-Hua, Ma Xin-Wen, Mao Rui-Shi, T. Uesaka, Xiao Guo-Qing, Xing Yuan-Ming, T. Yamaguchi, Y. Yamaguchi, Zeng Qi, Yan Xin-Liang, Zhao Hong-Wei, Zhao Tie-Cheng, Zhang Wei, and Zhan Wen-Long. Direct mass measurements of neutron-rich 86 Kr projectile fragments and the persistence of neutron magic number $n = 32$ in sc isotopes. *Chinese Physics C*, 39(10):104001, 2015.
- [119] G. Audi, F.G. Kondev, Meng Wang, W.J. Huang, and S. Naimi. The *nubase2016* evaluation of nuclear properties. *Chinese Physics C*, 41(3):030001, 2017.
- [120] M. Wada et al. in progress.
- [121] P. Schury, M. Wada, Y. Ito, D. Kaji, H. Haba, Y. Hirayama, S. Kimura, H. Koura, M. MacCormick, H. Miyatake, J.Y. Moon, K. Morimoto, K. Morita, I. Murray, A. Ozawa, M. Rosenbusch, M. Reponen, A. Takamine, T. Tanaka, Y.X. Watanabe, and H. Wollnik. Observation of doubly-charged ions of francium isotopes extracted from a gas cell. *Nuclear Instruments and Methods in Physics Research Section B: Beam Interactions with Materials and Atoms*, 407:160 – 165, 2017.
- [122] Y. Ito, P. Schury, M. Wada, F. Arai, H. Haba, Y. Hirayama, S. Ishizawa, D. Kaji, S. Kimura, H. Koura, M. MacComick, H. Miyatake, J.Y. Moon, K. Morimoto, K. Morita, M. Mukai, I. Murray, T. Niwase, K. Okada, A. Ozawa, M. Rosenbusch, A. Takamine, T. Tanaka, Y.X. Watanabe, H. Wollnik, and S. Yamaki, 2017. arXiv:1709.06468.
- [123] M. La Commara, J. Gmez del Campo, A. D’Onofrio, A. Gadea, M. Glogowski, P. Jarillo-Herrero, N. Belcari, R. Borcea, G. de Angelis, C. Fahlander, M. Grska, H. Grawe, M. Hellstrm, R. Kirchner, M. Rejmund, V. Roca, E. Roeckl, M. Romano, K. Rykaczewski, K. Schmidt, and F. Terrasi. Production of very neutron-deficient isotopes near 100sn via reactions involving light-particle and cluster emission. *Nuclear Physics A*, 669(1):43 – 50, 2000.
- [124] A. Lépine-Szily, M. Chartier, G. Auger, W. Mittig, J. M. Casandjian, M. Chabert, L. K. Fifield, J. Fermé, A. Gillibert, M. Lewitowicz, M. MacCormick, M. H. Moscatello, O. H. Odland, N. A. Orr, G. Politi, C. Spitaels, and A. C. C. Villari. Mass measurements far from stability around the $n=z$ line ($100\text{sn}, 100\text{in}, 100\text{cd}$). *Acta Physica Hungarica New Series Heavy Ion Physics*, 6(1):157–168, Oct 1997.
- [125] M. Karny, L. Batist, A. Banu, F. Becker, A. Blazhev, B. A. Brown, W. Brüche, J. Döring, T. Faestermann, M. Górska, H. Grawe, Z. Janas, A. Jungclaus, M. Kavatsyuk, O. Kavatsyuk, R. Kirchner, M. La Commara, S. Mandal, C. Mazzocchi, K. Miernik, I. Mukha, S. Muralithar, C. Plettner, A. Płochocki, E. Roeckl, M. Romoli, K. Rykaczewski, M. Schädel, K. Schmidt, R. Schwengner, and J. Żylicz. Beta decay of the proton-rich nuclei 102sn and 104sn . *The European Physical Journal A - Hadrons and Nuclei*, 27(2):129–136, Feb 2006.
- [126] O. Kavatsyuk, C. Mazzocchi, Z. Janas, A. Banu, L. Batist, F. Becker, A. Blazhev, W. Brüche, J. Döring, T. Faestermann, M. Górska, H. Grawe, A. Jungclaus,

- M. Karny, M. Kavatsyuk, O. Klepper, R. Kirchner, M. La Commara, K. Miernik, I. Mukha, C. Plettner, A. Płochocki, E. Roeckl, M. Romoli, K. Rykaczewski, M. Schädel, K. Schmidt, R. Schwengner, and J. Żylicz. Beta decay of ^{101}Sn . *The European Physical Journal A*, 31(3):319–325, Mar 2007.
- [127] D. Alber, H. H. Bertschat, H. Grawe, H. Haas, B. Spellmeyer, and X. Sun. First in-beam observation of ^{97}Ag — the three-proton-hole spectrum in ^{100}Sn . *Zeitschrift für Physik A Atomic Nuclei*, 335(3):265–270, Sep 1990.
- [128] D. Alber, A. Berger, H. H. Bertschat, H. Grawe, H. Haas, H. Kluge, A. Kuhnert, H. E. Mahnke, K. H. Maier, R. Schubart, B. Spellmeyer, X. Sun, and L. Wood. Nuclear structure study of the neutron deficient cadmium isotopes 100 , 101 , ^{102}Cd . *Zeitschrift für Physik A Hadrons and Nuclei*, 344(1):1–11, Mar 1992.
- [129] R. Schneider, J. Friese, J. Reinhold, K. Zeitelhack, T. Faestermann, R. Gernhäuser, H. Gilg, F. Heine, J. Homolka, P. Kienle, H. J. Körner, H. Geissel, G. Münzenberg, and K. Sümmerer. Production and identification of ^{100}Sn . *Zeitschrift für Physik A Hadrons and Nuclei*, 348(4):241–242, Dec 1994.
- [130] M. Lewitowicz, R. Anne, G. Auger, D. Bazin, C. Borcea, V. Borrel, J.M. Corre, T. Dörfler, A. Fomichov, R. Grzywacz, D. Guillemaud-Mueller, R. Hue, M. Huyse, Z. Janas, H. Keller, S. Lukyanov, A.C. Mueller, Yu. Penionzhkevich, M. Pfützner, F. Pougheon, K. Rykaczewski, M.G. Saint-Laurent, K. Schmidt, W.D. Schmidt-Ott, O. Sorlin, J. Szerypo, O. Tarasov, J. Wauters, and J. Żylicz. Identification of the doubly-magic nucleus ^{100}Sn in the reaction $^{112}\text{Sn} + \text{nat Ni}$ at 63 mev/nucleon. *Physics Letters B*, 332(1):20 – 24, 1994.
- [131] D. Bazin, F. Montes, A. Becerril, G. Lorusso, A. Amthor, T. Baumann, H. Crawford, A. Estrade, A. Gade, T. Ginter, C. J. Guess, M. Hausmann, G. W. Hitt, P. Mantica, M. Matos, R. Meharchand, K. Minamisono, G. Perdikakis, J. Pereira, J. Pinter, M. Portillo, H. Schatz, K. Smith, J. Stoker, A. Stolz, and R. G. T. Zegers. Production and β decay of rp -process nuclei ^{96}Cd , ^{98}In , and ^{100}Sn . *Phys. Rev. Lett.*, 101:252501, Dec 2008.
- [132] C. B. Hinke, M. Böhmer, P. Boutachkov, T. Faestermann, H. Geissel, J. Gerl, M. Gernhäuser, R. and Górska, A. Gottardo, H. Grawe, J. L. Grębosz, R. Krücken, N. Kurz, Z. Liu, L. Maier, F. Nowacki, S. Pietri, Zs. Podolyák, K. Sieja, K. Steiger, K. Straub, H. Weick, H.-J. Wollersheim, P. J. Woods, N. Al-Dahan, N. Alkhomashi, A. Ataç, A. Blazhev, N. F. Braun, I. T. Čeliković, I. Davinson, T. and Dillmann, C. Domingo-Pardo, P. C. Doornenbal, G. de France, G. F. Farrelly, F. Fariñon, N. Goel, T. C. Habermann, R. Hoischen, R. Janik, M. Karny, A. Kaşkaş, I. M. Kojouharov, Th. Kröll, Y. Litvinov, S. Myalski, F. Nebel, S. Nishimura, C. Nociforo, J. Nyberg, A. R. Parikh, A. Procházka, P. H. Regan, C. Rigollet, H. Schaffner, C. Scheidenberger, S. Schwertel, P.-A. Söderström, S. J. Steer, A. Stolz, and P. Strmeň. Superallowed gamow-teller decay of the doubly magic nucleus ^{100}Sn . *Nature*, 486:341, 2012.
- [133] Valeriy Zagrebaev, Alexander Karpov, and Walter Greiner. Future of superheavy element research: Which nuclei could be synthesized within the next few years? *Journal of Physics: Conference Series*, 420(1):012001, 2013.

- [134] J.V. Kratz, W. Loveland, and K.J. Moody. Syntheses of transuranium isotopes with atomic numbers $z \geq 103$ in multi-nucleon transfer reactions. *Nuclear Physics A*, 944:117 – 157, 2015. Special Issue on Superheavy Elements.
- [135] V. I. Zagrebaev and Walter Greiner. Production of heavy and superheavy neutron-rich nuclei in transfer reactions. *Phys. Rev. C*, 83:044618, Apr 2011.
- [136] Kai Zhao, Zhuxia Li, Yingxun Zhang, Ning Wang, Qingfeng Li, Caiwan Shen, Yongjia Wang, and Xizhen Wu. Production of unknown neutron-rich isotopes in $^{238}\text{U} + ^{238}\text{U}$ collisions at near-barrier energy. *Phys. Rev. C*, 94:024601, Aug 2016.